t

National Technical University of Athens
School of Mechanical Engineering
Laboratory of Thermal Turbomachines
Parallel CFD & Optimization Unit

Exploring-optimizing the impact of bumps on the endwalls of a transonic compressor rotor

Diploma Thesis

Konstantinos Bouzalas

Supervisor: Kyriakos C. Giannakoglou, Professor NTUA

Athens 2025

National Technical University of Athens
School of Mechanical Engineering
Laboratory of Thermal Turbomachines
Parallel CFD & Optimization Unit

Exploring-optimizing the impact of bumps on the endwalls of a transonic compressor rotor

Diploma Thesis

Konstantinos Bouzalas

Supervisor: Kyriakos C. Giannakoglou, Professor NTUA

Athens 2025

Abstract

This thesis investigates the effects of endwall contouring on the aerodynamic performance of NASA Rotor 37, the inlet rotor of a transonic axial compressor, with emphasis on improving isentropic efficiency. NASA Rotor 37 is a widely recognized benchmark in the field of turbomachinery, offering both extensive computational and experimental data, which makes it an ideal candidate for this study. The primary objective of this research is to explore how variations in the contour of the rotor's hub and shroud regions, particularly outside the blade passage, affect the overall flow dynamics and performance.

Endwall contouring has emerged as a key focus in optimizing turbomachinery through Computational Fluid Dynamics (CFD), with extensive studies aimed at gaining a deeper understanding of flow behavior within these systems. The endwall region, in particular, plays a critical role in the overall performance of turbomachinery, where the interaction of boundary layers and the formation of secondary flows significantly affects pressure losses and flow uniformity. These complexities in the endwall region motivate the need for targeted optimization strategies that can mitigate secondary flows and enhance overall efficiency.

In this study, axisymmetric arch-shaped endwall contouring is applied to the sections outside the blade passage. Initially, a parametric study is performed to identify the most beneficial region for optimization, while exploring the different results of the regions and their impact on rotor performance. Secondly, the flow behavior is analyzed in response to the applied changes, enabling the evaluation of how the optimized geometry affects performance parameters, such as pressure losses and the velocity field.

The flow solver, PUMA(Parallel Unstructured Multi-row & Adjoint solver), and the optimization framework, EASY (Evolutional Algorithms SYstem), both of which are developed by the Parallel CFD & Optimization Unit (PCOpt) at NTUA, are utilized in this study. PUMA, a GPU-enabled software tool designed for flow simulations, ensures efficient and accurate computational analysis. Meanwhile, EASY, a generic optimization platform based on evolutionary algorithms and assisted by artificial intelligence, facilitates optimization by exploring and evaluating a wide design space. For the shape parameterization, Bézier curves are employed to define the endwall profile in the meridional plane offering flexibility and control over the design while the interpolation of the produced displacement to the interior is handled using Radial Basis Function (RBF) interpolation, ensuring smooth transitions across the geometry.

Εθνικό Μετσόβιο Πολυτεχνείο
Σχολή Μηχανολόγων Μηχανικών
Εργαστήριο Θερμικών Στροβιλομηχανών
Μονάδα Παράλληλης Υπολογιστικής Ρευστοδυναμικής
& Βελτιστοποίησης

Διερεύνηση-βελτιστοποίηση της επίδρασης διαμορφώσεων στα κελύφη κινητής πτερύγωσης διηχητικού συμπιεστή

Διπλωματική Εργασία

Μπουζαλάς Κωνσταντίνος

Επιβλέπων: Κυριάκος Χ. Γιαννάκογλου, Καθηγητής ΕΜΠ

Αθήνα, 2025

Περίληψη

Η διπλωματική αυτή διερευνά την επίδραση της διαμόρφωσης των κελυφών του δρομέα στην αεροδυναμική απόδοση του NASA Rotor 37, με έμφαση στη βελτίωση της ισεντροπικής απόδοσης. Ο δρομέας (NASA Rotor 37), με γεωμετρία χαμηλού λόγου επιμήκους, σχεδιάστηκε μαζί με τη σταθερή πτέρυγωση (Stator 37), αποτελώντας μαζί την πρώτη βαθμίδα ενός οκταβάθμιου διηχητικού αξονικού συμπιεστή. Ο δρομέας είναι ευρέως γνωστός στον τομέα της υπολογιστικής ρευστοδυναμικής, καθώς συνοδεύεται από εκτενή πειραματικά και υπολογιστικά δεδομένα, τα πρώτα από τα οποία είναι και διαθέσιμα από την NASA.

Η διαμόρφωση των κελυφών πτερύγωσης έχει αναδειχθεί ως βασικό πεδίο έρευνας στη βελτιστοποίηση των στροβιλομηχανών μέσω της υπολογιστικής Ρευστοδυναμικής , με εκτενείς μελέτες να στοχεύουν σε μια βαθύτερη κατανόηση της συμπεριφοράς της ροής σε αυτά τα συστήματα. Η περιοχή των κελυφών διαδραματίζει καθοριστικό ρόλο στη συνολική απόδοση των στροβιλομηχανών, καθώς η αλληλεπίδραση των οριακών στρωμάτων και ο σχηματισμός δευτερευουσών ροών επηρεάζουν σημαντικά τις απώλειες πίεσης και την ομοιομορφία της ροής. Αυτές οι πολύπλοκες ροϊκές δομές στην περιοχή των κελυφών καθιστούν αναγκαία την ανάπτυξη στοχευμένων στρατηγικών βελτιστοποίησης,

ικανών να μετριάσουν τις δευτερεύουσες ροές και να ενισχύσουν τη συνολική απόδοση.

Στην παρούσα μελέτη, εφαρμόζεται αξονοσυμμετρική καμπυλοειδής διαμόρφωση στα κελύφη εκτός του περάσματος του δρομέα. Αρχικά, διεξάγεται μια παραμετρική μελέτη για τον εντοπισμό της περιοχής με τα πιο ευνοϊκά αποτελέσματα ως προς την απόδοση εκφραζόμενη από τον ισεντρόπικο βαθμό απόδοσης, προκειμένου η διαδικασία βελτιστοποίησης να επικεντρωθεί σε αυτήν, εξετάζοντας παράλληλα τα διαφορετικά αποτελέσματα των περιοχών και την επίδρασή τους στην απόδοση του δρομέα. Στη συνέχεια, αναλύεται η συμπεριφορά της ροής ως απόκριση στις εφαρμοζόμενες μεταβολές, επιτρέποντας την αξιολόγηση του τρόπου με τον οποίο η βελτιστοποιημένη γεωμετρία επηρεάζει παραμέτρους απόδοσης, όπως οι απώλειες πίεσης και το πεδίο ταχυτήτων.

Η επίλυση και προσομοίωση της ροής πραγματοποιείται με το λογισμικό PUMA (Parallel Unstructured Multi-row & Adjoint solver), ενώ η βελτιστοποίηση πραγματοποιείται μέσω της πλατφόρμας EASY (Evolutional Algorithms SYstem). Και τα δύο εργαλεία, ανεπτυγμένα από τη Μονάδα Παράλληλης Υπολογιστικής Ρευστοδυναμικής & Βελτιστοποίησης του ΕΜΠ, χρησιμοποιούνται σε αυτή τη μελέτη. Ο PUMA, ένα λογισμικό εργαλείο προσομοίωσης ροής που χρησιμοποιεί GPU για την εκτέλεση των υπολογισμών, διασφαλίζει αποδοτική και ακριβή υπολογιστική ανάλυση. Παράλληλα, ο EASY, μια γενική πλατφόρμα βελτιστοποίησης βασισμένη στους εξελικτικούς αλγορίθμους και υποστηριζόμενη από μεθόδους τεχνητής νοημοσύνης, επιτρέπει μια αξιόπιστη διαδικασία βελτιστοποίησης, εξερευνώντας και αξιολογώντας έναν ευρύ σχεδιαστικό χώρο. Για την παραμετροποίηση της γεωμετρίας, χρησιμοποιούνται καμπύλες Bèzier για τον ορισμό του προφίλ του κελύφους στον μεσημβρινό επίπεδο, παρέχοντας ευελιξία και έλεγχο στον σχεδιασμό, ενώ η παρεμβολή της προκύπτουσας μετατόπισης προς το εσωτερικό υλοποιείται μέσω παρεμβολής με Radial Basis Function (RBF), εξασφαλίζοντας ομαλές μεταβάσεις στη γεωμετρία.

List of Abbreviations

- **CFD** - Computational Fluid Dynamics
- **PCOpt** - Parallel CFD & Optimization Unit
- **RBF** - Radial Basis Function
- **NTUA** - National Technical University of Athens
- **EA** - Evolutionary Algorithm
- **PUMA** - Parallel, Unstructured, Multirow flow & Adjoint solver
- **EASY** - Evolutional Algorithms SYstem
- **MAEA** - Metamodel-Assisted Evolutionary Algorithm
- **RANS** - Reynolds-Averaged Navier-Stokes

Contents

List of Figures

List of Tables

Chapter 1

Introduction

1.1 Fundamentals of Axial-Flow Compressors

1.1.1 Historical Origins of Axial-Flow Compressors

The idea of using a form of reversed turbine as an axial compressor is as old as the reaction turbine itself. One of the earliest experimental axial-flow compressors (1884) was obtained by C. A. Parsons by running a multistage reaction type turbine in reverse [13]. However simply reversing the turbine's blade rotation resulted in very low efficiencies.The idea of altering blades geometry along the flow path to enhance performance first surfaced in the early 1900s. However, significant progress in axial compressor and gas turbine development didn't take off until World War II, driven by the need for advanced propulsion systems in aviation.Around that time, it was quickly realised that more compression resulted in more engine power without adding significant weight, making it a crucial factor in improving aircraft performance.

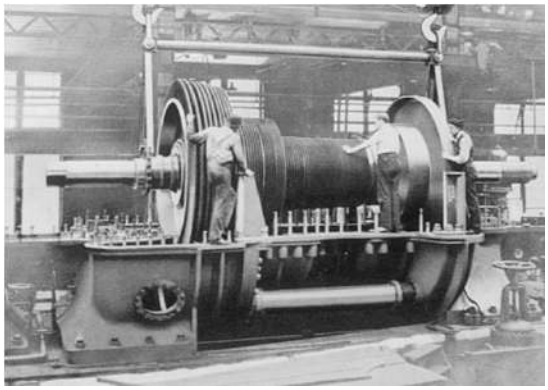

Figure 1.1: Parsons Axial flow Steam turbine Opened for inspection.(Parsons,1926)[17]

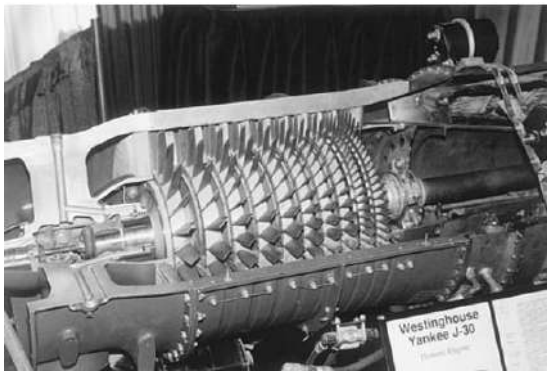

Figure 1.2: Westinghouse Yankee J-30, 10-stage Axial flow Compressor (Pressure ratio 3.8:1), Cutaway View.[17]

One of the main distinctions between compressors and turbines lies in the direction of the velocity gradient. In compressors, the flow is slowed down in order to increase its pressure, and consequently, according the Bernoulli's principle, adverse pressure gradients that can lead to problems like flow separation, stall, or at worst, surge, where the perturbation occurs in the axial direction ([4]). As a result, compressors require multiple stages to increase the flow's pressure, step by step, achieving the desired pressure rise. Turbines, on the other hand, typically a small number of stages, as the acceleration of the flow, creates a favorable pressure gradient that reduces the risk of such instabilities. However, turbines face challenges primarily related to high thermal loads due to the elevated temperatures in the flow.

1.1.2 Early Simplifications and Modern Advancements in Compressor Flow Analysis

The flow through axial-flow compressors is an extremely complicated three-dimensional phenomenon, characterized by strong gradients in the axial, radial, and circumferential directions. Figure 1.3 provides an overview of the complex flow phenomena occurring within the passage, such as flow separations, tip leakage vortices, secondary flows, and other effects that contribute to the overall aerodynamic behavior. In a NASA report from 1999[3], four critical flow phenomena were identified as key research challenges in turbomachinery: unsteady flow, transition to turbulence, film cooling, and three-dimensional flow (including tip leakage effects). These phenomena continue to play a significant role in the performance and optimization of compressors, influencing both current and future research.

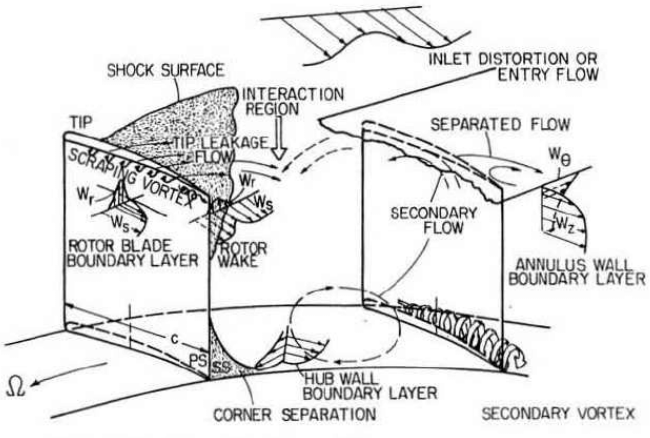

Figure 1.3: Nature of the Flow in an Axial Flow Compressor Rotor Passage [8]

Engineers in the 1950s began simplifying compressor analysis by employing 2D techniques, such as the blade-element method and axial symmetry. The blade-element

approach assumes that the flow in the circumferential plane can be analyzed by examining blade profiles formed by the intersection of a flow surface of revolution and the compressor blades Figure 1.4. The assumption of axial symmetry further simplifies this approach by allowing an average value to represent the air's state across the blade-to-blade plane, treating the flow as uniform in the circumferential section. Together, these assumptions form a quasi-3D approach, with radial variations handled through radial equilibrium, continuity, and energy equations in the meridional plane (from hub to tip).

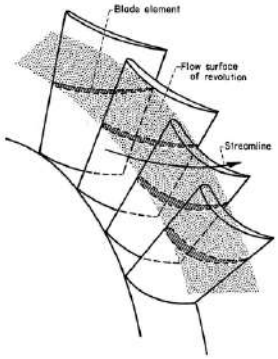

Figure 1.4: Flow in circumferential plane .[13]

Advancements in technology and computational power have transformed compressor design, allowing for detailed 3D flow simulations through CFD. By the early 1980s, full 3D problems began to be solved, highlighting the importance of CFD simulations and numerical optimization. Figure 1.5 illustrates how these advancements have increased the efficiency of SNECMA fan performance over more than 30 years. Despite advances in CFD, previously developed semi-empirical remain integral to modern compressor design.

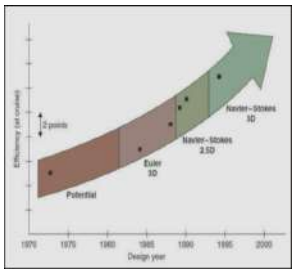

Figure 1.5: Impact of CFD on SNECMA fan performance, over a period of 30 years.[26]

1.1.3 Design of Multistage Axial-Flow Compressors

Axial flow compressors handle a large mass flow of air and increase its pressure and temperature through a series of stages. Each stage consists of a rotating blade (rotor) followed by a stationary blade (stator). The rotor's role is to impart kinetic energy to the fluid by increasing its tangential velocity through the rotation of the blades, while also converting some of this kinetic energy into static pressure due to the turning of the flow and the diffusive path between the blades, which decelerates the flow and increases the pressure. The stator's role is to further decelerate the flow by redirecting it to a more axial direction, preparing it for the next stage, if any.

In Figure 1.6, the meridional view of a compressor stage is shown, highlighting stations 1, 2, and 3 that represent the inlet, the region between the rotor and stator, and the outlet. This provides an overview of the flow path across the stage. In Figure 1.7, the corresponding velocity triangles are illustrated. These provide insight into how the flow turns as it passes through the rotor and stator, highlighting changes in both absolute and relative frame.

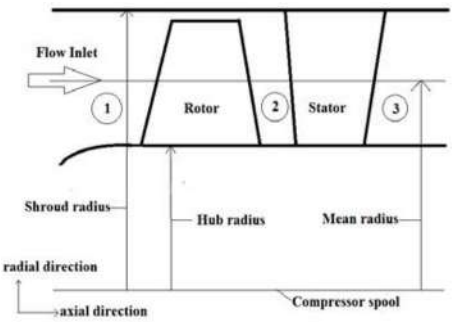

Figure 1.6: Schematic of meridional view of a compressor stage specifying stations 1, 2, and 3([20]).

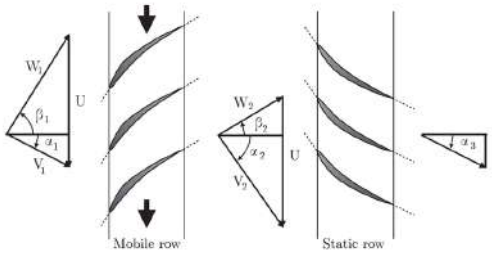

Figure 1.7: Example of velocity diagrams within a compressor stage([16]).

To achieve a higher pressure ratio, adjustments to the velocity triangles are essential. This can be achieved by increasing the flow turning, diffusing the flow path, raising the rotational speed, or by increasing the axial velocity-each with its own limitations. Increasing the flow turning and diffusing the flow path, and thereby decelerating the fluid, is restricted by the de Haller rule, established through experiments on linear cascades in 1953 to limit losses and prevent flow separation. Increasing the rotational speed of a compressor can indeed raise the pressure ratio, but it is constrained by mechanical limits due to the centrifugal forces acting on the blades. Increasing the axial velocity can lead to shock wave formation, especially near the blade tips where the relative velocity is highest. The formation of these shock waves, if carefully managed to minimize losses, may considerably increase static pressure. It is preferable to have

early compressor stages operate in the transonic regime to harness these advantages, while fully supersonic flow conditions remain an area of ongoing research.[19]

In designing a multistage compressor, the initial step is to determine the velocity diagrams at the design operating point to achieve the desired increase in total pressure. The blade-element method remains the foundation of this procedure, allowing for the specification of velocity diagrams at each radial position. This approach ensures that the blade profiles are developed based on these velocity diagrams to meet the required performance criteria. For the third step, the focus shifts to off-design performance, where stage matching becomes essential to ensure efficient operation across a range of conditions.

Stage matching problem

Every machine has to start, and the same applies to compressors. During startup or at lower power settings, it is essential for a multistage compressor to operate under stable conditions, maintaining smooth airflow through the stages. Especially in high-pressure compressors, it is a vital and highly sensitive task to match the stages in such a way that they operate in stable conditions under varying operational demands. At lower rotational speeds, the front stages are particularly vulnerable to approaching the surge line due to reduced mass flow while the rear stages face the problem of choking. A well-designed flow passage through the compressor aims to maintain a constant axial velocity. To achieve this, as the density of the flow increases, the cross-sectional area of the flow path is decreased accordingly. This is why the rear stages can face choking: the pressure isn't high enough to sufficiently increase the density, causing the mass flow to rise beyond the stage's capacity, leading to choked flow conditions.([2])

One approach to address the issue of front stages nearing the surge line is to use variable stator vanes. By adjusting the stator angle, the compressor can maintain optimal flow angles under reduced mass flow conditions, helping to keep the stages within stable operating limits. This method allows these stages to operate closer to stall conditions during off-design points but comes at the cost of added mechanical complexity and control requirements. Variable stator vanes are particularly beneficial in managing surge risk across a wide range of operating speeds, especially where flexibility in response to fluctuating conditions is critical. To prevent choking at the rear stages, a common approach is to bleed air from intermediate stages.

CFD Role in the process - Performance Map

After the preliminary design phase, CFD plays a crucial role in optimizing compressor performance. It provides insights into the behavior of the compressor under various

operating conditions, contributing to the development of a detailed performance map that illustrates efficiency and flow characteristics across different scenarios.

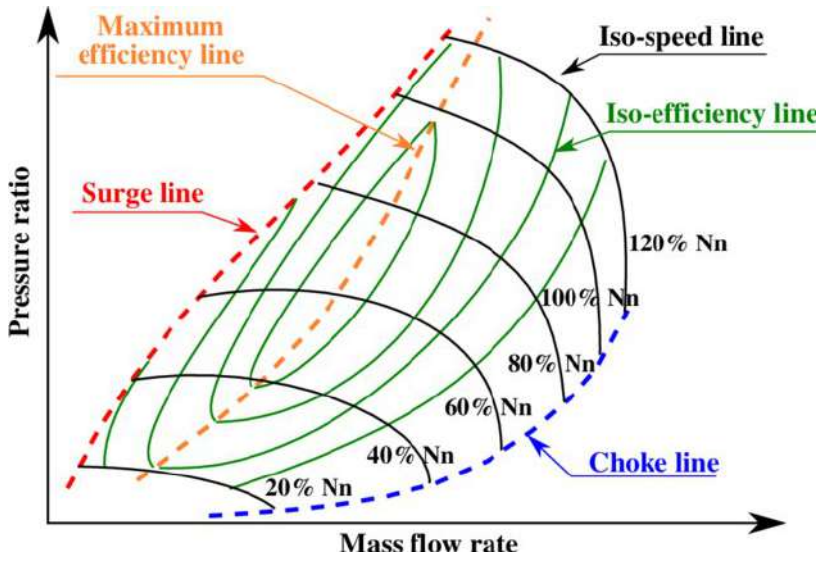

Figure 1.8: Typical compressor performance map ([34].

Figure 1.8 shows an example of a compressor map, illustrating the performance characteristics of a multistage compressor under varying operating conditions. The map presents key parameters, such as mass flow rate and pressure ratio, offering insight into the compressor's behavior across different speeds and operating regimes. The map also displays the contours of iso-isentropic efficiency, providing insight into efficiency variations across different operating conditions. The maximum efficiency line illustrates the typical path of operation.

In turbomachinery, CFD serves as an indispensable tool for refining designs and ensuring optimal performance across a wide range of operating conditions. Although capturing the full complexity of the flow inside turbomachinery remains a challenge due to phenomena like turbulence and unsteady flow interactions, CFD excels in identifying meaningful trends and differences. These insights often translate directly into practical improvements in real-world applications. Beyond performance mapping, CFD enables detailed analysis of flow phenomena, such as boundary layer behavior, flow separation, and secondary flows. Such analyses guide the implementation of advanced optimization techniques, including endwall contouring, which aims to reduce losses and improve efficiency by mitigating secondary flow structures and enhancing flow uniformity. By simulating various design modifications and analyzing their impact on performance metrics like total pressure loss and efficiency, CFD accelerates the iterative design process and fosters innovations in compressor design.

1.2 About Endwall Contouring

Endwall contouring has emerged as a critical optimization technique in turbomachinery design, addressing the persistent challenge of secondary flow losses that occur in the blade-endwall regions. These losses, driven by the interaction of boundary layers and secondary flow structures, can significantly reduce the overall efficiency of compressors and turbines. By reshaping the endwall surfaces to guide the flow more effectively, endwall contouring aims to mitigate these losses, leading to improvements in efficiency and operational stability.

Secondary flows ([10]) account for a substantial total pressure loss in the overall losses inside a rotor passage. Their existence is inherently a 3D phenomenon, and they form as the flow enters the blade passage with a non-uniform radial distribution of velocity and turns due to the blade. The non-uniformity of the velocity at the blade inlet is primarily caused by the influence of the viscous region of the endwall boundary layers. However, the free-stream region can also enter with velocity variations, for example, due to a wake formed by an upstream blade ([25]). Figure 1.9, shows how streamlines follow a certain curvature along the normal flow path and how the interplay between low-momentum fluid from the endwall boundary layers and the pressure gradient in the peripheral direction alters this path, resulting in a reduced curvature.

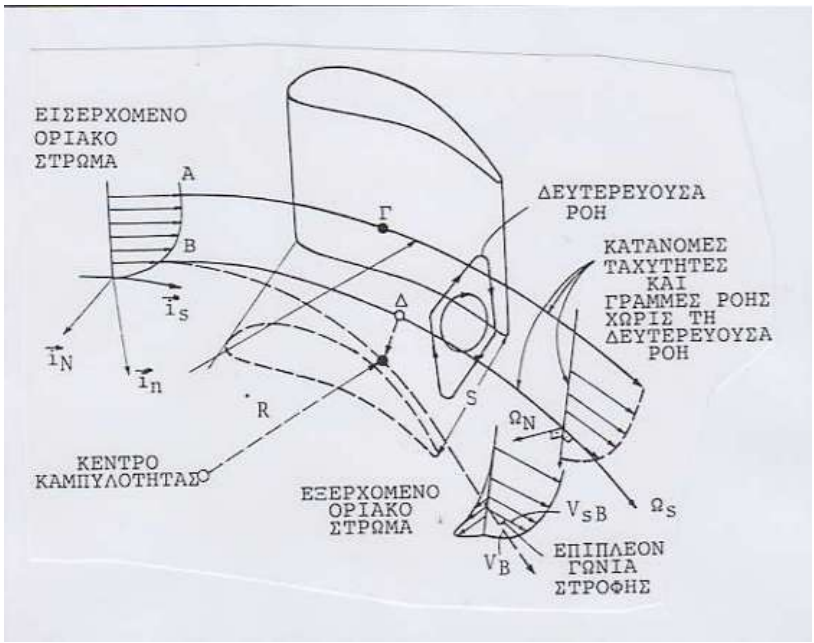

Figure 1.9: Formation of secondary flows inside blade passage ([10]).

Additionally, by solving the continuity equation, we see that velocity components appear in both directions perpendicular to the main flow direction. In other words, any

non-uniformity in the radial velocity distribution at the blade inlet can be considered a primary vortex, which then leads to the formation of secondary vortices that account for what we call secondary flows.

Several complex flow phenomena are at play in the blade-endwall region, each contributing to the overall loss mechanisms. Boundary layer interactions between the blade surface and the endwall create regions of high shear and separation, promoting the formation of secondary flows such as passage vortices and corner vortices. These vortices increase aerodynamic losses and disrupt flow uniformity downstream. Additionally, in transonic flows, shock wave interactions with the boundary layer can further complicate the flow field, causing local separation and intensifying mixing. This mixing, which is often localized in regions of flow turning or high-pressure gradients, exacerbates secondary flow effects and amplifies total pressure losses.

The cumulative effect of these phenomena–boundary layer interactions, secondary flows, shock-boundary layer interactions, and mixing–is most pronounced in areas where flow paths converge or diverge, such as near the blade leading and trailing edges. Endwall contouring seeks to address these challenges holistically by carefully tailoring the geometry to reduce local gradients and guide the flow more effectively. Through shape optimization methods, designers can make changes to the hub or shroud geometry that balance all contributing factors to minimize losses and improve performance.

There are numerous papers ([11] , [18] , [15])applying endwall contouring to optimize turbomachinery performance, demonstrating its ability to alter flow structures and reduce losses. Endwall contouring induces changes in the vortices within the flow, such as passage and corner vortices. Common approaches include axisymmetric and non-axisymmetric contouring (Figure 1.10). Axisymmetric designs maintain a uniform geometry along the circumferential direction, typically focusing on reducing total pressure loss by smoothing the flow. In contrast, non-axisymmetric contouring introduces localized variations in geometry.

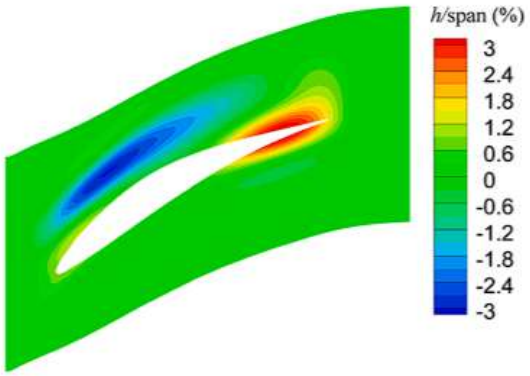

Fig. 2. Adopted non-axisymmetric end-wall.

Figure 1.10: Illustration of non-axisymmetric endwall contouring. Adapted from [21].

Several studies have explored various applications of endwall contouring, each highlighting unique aspects of its impact on turbomachinery performance. A study ([24]) optimizing the hub endwall passage by introducing a hill-and-valley geometry successfully reduced total losses by up to 16%. This improvement was achieved by minimizing corner stall, thereby reducing the associated secondary flow losses in the region. Additionally, enhanced the uniformity of the flow, for beneficial effects on a hypothetical next stage or the combustion chamber. Another study ([33]), focused on axisymmetric arc-shaped casing contouring in a 2-stage turbine, which increased efficiency. The arc-shaped casing led to smoother loading distribution in the tip region, reducing peak values and enlarging the low-velocity zone. As a result of this sequence, the axisymmetric casing contouring prevents more flow on the tip pressure side from leaking to the suction side and, thus, losses are reduced.

1.3 Case Study: NASA Rotor 37

This study focuses on the NASA Rotor 37 as the test case. The NASA Rotor 37 test case is well known in the field of CFD for turbomachinery applications, having been extensively utilized for code validation purposes and cross-referencing with experimental data.

Originally designed and tested by Reid and Moore in 1978 [23] as a part of four highly loaded, high-speed inlet stages for an advanced high-pressure-ratio core compressor. The primary design differences among these stages were total pressure ratio $(1.82, 2.05)$ and blade row aspect ratio. Notably, the low aspect ratio stages demonstrated significantly better performance, with the high-pressure-ratio stage being more efficient across varying speeds.

Rotor 37, part of Stage 37, represents the low aspect ratio configuration with the

high-pressure ratio, with the following geometric properties:

- Rotor inlet hub-to-tip diameter ratio 0.7.
- Rotor blade aspect ratio 1.19.
- Rotor tip relative inlet Mach number 1.48.
- Rotor hub relative inlet Mach number 1.13.
- Rotor tip solidity 1.29.
- Blade airfoil sections Multiple-Circular-Arc (MCA).

The design operating values for the rotor and other data, are presented in Table 1.1,

PARAMETER	DESIGN VALUE
Rotor total pressure ratio	2.106
Rotor total temperature ratio	1.270
Rotor isentropic efficiency	0.877
Mass flow	20.188 $(\frac{kg}{s})$
Rotational speed	17188.7 (RPM)
Number of rotor blades	36

Table 1.1: Rotor 37 - Design parameters

Experimental investigations of the flow field of Rotor 37 were conducted by Kenneth L. Suder in 1996([29],[30]). The first experiment aimed to investigate the effects of tip clearance on the flow by comparing the relative Mach numbers along streamlines at 90% and 95% spanwise positions. The second experiment focused on examining the flow mechanisms responsible for the development of blockage at various operating conditions and locations along the blade, particularly about shock formation.

Rotor 37 was tested in isolation to eliminate interaction effects from an upstream inlet guide vane or downstream stator blade row. The tests were conducted with atmospheric inlet and exit conditions, using a downstream throttle valve to control back pressure on the rotor.

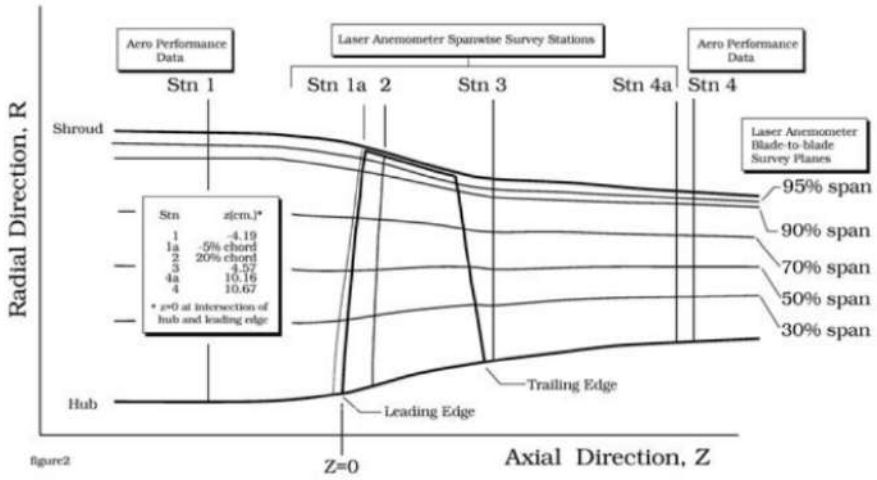

Figure 1.11: Meridional plane of the rotor, highlighting the various stations where measurements are taken.

Stations 1 and 4 were positioned at a distance from the main flow to minimize interactions, allowing for measurements of total pressure, total temperature, and flow angle at 18 distinct radial positions using Cobra probes. These available measurements serve as a reference for comparison and analysis of the results obtained in this study.

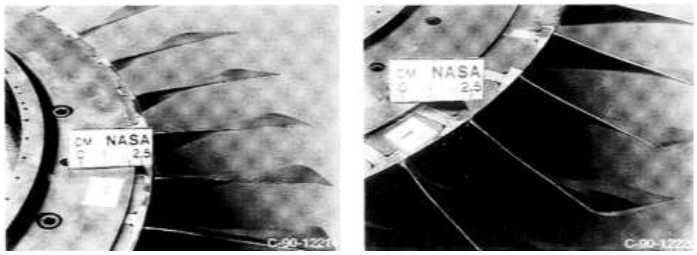

Figure 1.12: Photographs of NASA Rotor 37. Left: In-channel view looking downstream. Right: In-channel view looking upstream([29]).

Chapter 2

Analysis of Rotor 37 using PUMA

For the computational process, this diploma thesis utilized PUMA, a GPU-enabled flow solver developed by the PCOpt/NTUA. Originally a CPU-based solver, PUMA has been adapted to GPUs, with programming and development performed in CUDA C/C++.

The GPU architecture, with its shared memory and parallel thread execution, introduces challenges in terms of discretization and numerical algorithms. Specific attention is needed for handling memory latency and avoiding thread race conditions, particularly in scatter-add algorithms used for numerical flux computations. These techniques, applied during the runs, derived from the PhD work of X. Trompoukis ([31]), have significantly enhanced the solver's performance, achieving speed-ups up to 45 times faster than the CPU version, depending on the hardware used.

PUMA also facilitates detailed flow analysis for turbomachinery applications by enabling the extraction of flow results across predefined radial zones at specific z-locations chosen for printing. These zones, 21 in total, are distributed along the radial direction using a hyperbolic tangent function, which concentrates more zones near the edges for higher resolution in critical regions. Within these zones, PUMA computes area- or mass-flow-averaged quantities, allowing the radial distribution of selected flow variables to be evaluated on each slice. This approach provides precise insights into the flow behavior, especially near the boundaries, where data accurancy is crucial for performance analysis.

2.1 Flow Model

2.1.1 Governing Equations

The 3D Reynolds-Averaged Navier-Stokes (RANS) equations for compressible, turbulent flow are solved. The hyperbolic nature of these equations makes them suitable for a time-marching technique, by including pseudo-time derivatives in the equations. In its iteration through pseudo-time, the solver updates the field properties until convergence is achieved.

To solve the system of RANS equations, an additional equation computes the turbulent viscosity (μ_t). For this, the Spalart-Allmaras turbulence model [28] is employed.

A vertex-centered Finite Volume Method (FVM) is used for spatial discretization, making it appropriate for unstructured meshes.

All the details regarding the system of equations solved by PUMA, along with their discretization, are thoroughly explained by Konstantinos T. Tsiakas in his PhD thesis ([32]). For a more comprehensive understanding of the equations and their discretization, the reader is referred to his work.

2.1.2 Boundary conditions

Inlet boundary conditions

Along the inlet boundaries, five quantities must be specified, while one is extrapolated from the flow domain. In this case, the radial distribution of total temperature, total pressure, and two flow angles that define the inlet velocity direction are specified. The Mach number is the extrapolated variable from the interior of the flow domain. Concerning the turbulence model, the fifth inlet boundary condition specified is the viscosity ratio $(\frac{\nu_t}{\nu})_{in}$.

Outlet boundary conditions

In this case, where the outlet condition of the flow is subsonic, one quantity must be specified. Here, the mean static pressure at a radius of $0.216m$ is specified and since the value of an integral quantity over the entire outlet boundary is specified, the pressure at the outlet is iteratively computed by uniformly correcting the ones extrapolated from the flow domain. This is accomplished by solving a simplified radial equilibrium equation accounting for pressure gradient and centrifugal forces.

$$\frac{\partial p}{\partial r} = -\rho \frac{(V_u)^2}{r}$$

(where V_u is the absolute peripheral velocity).

For the turbulence model, a zero Neumann boundary condition is applied. The remaining four quantities are extrapolated from the flow domain(Total temperature, Mach number, and flow angles.)

As specified, the outlet boundary condition is defined by static pressure. Therefore, the operating point, while often described in terms of mass flow ($\dot{m}$) or total pressure, is not straightforward to define without explicitly specifying the static pressure.

Periodic boundary conditions

Peripheral periodicity is enforced on the sides of the flow domain, where two points are periodically linked if their projections onto the meridional plane coincide and their circumferential positions differ by the peripheral pitch. Paired points exhibit identical scalar values, while vector and tensor quantities, such as velocity or spatial derivatives, undergo rotation by the row pitch between these paired points.

Wall boundary conditions

At all solid walls, the no-slip condition is enforced as:

$$\vec{W}_{wall} = 0$$

where the superscript R denotes the velocity in the relative frame. This ensures that the velocity relative to the wall is zero. For thermal boundary conditions, an adiabatic wall condition is specified:

$$\frac{\partial T}{\partial n} = 0$$

This condition means there is no heat flux across the wall, which is common for adiabatic surfaces.

Additionally, to accurately model the near-wall flow, a **low-Reynolds approach** is applied, where the grid is fine enough to resolve the flow in the boundary layer. This is achieved by ensuring that the dimensionless wall distance y^+ is kept below 1:

$$y^+ = \frac{\rho u_\tau y}{\mu} < 1$$

Here, ρ represents the fluid density, u_τ is the friction velocity (calculated as $u_\tau = \sqrt{\tau_w/\rho}$, where τ_w is the wall shear stress), y is the physical distance from the wall, and μ is the dynamic viscosity. A y^+ value of less than 1 ensures that the first grid point is very close to the wall, allowing for accurate resolution of the near-wall flow

and capturing critical details of the boundary layer dynamics. In our cases, the y^+ values typically range from 0.0016 to 1.42.

To ensure consistency with the original experimental setup, the inlet boundary conditions used in this study are based on the Station 1 experimental data from the NASA test campaign, which is publicly available online. These conditions define the flow characteristics upstream of the rotor and serve as a reference for numerical simulations. The inlet experimental data are presented in Table 2.1 .

Radius(m)	Total Pressure ($\frac{N}{m^2}$)	Total Temperature (K)	Viscosity Ratio
0.179222	99947.0	288.265	5.83
0.18349	101740.0	287.862	5.83
0.187452	101872.0	287.775	5.83
0.191414	101872.0	287.804	5.83
0.195682	101872.0	287.804	5.83
0.199644	101872.0	287.804	5.83
0.205435	101872.0	287.862	5.83
0.210922	101872.0	287.977	5.83
0.216713	101811.0	288.035	5.83
0.222504	101740.0	288.265	5.83
0.22799	101670.0	288.381	5.83
0.232258	101740.0	288.323	5.83
0.23622	101811.0	288.208	5.83
0.240182	101740.0	288.15	5.83
0.24445	101528.0	288.208	5.83
0.248412	100910.0	288.265	5.83
0.251765	98913.5	288.265	5.83
0.254203	95600.1	288.381	5.83

Table 2.1: Inlet boundary conditions [6].

2.2 PUMA Results Against Measurements

In this section, CFD results by the PUMA flow solver are compared with experimental measurements.

The primary parameters for comparison include the total pressure ratio (PR), total temperature ratio (TR), isentropic efficiency (η_{is}) across a range of mass flow conditions, ranging from stall to choke, as well as the total pressure radial distribution at the exit (Station 4). The results are shown in Figure 2.1,Figure 2.2 and Figure 2.3.

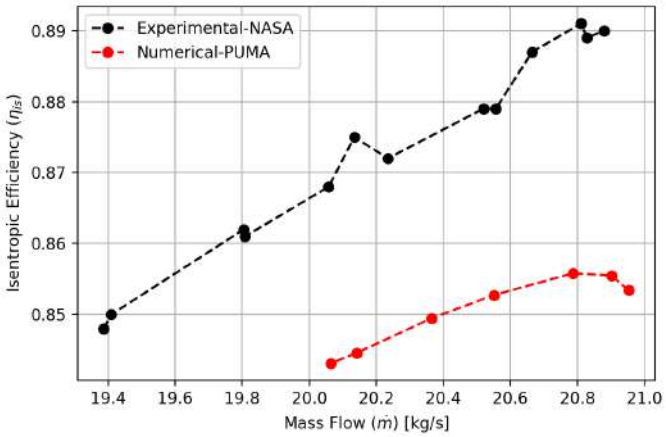

Figure 2.1: Comparison - Isentropic Efficiency (η_{is}).

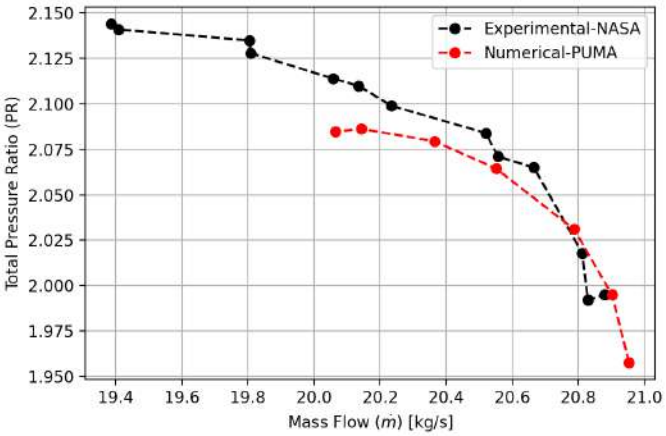

Figure 2.2: Comparison - Total Pressure Ratio PR.

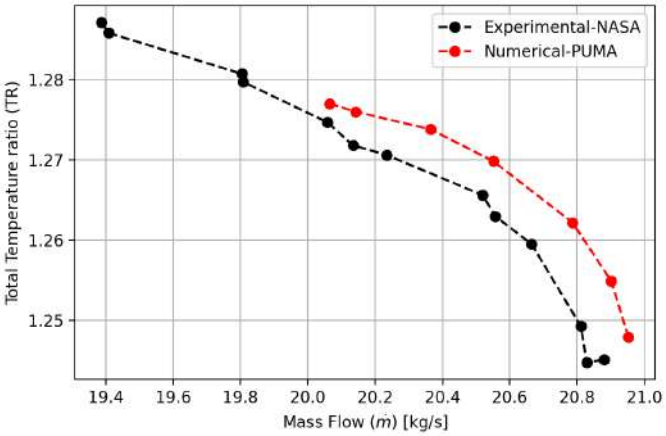

Figure 2.3: Comparison - Total Temperature Ratio TR.

In the following sections of this diploma, when referring to "near peak efficiency", it corresponds to the operating point with a mass flow of $20.5\frac{kg}{s}$, an isentropic efficiency of 0.85273 and a total pressure ratio of 2.06445.

The total pressure prediction reasonably matches the experimental data, demonstrating good agreement in capturing the aerodynamic performance of the rotor. However, the total temperature is overpredicted in the simulation, resulting in an underprediction of the isentropic efficiency and an overestimation of energy losses within the rotor.

Figure 2.4 and Figure 2.5 show the prediction of the radial distribution of total pressure ratio and isentropic efficiency at the exit, near peak efficiency, follows a similar trend. The total pressure ratio is generally well predicted; however, in the hub region, there are indications of hub leakage([27]), leading to an overprediction of total pressure, as the simulation fails to capture its detailed effects. Isentropic efficiency shows a deficit of around 3% in the middle spanwise region, with the deficit increasing near the tip-wall region.

The prediction of the radial distribution of total pressure ratio and isentropic efficiency at the exit, near peak efficiency, follows a similar trend. The total pressure ratio is generally well predicted; however, in the hub region, there are indications of hub leakage, which refers to the inability of many codes to accurately predict the flow deficit at the hub([12]). As a result, they often consider a small hub leakage, leading to an overprediction of total pressure, as the simulation fails to capture the detailed effects of the leakage. Isentropic efficiency shows a deficit of around 3% in the middle spanwise region, with the deficit increasing near the tip-wall region.

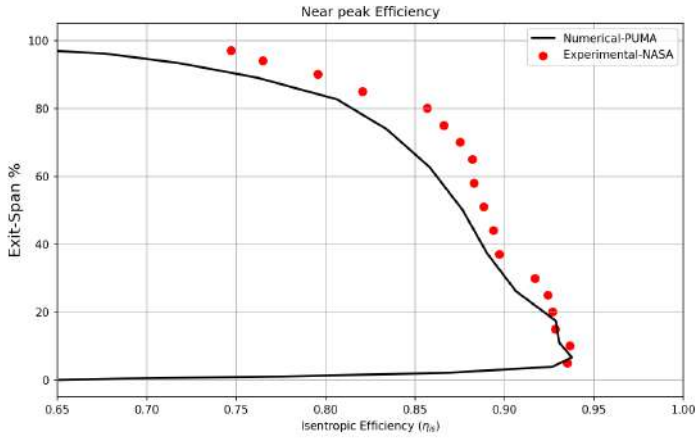

Figure 2.4: Radial distribution of Isentropic Efficiency calculated separately at each spanwise location using inlet and outlet, mass-averaged, total pressure and total temperature values. Comparison with experimental data.

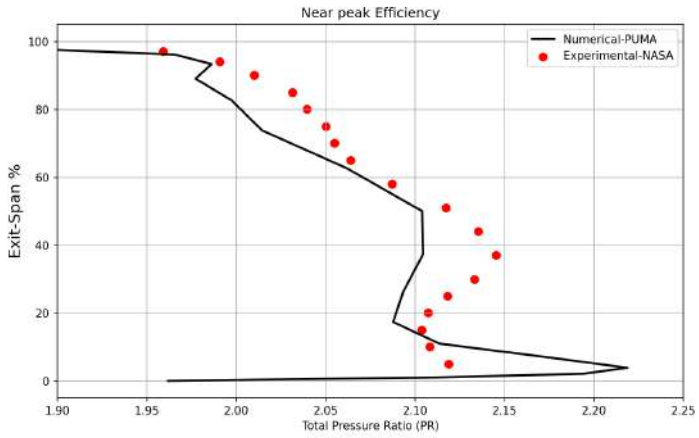

Figure 2.5: Comparison of the radial distribution of Total Pressure Ratio with experimental data.

Overall, PUMA predicts total pressure reasonably well, particularly in the region from near peak efficiency to choke. In addition, the radial distribution of total pressure at the exit reveals a deficit in the hub region, which is consistent with the experimental data showing hub leakage flow ([27]). Many simulations using turbulence transport models show an underprediction of isentropic efficiency by approximately 3%, ranging from 10% to 80% of the blade span at exit([6]). Figure 2.6 presents a comparison of various CFD codes, highlighting this common tendency to underestimate isentropic efficiency.

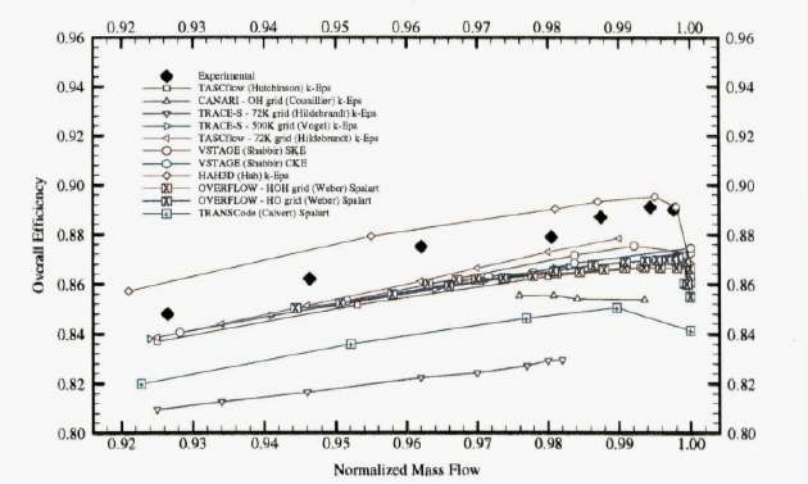

Figure 2.6: Comparison of Isentropic Efficiency from different simulation codes Using Turbulence Transport Models ([6]).

This section examines the effects of tip clearance vortices within the rotor by ana-

lyzing the relative Mach number spanwise distribution. The results from PUMA are compared against experimental data of [29], with a focus on the 90% and 95% spanwise locations(Figure 2.7). The experimental data were digitized to extract values directly from the figures.

The analysis highlights how tip clearance vortices cause a significant drop in relative Mach number near the blade tip, which is evident in the experimental data. These vortices are generated due to the pressure difference across the blade tip, resulting in leakage flow that impacts the overall aerodynamic performance. For consistency with [30], the chord length referenced in this analysis is normalized using the hub's chord length.

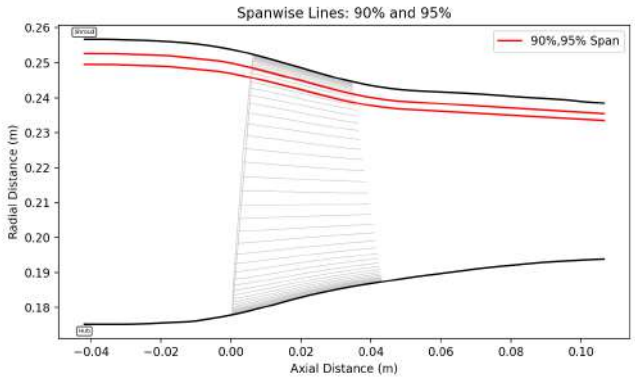

Figure 2.7: Radial zones along the meridional plane of Rotor 37.

To gain a first understanding of the tip clearance vortices, visualization is performed using slices at constant z-axis values, highlighting the magnitude of the vorticity field. Figure 2.8 and Figure 2.9 illustrate the magnitude of vortices generated from the tip clearance at 20% and 60% chord length positions, respectively, as viewed from upstream to downstream. In particular, the vorticity generated due to the tip leakage flow moving from the pressure side to the suction side and then, penetrating into the flow field can be identified. At 20% chord length, the outer color (white) of the tip clearance vortices is around 98.5% of the span.

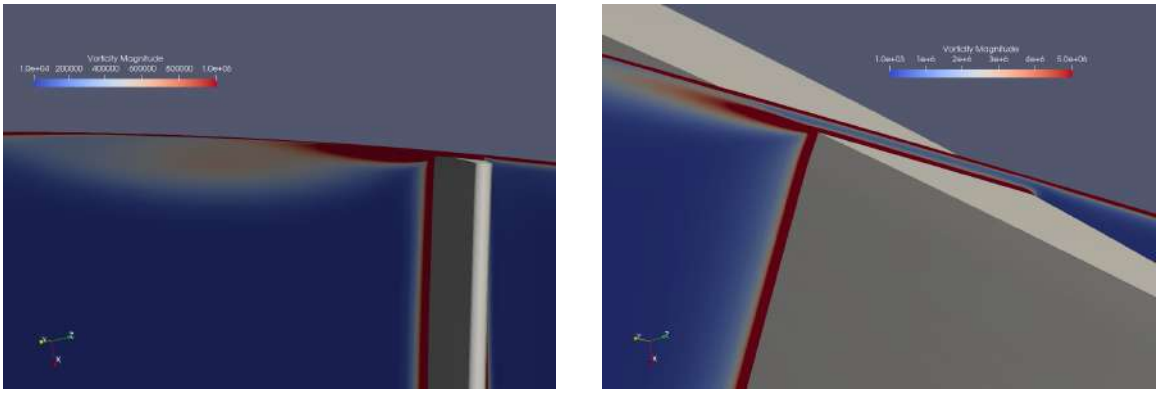

Figure 2.8: Visualization of the vorticity field at 20% chord length. The left figure shows the extent of the tip clearance vortices, while the right shows a zoomed-in view.

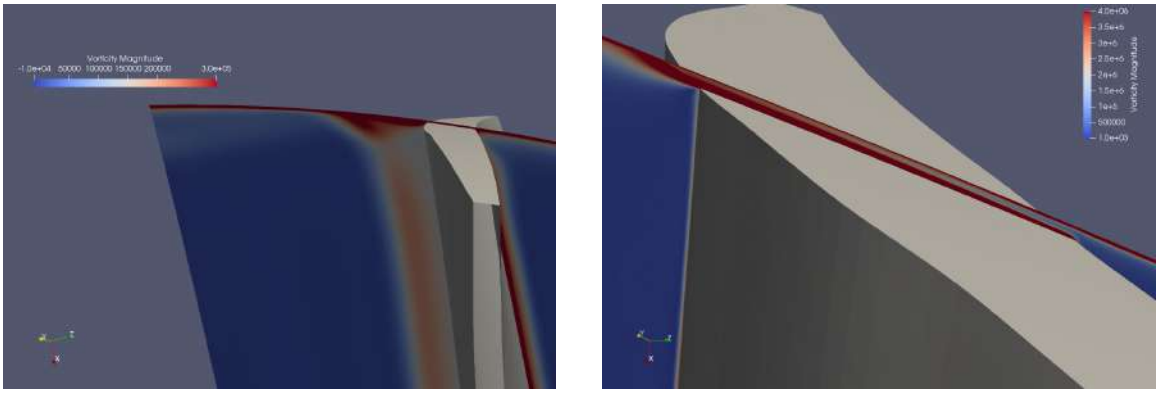

Figure 2.9: Visualization of the vorticity field magnitude, highlighting the extent and structure of tip clearance vortices from two different views at 60% length.

Figure 2.10 compares the results of PUMA with experimental data from NASA at 90% and 95% span along the axial direction, focusing on relative Mach number distributions. At the 90% spanwise location, PUMA and experimental data show good agreement, with only minor deviations, particularly noticeable after the blade, where mixing effects are likely more pronounced in the experimental setup. While the 95% span shows a slight increase in Mach number over the 90% span in the blade passage, after the trailing edge, the 90% span results show a higher Mach number compared to the 95% span. It is possible that after the trailing edge, the interaction between tip leakage vortices and the trailing edge wake enhances mixing and momentum loss, leading to a more pronounced reduction in relative Mach number. This effect could explain why the Mach number drop appears more significant in the 95% span region, where the influence of the tip leakage vortex might be more pronounced.

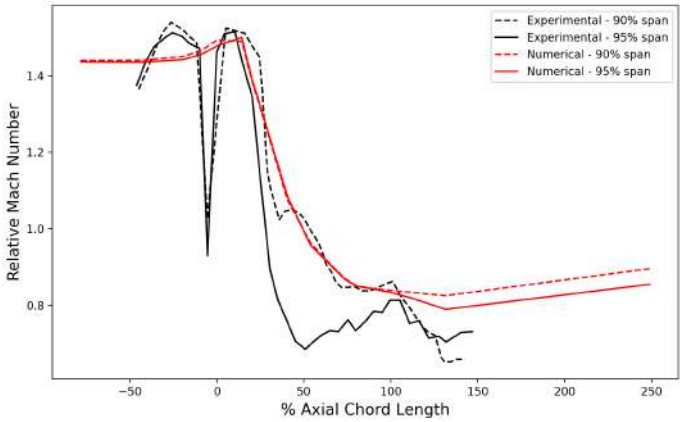

Figure 2.10: Comparison of relative Mach number between PUMA results and experimental data at 90% and 95% spanwise locations.

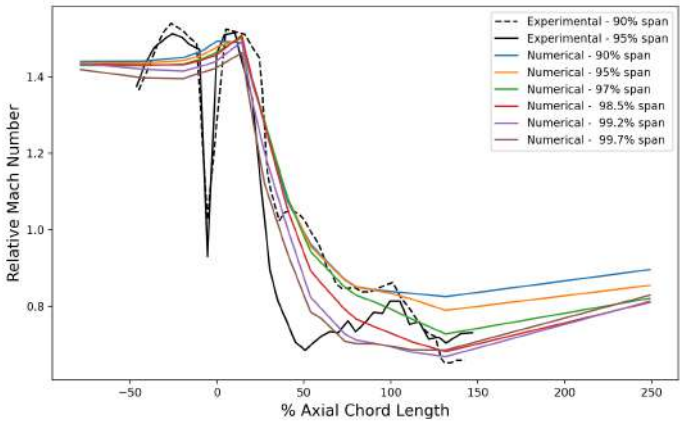

Figure 2.11: Chordwise distributions of Mach Number near the Shroud.

To further investigate this phenomenon, Figure 2.11 isolates the numerical results, focusing on identifying near-shroud regions where tip clearance vortices are expected to manifest along the z-axis and highlighting the associated changes in the relative Mach number.

By observing the relative Mach number distributions near 99% span location, we see that at 20% chord length, the only difference in relative Mach number appears at 98.5% span and above, as expected. After 50% chord length, we observe an increased deficit between 98.5% span and above, which, Figure 2.9, is due to the interaction between boundary layer vortices from the pressure side and the tip clearance vortices.

To further assess the accuracy of the numerical model by predicting the shock wave, we examine the relative Mach number distribution at 70% span and compare it with available experimental data([29]). Shock waves are expected to form when the relative Mach number drops from supersonic ($M_{rel} > 1$) to subsonic ($M_{rel} < 1$). This typically occurs first on the pressure side near the leading edge, where the flow decelerates abruptly, creating a strong gradient in relative Mach number along with other flow variables such as pressure and density. On the suction side, where the flow accelerates to higher speeds, the shock wave tends to form further downstream, usually around mid-passage. However, the exact location and strength of the shock vary depending on the spanwise position, as 3D effects like tip leakage and secondary flows influence the shock structure across different blade heights.

By comparing Figure 2.12 and Figure 2.13, which show the relative Mach number contours at 70% span, we observe good agreement with measurements, particularly near the leading edge. The contour lines in our simulation match closely with the experimental ones, although there are small differences. Some contour lines are slightly above or below the measurements by approximately 0.1, especially in the upstream regions. In the middle section of the passage, the experimental data shows relative Mach values between 1 and 0.9, whereas PUMA results exhibit slightly lower values. Despite these minor discrepancies, the overall trend and behavior of the relative Mach number contours remain consistent.

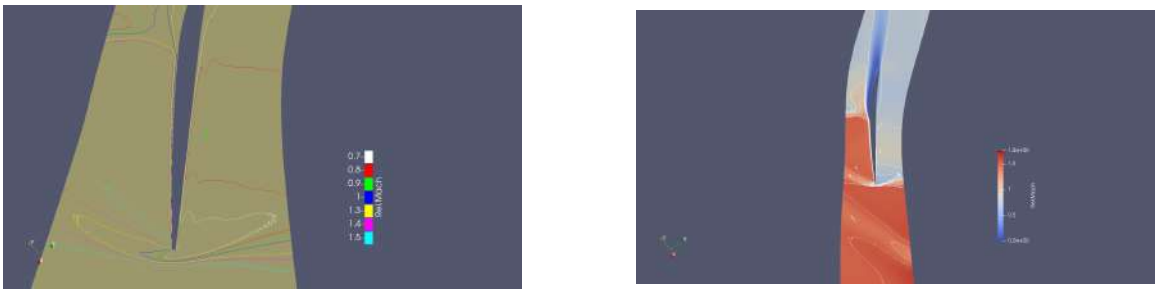

Figure 2.12: PUMA for the Relative Mach at 70% span, at near peak efficiency.

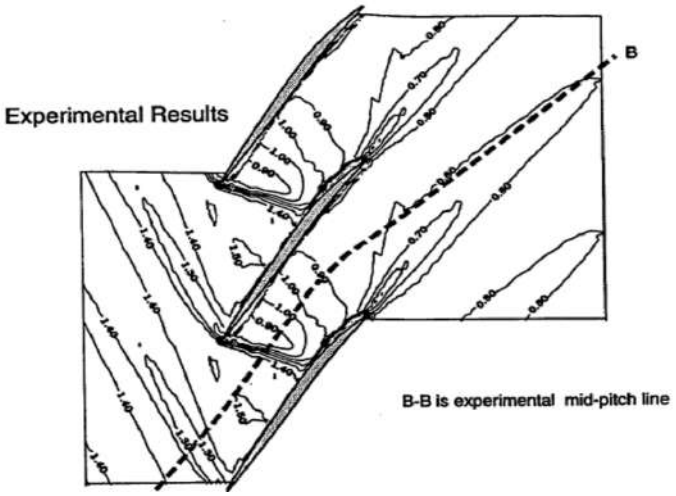

Figure 2.13: Experimental data presenting relative Mach at 70% span ([1]),at near peak efficiency.

The shock wave occurs at the leading edge, where it forms at nearly the same axial position as seen in the experiment. This is characterized by a rapid decrease in the relative Mach number contours, confirming the presence of shock waves at the leading edge. The operating point corresponding to peak efficiency typically occurs when the shock wave is located close to the blade leading edge ([5]). This relationship is crucial, as the presence and positioning of the shock wave strongly influence the flow characteristics within the blade passage. The shock wave, initiated at the leading edge, continues downstream and is observed on the suction side at about mid-chord. In this region, although the drop in the relative Mach number is less abrupt than at the leading edge, it remains significant indicating that the shock persists along the blade. The position and characteristics of this drop align well with the experimental data, thereby further validating the accuracy of the simulation.

In conclusion, this chapter presented a detailed comparison between PUMA's numerical data and measurements, with a particular focus on the investigation of tip clearance vortices. PUMA demonstrated good agreement with the experimental data in terms of total pressure rise but showed discrepancies in capturing the isentropic efficiency.

Chapter 3

Endwall Contouring - Parameterization and Mesh Displacement

The computational domain for this study is discretized using an unstructured hexahedral mesh consisting of approximately 3,200,000 nodes, with higher resolution in critical regions such as the endwall and blade passage. This mesh ensures accurate representation of the Rotor 37 flow field, capturing key aerodynamic features and gradients.

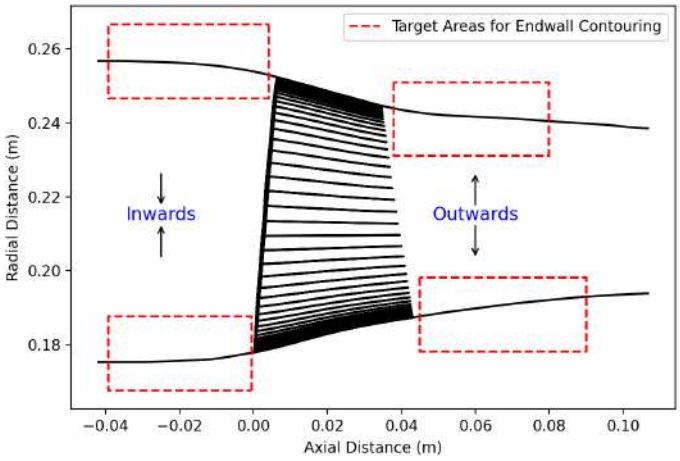

Figure 3.1: Target areas for endwall contouring on the meridional plane.

Endwall contouring is applied to all four regions outside the blade passage, covering both the hub and shroud. As shown in Figure 3.1, modifications are either inward or

outward, depending on whether the surface is displaced toward or away from the flow. These contouring strategies aim to assess their influence on secondary flow structures and overall aerodynamic performance.

For the parameterization of the endwall profile in the meridional plane, Bèzier curves are utilized to define smooth and controllable surface modifications. To transfer the displacement to the interior mesh nodes, the Radial Basis Function (RBF) ([7]) method is employed, ensuring a smooth and consistent deformation throughout the domain.

3.1 Parameterization - Endwall Profile

As a baseline, parametric Bèzier curves are used to contour the endwall geometry of Rotor 37. Simplicity as well as smoothness and continuity due to the polynomial nature of the equations makes Bèzier curves a suitable choice. Also, the axisymmetric features of the geometry render it well-suited for contouring the endwall profiles in a meridional plane (z, r).

The parametric equations for a Bèzier curve, which effectively translate the typical (x, y) coordinates of the Bèzier equations, to the meridional plane (z, r) with parameter (t), are given by:

$$z(t) = \sum_{i=0}^{n} B_i^n(t) \cdot z_i \tag{3.1}$$

$$r(t) = \sum_{i=0}^{n} B_i^n(t) \cdot r_i \tag{3.2}$$

where n is the degree of the curve, (z_i and r_i) are the control points, and $B_i^n(t)$ are the Bernstein basis polynomials defined as:

$$B_i^n(t) = \binom{n}{i} t^i (1-t)^{n-i} \tag{3.3}$$

The first derivatives of $z(t)$ and $r(t)$ with respect to t are:

$$\frac{dz}{dt} = \sum_{i=0}^{n} \frac{d}{dt}\left(B_i^n(t)\right) \cdot z_i \tag{3.4}$$

$$\frac{dr}{dt} = \sum_{i=0}^{n} \frac{d}{dt}\left(B_i^n(t)\right) \cdot r_i \tag{3.5}$$

To compute the derivatives of the Bernstein basis polynomials, we use the following formula:

$$\frac{d}{dt}\left(B_i^n(t)\right) = n\left(B_{i-1}^{n-1}(t) - B_i^{n-1}(t)\right) \tag{3.6}$$

By selecting control points with normalized z-values ranging from 0 to 1, a parametric curve is defined, that essentially maps the axial position of each node to a radial displacement $\Delta r = r(t)$. In particular, by setting the limits on the z-axis case we need to solve the inverse problem of Eq. (3.1) by calculating the parameter t for the given axial position (z) of a node inside these bounds.

Figure 3.2-Figure 3.5 show a parametric Bèzier curve which defines the modified endwall profiles for all four regions outside the passage. Each set consists of two views: one in the meridional plane illustrating the imposed parameterization and one in 3D highlighting the deformed surface. At this point, the direction of the imposed modification is chosen arbitrarily for demonstration purposes, including all the different regions.

Figure 3.2: Parameterization of the endwall in the hub upstream region. On the meridional plane (left) and a 3D view (right).

Figure 3.3: Parameterization of the endwall in the hub downstream region. On the meridional plane (left) and a 3D view (right).

Figure 3.4: Parameterization of the endwall in the shroud upstream region. On the meridional plane (left) and a 3D view (right).

Figure 3.5: Parameterization of the endwall in the shroud downstream region. On the meridional plane (left) and a 3D view (right).

Note: The displacement calculated primarily affects the $r - axis$ but will also have minor adjustments along the $z - axis$ based on the unit normal vector of each mesh node.

3.2 Mesh Deformation via Interpolation Techniques

For the interpolation of the boundary displacement (Δr) to the internal nodes, RBF (Radial Basis Function) will be used ([7]). The RBF method is appropriate for the reason of producing smooth and continuous interpolation and handles efficiently unstructured data meshes. The high computational cost is mitigated by localizing RBF to smaller regions.

Radial basis functions are real-valued functions $\phi : \mathbb{R} \to \mathbb{R}$ depending only on the distances of a point $x \in \mathbb{R}^Q$ from the so-called RBF interpolation sources $x_n \in \mathbb{R}^Q, n \in [1, N]$.The RBF deformation function $d : \mathbb{R}^{\mathbb{Q}} \to \mathbb{R}^{\mathbb{Q}}$ takes the form :

$$d(x) = \sum_{i=1}^{N} c_n \phi(||x - x_n||)$$

where $||\cdot||$ is the Euclidean distance, and the coefficients $c_n \in \mathbb{R}^{\mathbb{Q}}$ are computed so as to correctly reproduce the imposed displacements $d(x_n) = \delta_n \in \mathbb{R}^{\mathbb{Q}}, \forall n \in [1, N]$ at the source nodes; this requires the numerical solution of an $N \times N$ linear system.

In simple terms, RBF works by making the displacement of interior nodes depend on their distance from the boundary nodes. The known displacement at the boundary nodes is used to determine the weights of the interpolation, ensuring that the deformation spreads smoothly across the entire domain.

3.3 Mesh quality

To assess the mesh quality after any mesh displacement, three metrics are compared with those the original mesh:

1. Non-orthogonality, representing the deviation angle between the normal vector of a shared face and the vector connecting the centroids of two neighboring cells. It is expressed as:

$$\text{Non-orthogonality} = \cos^{-1}\left(\frac{\vec{n}\cdot\vec{c}}{|\vec{n}||\vec{c}|}\right)$$

   where:

   - $\vec{n}$ is the normal vector of the shared face between the two neighboring cells,
   - $\vec{c}$ is the vector connecting the centroids of the two cells.

2. Equiangle Skewness([**Ansys2011**]), which measures the angular deviation from ideal geometry. For hexahedral cells, skewness reflects the deviation from a perfect cube, and is expressed:

$$\text{Equiangle Skewness} = max(\frac{\theta_{max} - 90}{90}, \frac{90 - \theta_{min}}{90})$$

   where :

   - $\theta_{\max}$ is the maximum internal angle between adjacent cell faces,
   - $\theta_{\min}$ is the minimum internal angle between adjacent cell faces.

3. The determinant of the Jacobian matrix, $\det(J)$, ensuring $\det(J) > 0$ for all cells to avoid negative values that indicate cell inversion.

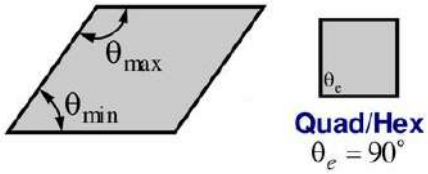

Figure 3.6: Equiangle Skewness.

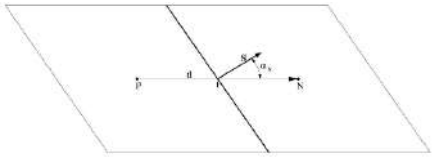

Figure 3.7: Non-orthogonality.

The comparison of these values with the original mesh will focus on a region influenced by the interpolation, containing approximately 53000 hexahedral elements, and is presented below :

Height(ΔR)		Non-Orthogonality	Equiangle Skewness	det J
Absolute (m)	Relative %	Average | Max		+ | -
ΔR= 0		48.40 | 65.28	0.536 | 0.730	+
ΔR= 0.002	1.5%	48.49 | 65.12	0.534 | 0.730	+
ΔR= 0.005	5 %	49.06 | 65.05	0.523 | 0.730	+
ΔR= 0.01	10 %	52.03 | 67.24	0.488 | 0.728	+
ΔR= 0.02	20 %	56.33 | 89.989	0.543 | 0.996	-

Table 3.1: Mesh quality metrics for various height modifications (ΔR) applied to the geometry.

For a hub modification height of approximately 10% of the rotor's overall height, the quantitative results show that the interpolation performs smoothly, with minimal degradation in these metrics and even slight improvements in some cases. However, visual inspection reveals areas where the mesh does not appear well-formed, indicating potential local issues. To address this, a maximum modification height of around 10% is selected as the standard for this study. This ensures reliable interpolation and maintains acceptable mesh quality. Achieving greater effectiveness in the interpolation, particularly for smooth transitions and diminishing displacements within the nodes, would require a significantly higher number of nodes to capture the finer details of deformation and improve the overall smoothness of the displacement field.

Chapter 4

Parametric Study of NASA Rotor 37 Endwall Regions

The goal of this thesis is first to study the influence of modifying the hub and shroud geometry outside the blade passage on Rotor 37's performance by applying arc-shaped contouring.

In this study, by contouring the endwalls outside the blade passage, relatively small differences in aerodynamic performance are expected. Given the significant cost and time associated with each computational run, it is essential to carefully select parameters and isolate individual regions. One key reason for this study, beyond further optimization, is to assess how each region responds to the height variations, understanding how the contouring modifications interact with the flow. Additionally, through optimization, the aim is to explore how adjustments to the curvature's slope (i.e., the angle of the Bèzier curve) influence aerodynamic performance, offering a more detailed understanding of the curve's impact on the overall rotor performance.

4.1 Parametric Study: Set up - Results

To investigate the effects of endwall contouring, the parametric study will begin by isolating individual regions of the hub and shroud-both upstream and downstream-and applying modifications independently. This systematic approach allows for a focused evaluation of the aerodynamic impact of contouring in each region, with the simulations conducted near the peak efficiency operating point of the rotor to identify how the contouring modifications affect aerodynamic performance under typical, high-efficiency operating conditions.

The aerodynamic performance of the rotor with contouring modifications is evaluated based on isentropic efficiency and total pressure. These parameters offer insight into

the efficiency of the flow process and the rotor's ability to maintain pressure across the modified endwall regions. By analyzing these results, the impact of the contouring on overall performance can be assessed and a foundation for further investigation be established.

Three curvature heights are tested for each region of the hub and shroud, encompassing both upstream and downstream sections. The curvature heights are defined as percentages of the respective cross-sectional height, and the orientation of the curvature alternates between positive and negative, with positive curvatures directed outward from the rotor and negative curvatures directed inward. These modifications are applied using a symmetrical Bèzier curve as the parameterization, ensuring smooth transitions in the geometry for all three curvature heights in each region.

- Upstream region: Curvature heights are based on the inlet span of the rotor.
- Downstream region: These correspond to the outlet span of the rotor.

The specific maximum heights of the contoured geometry, located at the midpoint of the Bèzier curve, correspond to:

- 2% of the corresponding span.
- 4% of the corresponding span.
- 6% of the corresponding span.

2% Height - Endwall Contouring

In this section, we explore the impact of applying a span of 2% height to the endwall geometry. This value represents a relatively modest modification to the original surface, serving as a starting point to observe the effects of contouring on flow characteristics. By comparing it to larger curvatures (4% and 6%), how increasing curvature height influences flow behavior and aerodynamic performance.

Figure 4.1 shows all the 2%-height modifications applied across all regions at once, providing a comparison of the impact of this height relative to the entire geometry.

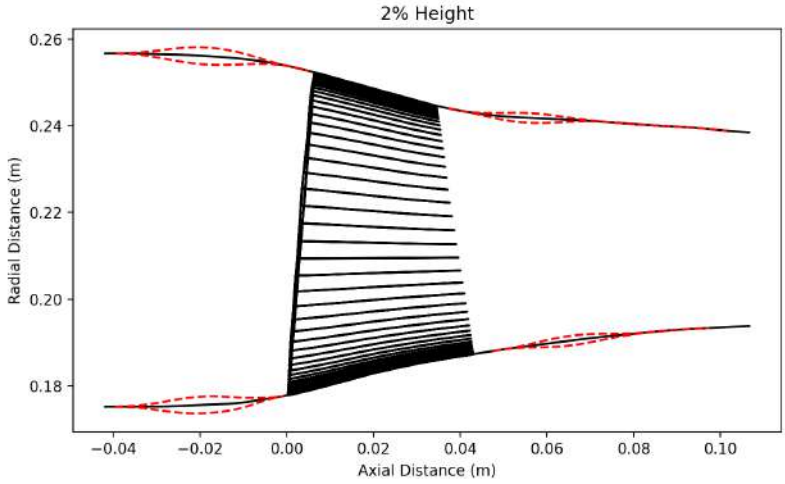

Figure 4.1: All 2% height curvature modifications applied across the different regions of the endwall, shown in the meridional plane.

The results for the first tested curvature height are presented below, focusing on the hub upstream and downstream regions. For both regions, the inward and outward orientations demonstrated performance levels similar to the baseline, with only minor drops observed in isentropic efficiency or total pressure. Figure 4.2 and Figure 4.3 are provided for reference.

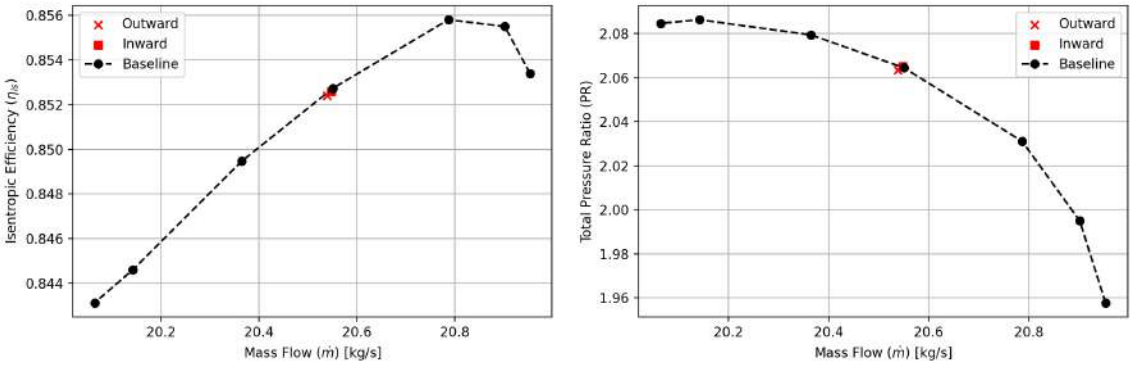

Figure 4.2: Impact of 2% Height Modifications in the Upstream Hub Region.

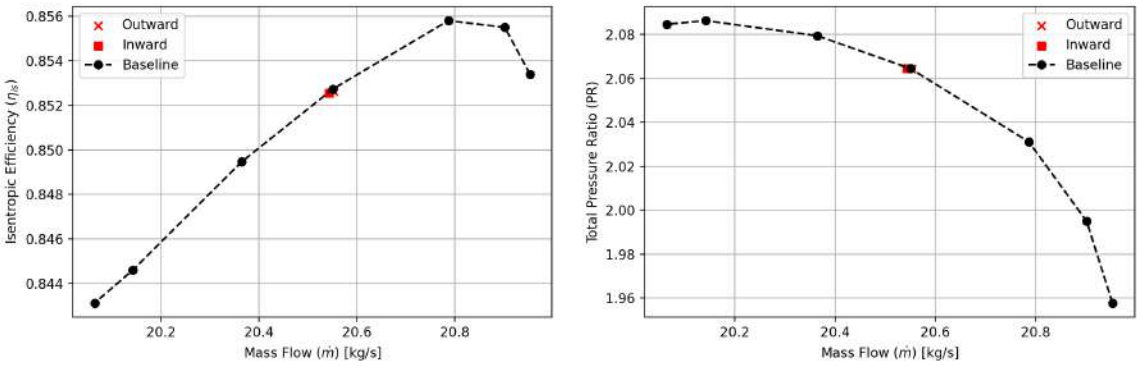

Figure 4.3: Impact of 2% Height Modifications in the Downstream Hub Region.

For the shroud, an improvement over the baseline was observed in both isentropic efficiency and total pressure for the upstream outward orientation. Conversely, the downstream upstream orientation exhibited notable negative results in both metrics. The shroud downstream region, however, showed performance levels consistent with the baseline, with the inward orientation increasing only slightly isentropic efficiency. Figure 4.4 and Figure 4.5 illustrate these trends.

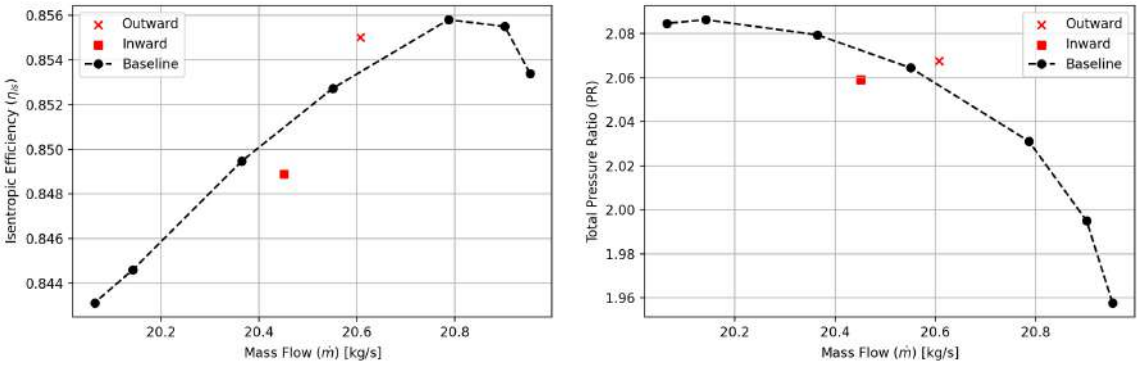

Figure 4.4: Impact of 2% Height Modifications in the Upstream Shroud Region.

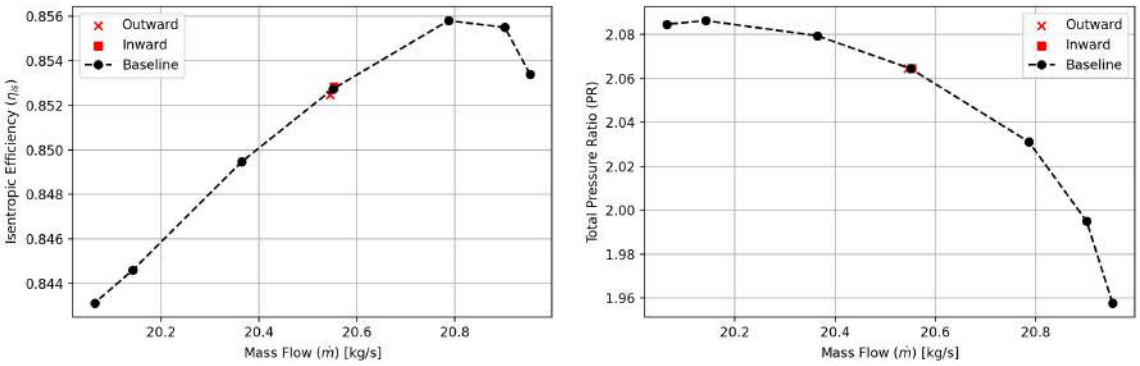

Figure 4.5: Impact of 2% Height Modifications in the Downstream Shroud Region.

4% Height - Endwall Contouring

In this section, we examine the effects of applying a 4% height contouring modification to the endwall geometry. This increased curvature is expected to amplify the flow redistribution observed in the previous section, offering deeper insights into how larger adjustments influence aerodynamic performance.

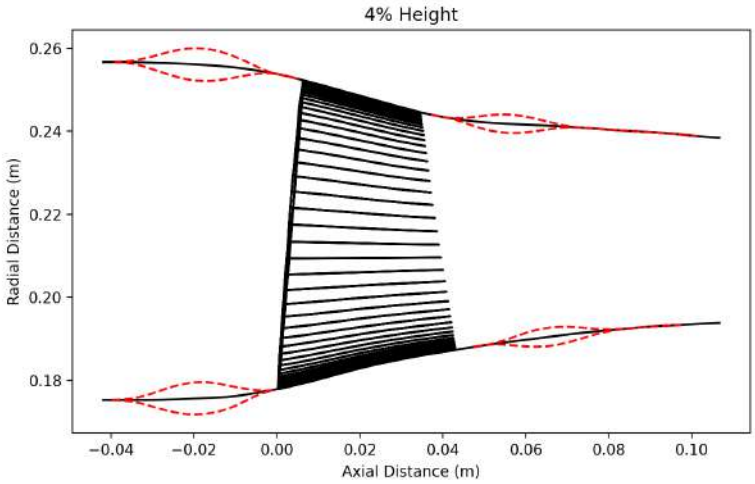

Figure 4.6: All 4% height curvature modifications applied across the different regions of the endwall, shown in the meridional plane.

For the 4% height modifications applied to the hub, both upstream and downstream, we observed a decline in isentropic efficiency as the height increased. Despite the rotor performing the same amount of work, the flow exhibited higher losses, likely due to the increased height of the contoured geometry.

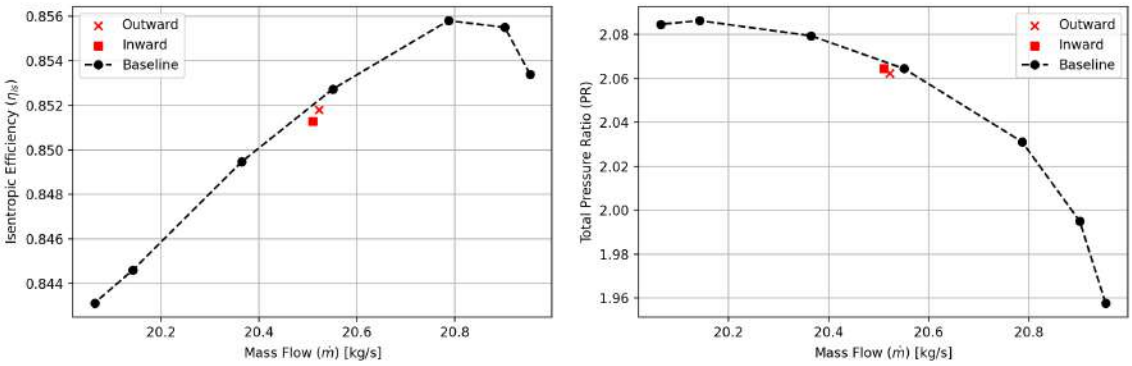

Figure 4.7: Impact of 4% Height Modifications in the Upstream Hub Region.

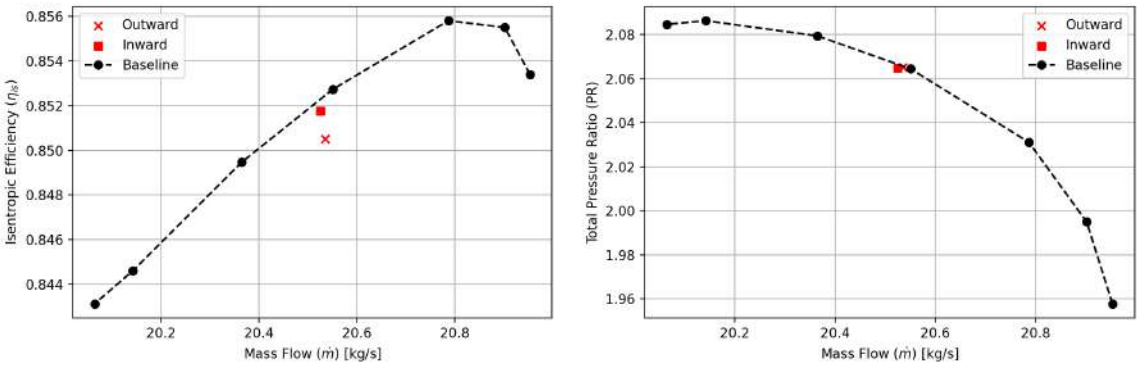

Figure 4.8: Impact of 4% Height Modifications in the Downstream Hub Region.

For the shroud modifications downstream, similar to the hub adjustments, the results showed a decline in isentropic efficiency despite the total pressure work remaining constant. Conversely, the upstream shroud modifications exhibited contrasting behavior: the outward-oriented contour yielded slightly improved results with increased height, while the inward-oriented contour suffered significantly. Given the poor performance observed, it is assumed that severe loss mechanisms are at play, potentially including reverse flow, increased vorticity, or other inefficiencies.

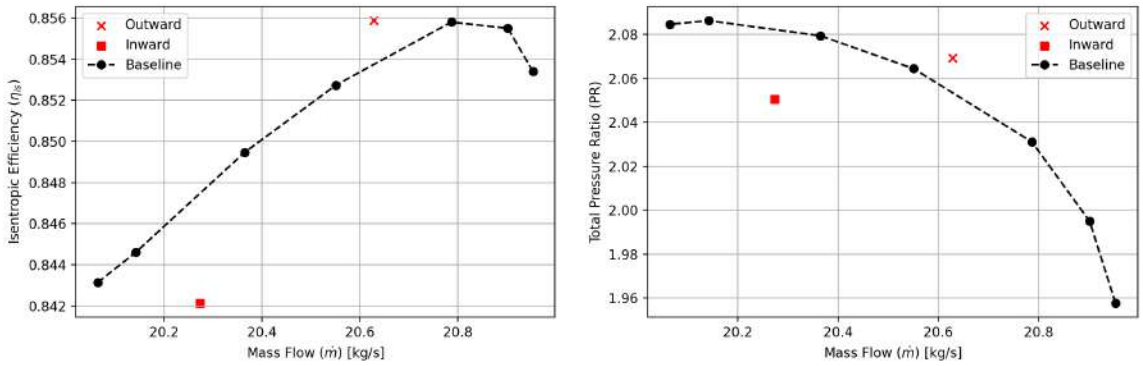

Figure 4.9: Impact of 4% Height Modifications in the Upstream Shroud Region.

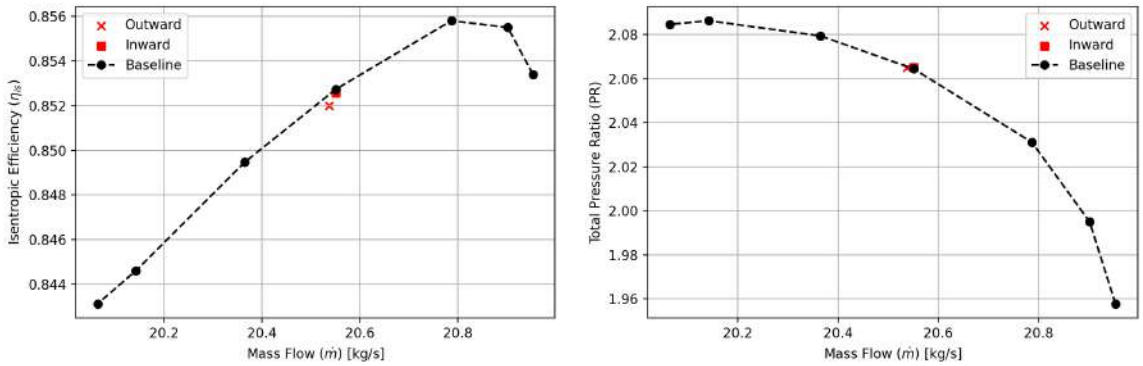

Figure 4.10: Impact of 4% Height Modifications in the Downstream Shroud Region.

6% Height - Endwall Contouring

The investigation into the 6% height modifications provided further insights into the influence of pronounced geometric alterations on the flow dynamics and overall performance. By increasing the height of the hub and shroud contours, the study aimed to understand the extent to which these changes impact isentropic efficiency and total pressure ratio.

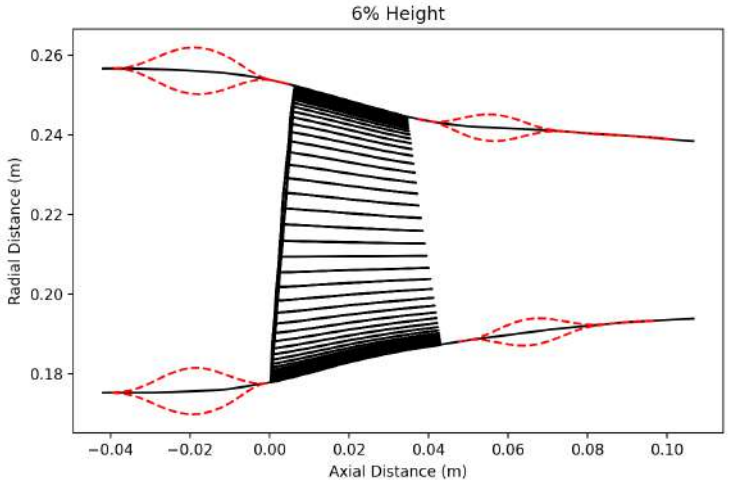

Figure 4.11: All 6% height curvature modifications applied across the different regions of the endwall, shown in the meridional plane.

Below, we observe the results of the 6% height contour modifications applied to the hub, both upstream and downstream. In both cases, the increased height appears to worsen the performance, with a decline in isentropic efficiency. This degradation is likely tied to increased secondary flow effects and boundary layer interaction, which intensify as the contour height increases.

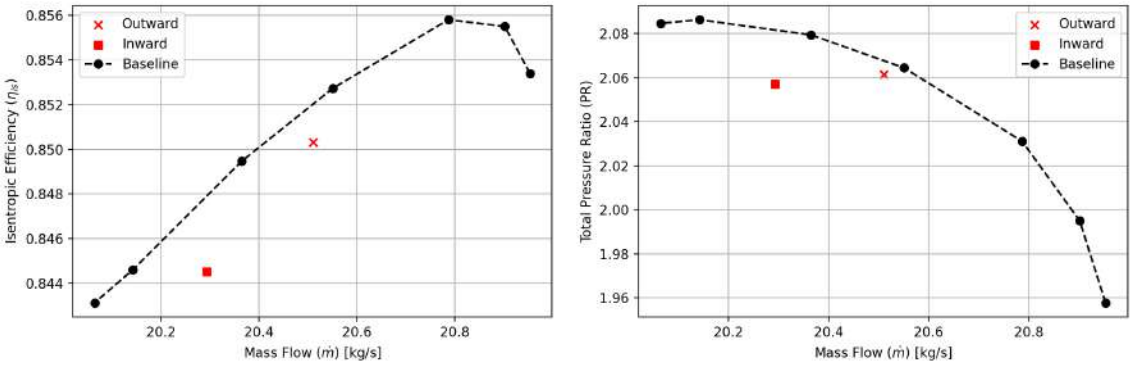

Figure 4.12: Impact of 6% Height Modifications in the Upstream Hub Region.

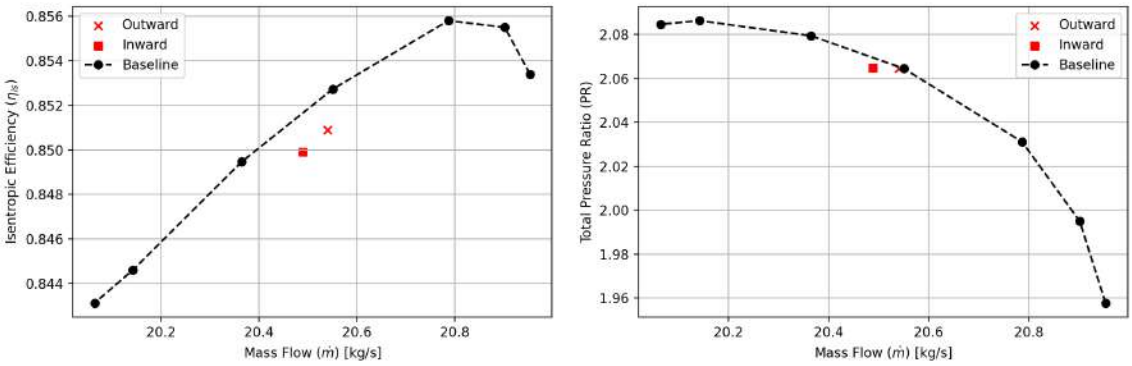

Figure 4.13: Impact of 6% Height Modifications in the Downstream Hub Region.

For the shroud downstream, we observe a similar pattern of increased losses, reflected in reduced isentropic efficiency, while the total pressure remains unchanged. On the other hand, the outward-oriented shroud modifications show slight improvement in performance with increased height. However, the inward-oriented shroud contour suffers significant performance degradation, likely due to the occurrence of reverse flow and associated losses.

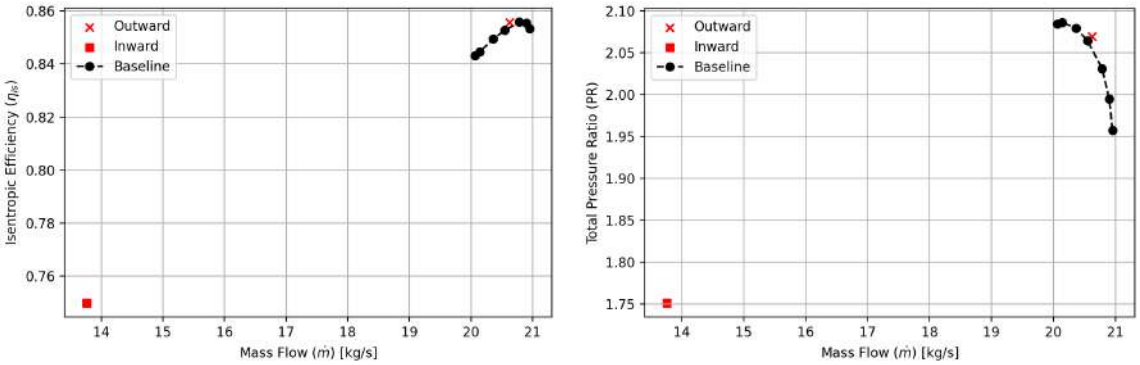

Figure 4.14: Impact of 6% Height Modifications in the Upstream Shroud Region.

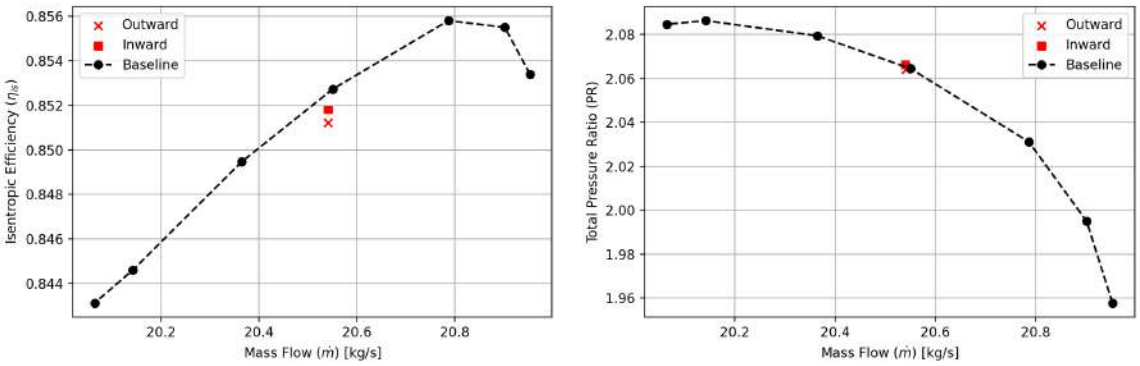

Figure 4.15: Impact of 6% Height Modifications in the Downstream Shroud Region.

4.2 Overall Summary of Parametric Stuies on Contour Heights

- **General Trend Across All Heights:**
  In all regions except shroud upstream and across all tested contour heights, the trend of increased losses in isentropic efficiency was observed, with most regions maintaining similar total pressure levels. The aerodynamic performance, in terms of total pressure, generally remained stable despite increased losses, indicating that while the height of the contour impacted efficiency, the overall work output remained largely unaffected.

- **Hub Regions (Upstream and Downstream):**
  As the height of the contour increased in either the inward or outward direction, both upstream and downstream regions of the hub showed worsened isentropic efficiency. The higher contour height likely induced stronger flow separation and led to increased secondary flows, thereby increasing losses while maintaining a constant total pressure. This suggests that contour heights in these regions might need to be limited for optimization.

- **Shroud Downstream:**
  Similar to the hub regions, the downstream shroud experienced worsened isentropic efficiency with increased height, although total pressure remained unchanged. This further supports the idea that while higher contours may not necessarily affect total pressure, they result in greater flow losses and reduced performance in some areas.

- **Shroud Upstream (Outward Orientation):**
  The most notable positive result was seen in the outward-oriented shroud upstream region. At all heights, there was a slight improvement in isentropic

efficiency, with performance increasing as the contour height increased. This suggests that optimization in this region could be a promising direction, with the increased height leading to enhanced flow behavior.

- **Shroud Upstream (Inward Orientation):**
  The inward-oriented contour in the upstream shroud region showed dramatically worse performance. Not only did the efficiency decrease significantly, but signs of reverse flow were also observed, indicating severe flow disruption. This suggests that inward-oriented contours should be avoided for optimization, as they cause significant performance degradation.

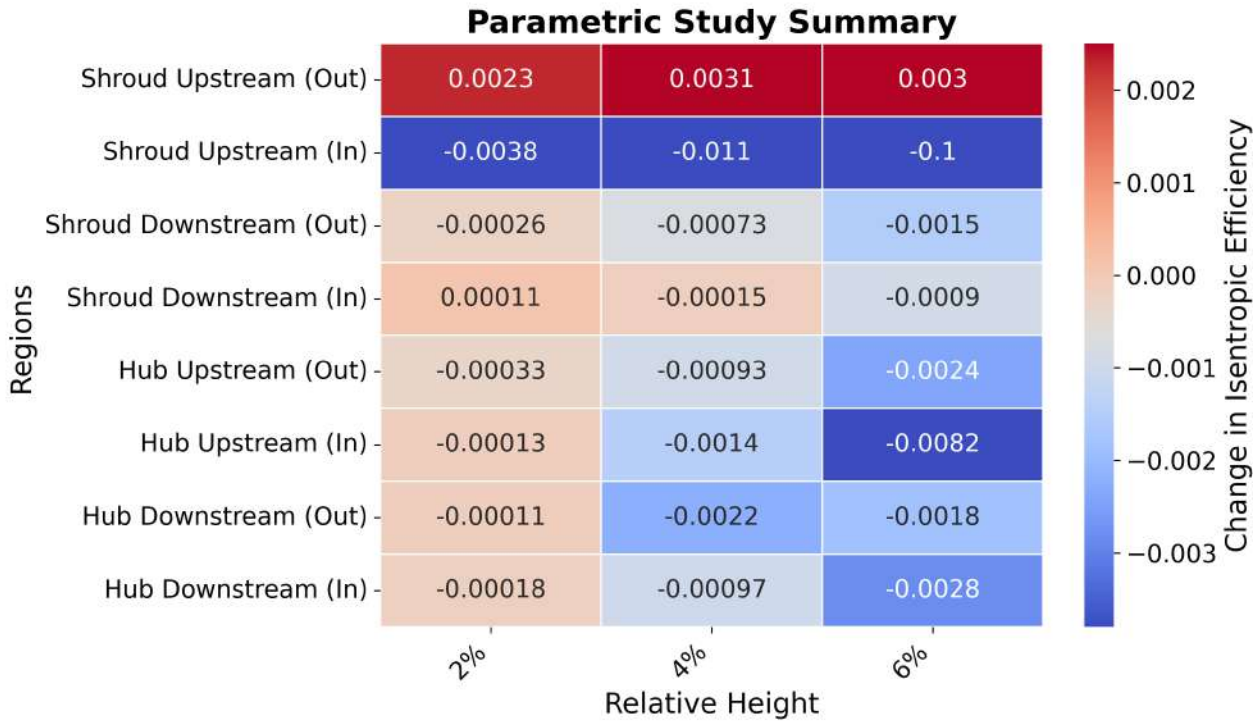

Figure 4.16: Heatmap of Isentropic Efficiency differences from baseline values for different regions and directions. The values on the heatmap represent the deviation in performance, highlighting regions where efficiency differs from the baseline at the varying heights (2%, 4%, 6%).

Conclusion:
The results of this parametric study suggest that optimization efforts should focus on the **shroud upstream region**, particularly with an **outward** orientation, where the increased contour height showed positive results. In contrast, both the hub regions and the inward-oriented upstream shroud exhibited increased losses, making these areas less suitable for height modifications.

Chapter 5

Optimization of Upstream Shroud Endwall Geometry

In this study, optimization of the rotor geometry is performed using a derivative-free approach, specifically, Evolutionary Algorithm Optimization, implemented through EASY, a generic optimization platform developed by PCOpt/NTUA([9]). EASY is a powerful and versatile tool designed for solving both single and multi-objective optimization problems, including those with constraints. It employs a (μ, λ) EA approach, with μ parents and λ offspring, and supports advanced features such as distributed, asynchronous, and hierarchical evolutionary strategies to enhance optimization performance (not used in the performed optimization runs).

Additionally, EASY is distinguished by its unique use of on-line trained personalized metamodels to reduce the computational cost of repeated evaluations, leading to the concept of Metamodel-Assisted Evolutionary Algorithm (MAEA)([14]). In this framework, built-in Radial Basis Function (RBF) networks are utilized as surrogate models to replace many calls to the computationally expensive evaluation tool.

The optimization aims to maximize isentropic efficiency near the operating point of peak performance while ensuring the total pressure remains within acceptable limits. Furthermore, the objective of this optimization is twofold. First, to assess the performance of the contoured shroud upstream geometry (outward) and determine whether it offers improvements or drawbacks in terms of rotor efficiency and flow characteristics. Second, to analyze the convergence of design variables, providing insights into their influence and allowing a comparison with the symmetric configuration at a similar height.

5.1 The Optimization Set-up

5.1.1 Design Variables

The design variables are derived from the Bèzier curves used for parameterizing the rotor geometry. The total number of design variables is seven. Two of these variables correspond to the starting and ending limits along the z-axis, while one variable is used to define the height along the r-axis. The remaining four variables are dimensionless, falling within the specific limits, and are used to adjust the intermediate points along the Bèzier curve. These variables collectively control the shape of the rotor's endwall, enabling optimization of the rotor's performance.

The starting and ending variables are controlled within the upstream region of the shroud, which is divided into four segments. The first quarter of the region defines the starting variable, while the last quarter defines the ending variable. This approach is designed to prevent the curve from becoming too steep, as overly steep curves could lead to undesirable results in the interpolation process, potentially causing inaccuracies or instability in the design.

5.1.2 Optimization Settings

The optimization algorithm incorporates elitism to retain the best-performing solutions and employs tournament. The algorithm's setup parameters are summarized in the tables Table 5.1,Table 5.2. In this optimization process, a MAEA is utilized, with an RBF-based metamodel to predict solutions. The metamodel uses a database with a minimum of 120 entries to ensure sufficient accuracy in the predictions.

Parameter	**Value**
Elites to Keep (Max Archive Size)	5
Elite Individuals to Force as New Offspring	1
Probability to Select an Elite	0.2
Tournament Size	5
Tournament Probability	0.90
Selection Mechanism	Tournament

Table 5.1: Key parameters related to the selection mechanism for the EA.

Parameter	Value
Parents Population Size (μ)	20
Offspring Population Size (λ)	40
Recombination Factor (ρ)	3
Mutation Probability	0.03
Crossover Probability	0.85

Table 5.2: Population parameters for the EA.

5.2 Optimization Results

PUMA provides us with the capability to initialize the computational field from previous simulations, streamlining the convergence process. Using results from the baseline mesh as the initial condition, the simulations converged to a criterion of 10^{-4} in isentropic efficiency, requiring approximately 1 hour and 10 minutes per case, leveraging the power of the NVIDIA Tesla P100 GPU.

The optimal design achieved an isentropic efficiency of 85.7% with a total pressure ratio of 2.07, demonstrating the improvement achieved through the optimization process. Compared to the baseline configuration, this represents an increase of 0.37% in isentropic efficiency. To provide a comprehensive understanding of the optimization process, the following figures illustrate the convergence and highlight the design variables for all evaluations throughout the optimization process.

Figure 5.1 provides an overview of the optimization process with its outcomes. The scatter plot presents the isentropic efficiency of all tested designs relative to the baseline. It is evident that every optimized design achieved an efficiency above the baseline value, underscoring the effectiveness of endwall contouring of the shroud geometry upstream of the rotor. Even the less optimal designs outperformed the initial configuration, reinforcing the overall benefit of the optimization approach.

Also, from the very first evaluation, we already see about one-third of the total improvement achieved by the best-performing design. While most designs resulted in only moderate gains, the overall trend confirms that upstream geometry modifications positively impact rotor performance. Notably, very few designs performed worse than the baseline, indicating that the optimization process consistently led to improvements, even if the degree of enhancement is small.

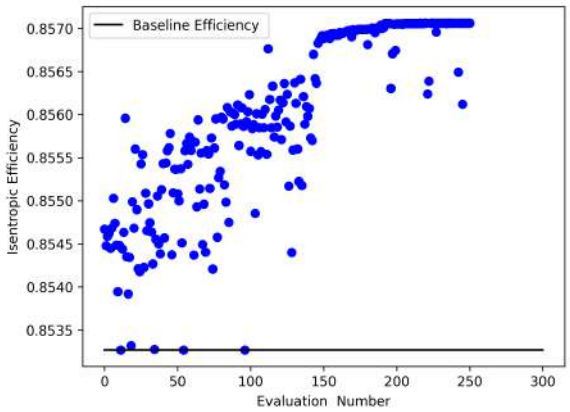

Figure 5.1: Scatter plot of all evaluations compared to the baseline.

Interestingly, by inspecting Figure 5.2, which depicts the starting and ending points of the parametric curve along the z-axis, we observe that both values converge toward their respective minimum and maximum limits. This convergence suggests that the optimization process effectively stretches the curve along the z-axis while ensuring a smoother overall shape. Notably, the convergence of the ending point indicates that the optimization is fully utilizing the available design space. This implies that further improvements could be achieved if the design constraints were relaxed, allowing the optimization to push the geometry closer to the blade, where flow interactions become more pronounced and influential.

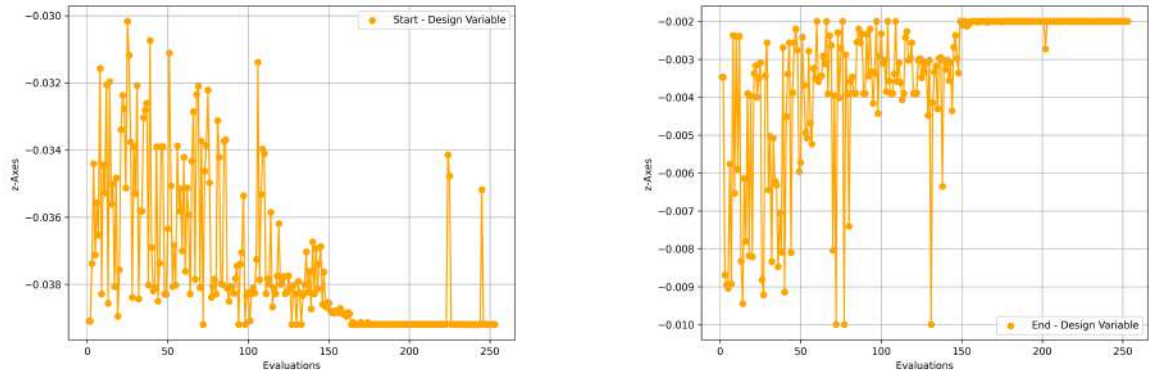

Figure 5.2: Left: Convergence of Starting point design variable with limits $(-0.0392, -0.03)$. Right: Convergence of Ending point design variable with limits $(-0.01, -0.002)$.

Figure 5.3 illustrates the convergence of the height, which is one design variable applied to the two middle Bèzier points to create a smooth contoured curve. The height is described in terms of the percentage of the inlet rotor height.

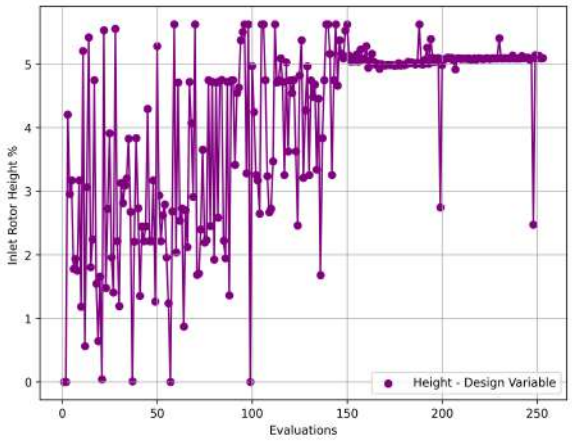

Figure 5.3: Convergence of the Height Design Variable in Terms of Percentage of Rotor's Inlet Height

Figure 5.3 reveals that the inlet height initially increases toward the maximum percentage, indicating a trend to maximize the height within the design space. However, as the optimization progresses, the height converges slightly below the maximum, suggesting that while a larger height provides certain aerodynamic advantages, the optimization ultimately balances this with other constraints and objectives. This indicates that further exploration of the effects of height beyond this range could reveal additional nuances in the relationship between geometry and performance.

The figures below expand on this analysis by focusing on the intermediate Bèzier points, which are normalized design variables defined by the start and end design variables that set the boundaries along the z-axis. Figure 5.4 illustrates the convergence behavior of the first two intermediate points (ranging from 0 to 0.5), while Figure 5.6 presents the convergence of the remaining two design variables (ranging from 0.5 to 1).

Moving the first intermediate design variable near 0, results in the curve becoming steeper at the starting point of the contoured curve, which helps introduce more aggressive flow turning. While the rest of the first half of the contoured curve gets more outward "ballooned" creating a more gradual and smooth transition in the flow. For the next intermediate point, we see it move slightly nearer to 0.5, shifting the curve's symmetry slightly to the right.

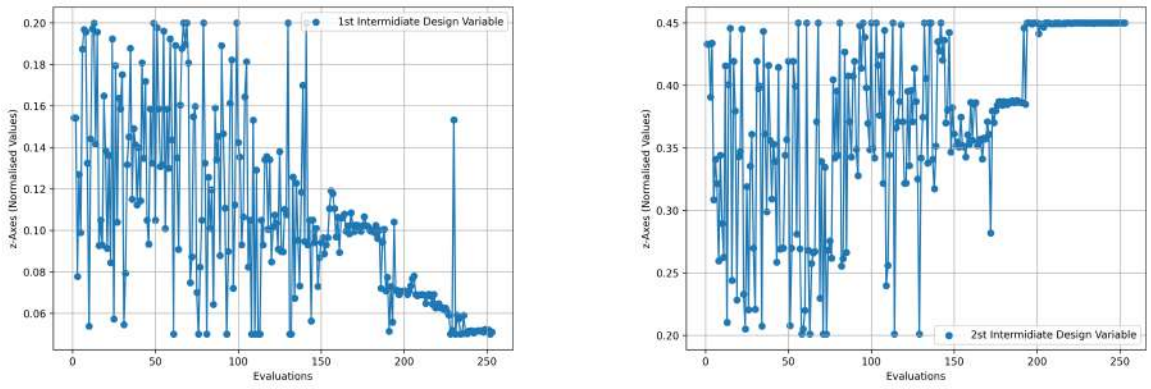

Figure 5.4: Convergence of the first two normalized intermediate design variables, positioned to the left of the symmetry axis with corresponding limits $(0.05, 0.2)$ and $(0.2, 0.45)$.

Figure 5.5, on the left, the effect of adjusting the first design variable, and on the right, the change resulting from the second design variable.

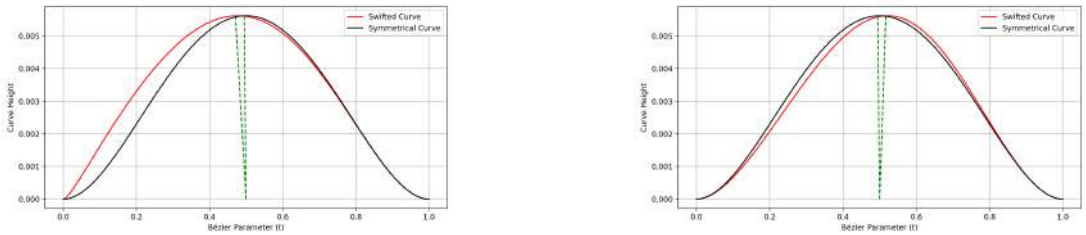

Figure 5.5: Effect of the intermediate design variables on the Bézier curve and flow characteristics. The first variable steepens the curve at the start, increasing flow turning, while the second shifts the curve slightly right, modifying the shape and transition behavior.

Figure 5.6, analyzes the effect of the 3rd and 4th intermediate design variables on the Bèzier curve, particularly focusing on how these variables influence the curve's shape on the right side. As the 3rd design variable reaches a value of 0.7, it introduces a further tilt to the right, shifting the symmetry of the curve toward the right side.

The 4th design variable, approaching its maximum value of 0.95, counteracts the tilt caused by the 1st design variable on the left while also making the curve more "ballooned" at both ends.

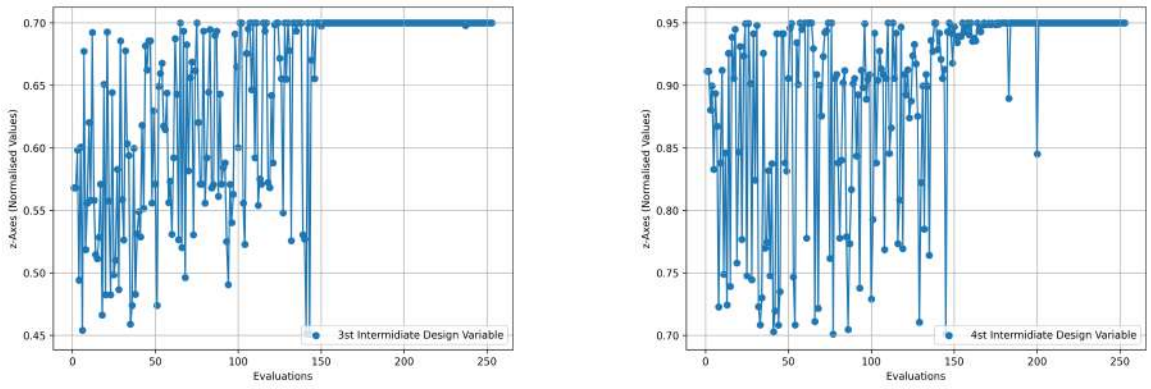

Figure 5.6: Convergence of the first two normalized intermediate design variables, positioned to the left of the symmetry axis with corresponding limits of $(0.45, 0.7)$ and $(0.7, 0.95)$.

Figure 5.7 demonstrates the overall reshaping of the curve, showcasing the cumulative effects of these intermediate design variables and their influence on the curve's final form. This is also illustrated in the figures of the Rotor 37 in the meridional plane, where the changes in shape are visualized on the rotor's endwall, highlighting how the curve adapts across the rotor geometry.

Figure 5.7: Comparison of the Bézier curve optimization (left) and the impact on the shroud meridional profile (right) in the upstream region of the shroud.

This overall reshaping indicates that the flow is directed more smoothly along the contoured surface, minimizing abrupt directional changes. The altered curvature further suggests an increase in radial velocity relative to axial velocity at the exit, potentially redistributing the flow to favor the middle sections of the passage. This could alleviate the high-loss regions near the top sections by reducing the adverse effects of secondary flows and improving overall flow uniformity.

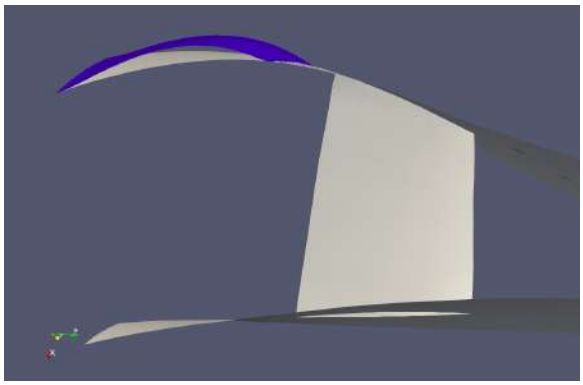

Figure 5.8: 3D representation of optimized shroud geometry.

Summary of Optimization Findings

The optimization process yielded consistent positive results across all runs, as suggested by the parametric study. Although the improvements were small, they collectively contributed to measurable performance gains, including a **0.37% increase in isentropic efficiency**.

A closer analysis of the design variables revealed several key trends:

- **Intermediate Design Variables:** The optimized distribution of intermediate design variables resulted in a smoother curvature of the shroud. This reshaping directed the fluid toward a more radial path, aligning with the intended aerodynamic characteristics.
- **Start and End Design Variables:** Both the start and end design variables converged at their respective maximum values, starting earlier near the inlet and extending later near the outlet. This suggests that the optimization favored shaping the curve more prominently at the beginning and end, enhancing flow control at these critical regions.
- **Height Design Variable:** Interestingly, the height design variable did not converge to its anticipated value, warranting further investigation. This raises questions about whether the new direction introduced by the reshaped geometry might be leading to excessive losses, or if the losses originate earlier in the flow.

Overall, the optimization reshaped the shroud to create a smoother transition for the flow, minimizing abrupt directional changes and promoting smoother flow paths. This also indicates a potential redistribution of the flow, possibly directing more mass through the midsection rather than the top region where losses are typically higher.

5.3 Further Analysis of Optimized Geometry

After completing the parametric study and optimization process, the next step is to analyze the operating line of the optimized rotor geometry and compare it to the baseline configuration. The operating line represents the relationship between mass flow and the pressure ratio (or total pressure), showing how the system performs across different operating points. This comparison provides insight into how the optimized geometry affects the system's behavior, particularly in terms of isentropic efficiency, total pressure, and mass flow distribution.

5.3.1 Comparison of Flow Variables

The operating points for both the baseline and optimized geometries are determined based on the outlet boundary condition, specifically the radial distribution of static pressure at the exit. This boundary condition ensures that the comparison of operating lines reflects the actual behavior of the rotor at various mass flow rates and pressure ratios.

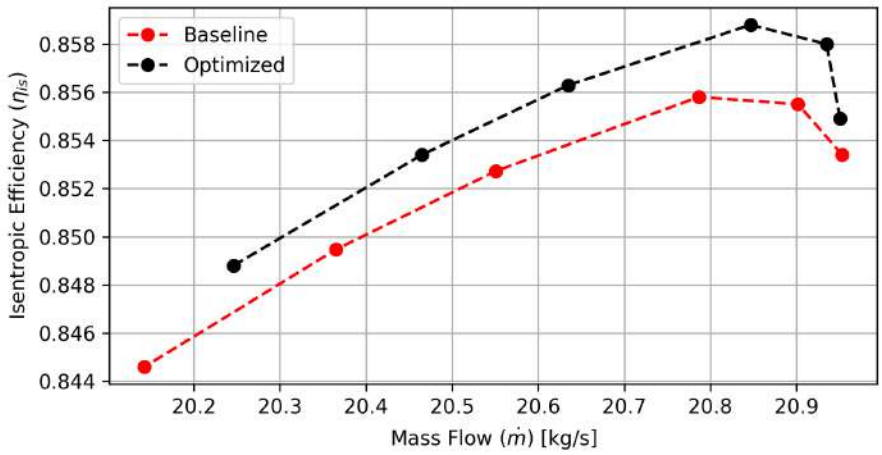

Figure 5.9: Comparison of isentropic efficiency across operating points for the baseline and optimized geometries.

According to Figure 5.9, a clear improvement in efficiency for the optimized geometry compared to the baseline is observed. However, it is also evident that the optimized rotor approaches the choke point more quickly. This behavior highlights the trade-off between improved flow handling and the proximity to the system's performance limits under higher mass flow rates.

From Figure 5.10, we observe that the total pressure follows a similar trend for both the baseline and optimized geometries, with the optimized geometry showing slightly higher total pressure values at each operating point. While the improvement may

appear modest when comparing the vertical height of the operating points, it becomes more significant when accounting for the additional mass flow handled by the optimized geometry.

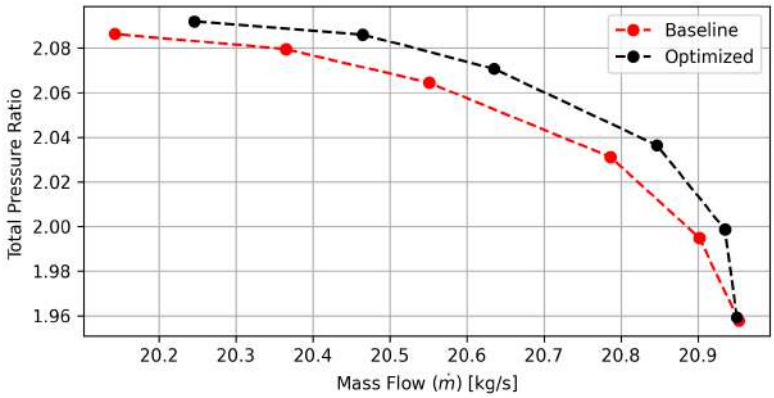

Figure 5.10: Comparison of total pressure ratio across operating points for the baseline and optimized geometries.

In Figure 5.11, an analysis reveals that the optimized geometry results in a slightly higher total temperature ratio compared to the baseline. This outcome is expected, as an increase in total pressure inherently leads to a rise in total temperature due to thermodynamic principles. However, the key aspect to evaluate is how effectively this pressure increase translates into useful work, which is captured by the isentropic efficiency. The previously discussed improvement in isentropic efficiency highlights that the optimized geometry achieves this conversion more effectively, ensuring that the rise in total temperature corresponds to a meaningful performance gain rather than merely an energy loss.

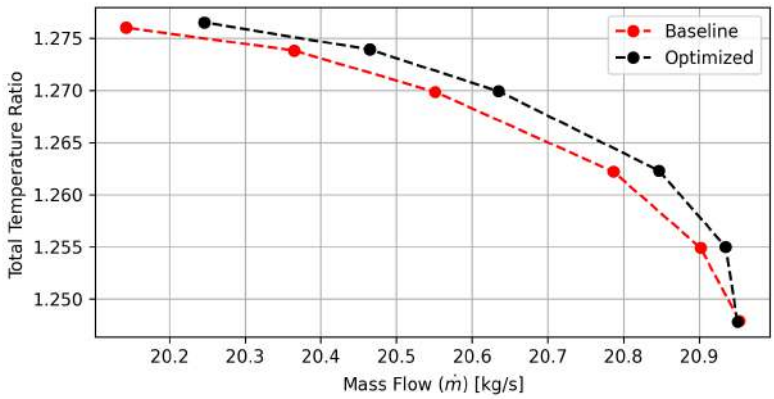

Figure 5.11: Comparison of total temperature ratio across operating points for the baseline and optimized geometries.

5.3.2 Comparison of Radial Distributions of Flow Variables at the Exit

In this section, comparison is made between the radial distributions at the exit such as total temperature, total pressure, and isentropic efficiency between the baseline and optimized geometries. By examining these distributions at the exit, particularly at the near-peak isentropic efficiency operating point, we aim to identify the spanwise regions where the most notable differences occur and assess their contribution to the overall performance improvements.

Radial Distribution of Total Pressure

To set the stage for this analysis, the first figure below illustrates the radial distribution of total pressure at the exit, directly comparing the baseline and optimized geometries.

From Figure 5.12, it can be seen that the optimized geometry achieves higher total pressure values starting at approximately 80% span and continuing down to around 40% span. This improvement is particularly pronounced in the middle-to-upper sections of the span, as should be expected, where the flow benefits most from the optimized design. This small increment in total pressure reflects the enhanced performance of the optimized geometry in these critical regions, where the flow turning and aerodynamic loading is most effective.

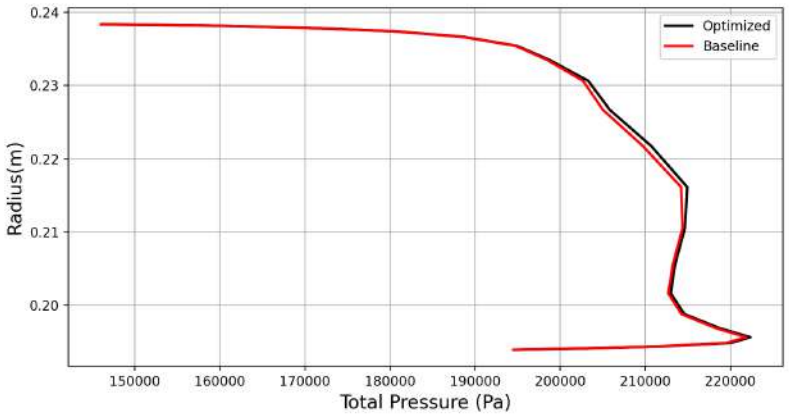

Figure 5.12: Comparison of Radial Distribution of Total Pressure at Exit Plane Between Baseline and Optimized Geometry Near Peak Efficiency Operating Point.

Radial Distribution of Total Temperature

Figure 5.13 depicts the radial distribution of total temperature at the exit, comparing the baseline and optimized geometries. Interestingly, in the span range of approxi-

mately 60% to 80%, the total temperature in the optimized geometry is slightly lower than the baseline. However, beyond the 80% span, we observe a noticeable increase in the optimized case.

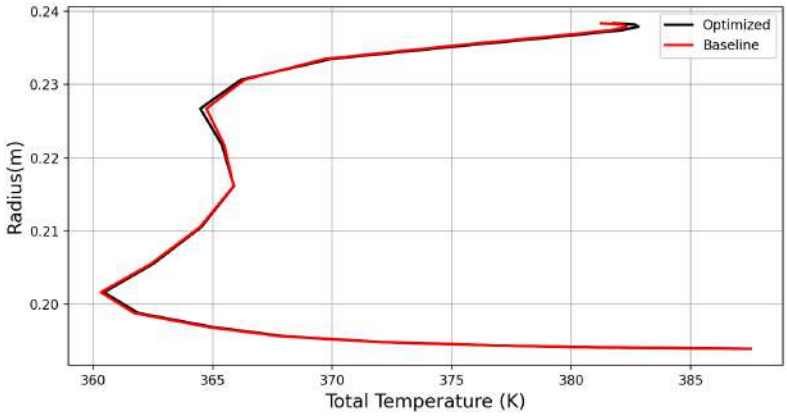

Figure 5.13: Comparison of Radial Distribution of Total Temperature at Exit Plane Between Baseline and Optimized Geometry Near Peak Efficiency Operating Point.

This trend aligns with the theory that while the middle section of the span benefits significantly from the optimized design, achieving a boost in performance, the upper section experiences increased losses. Despite this, the lower mass flow passing through the top section of the span results in overall positive performance improvements, consistent with the enhanced isentropic efficiency and total pressure observed earlier.

Radial Distribution of Axial Velocity

In the axial velocity distribution (Figure 5.14), the optimized geometry shows a noticeable boost in the mid-to-top span (50% to 80%). This region typically experiences significant losses due to tip leakage and generally has lower axial velocity compared to other sections. By increasing the axial velocity in this region, the optimized design not only enhances mass flow through the mid-to-top span but also contributes to a more uniform axial velocity profile across the exit. This improvement in uniformity is a positive outcome, as it can help stabilize flow and improve downstream performance.

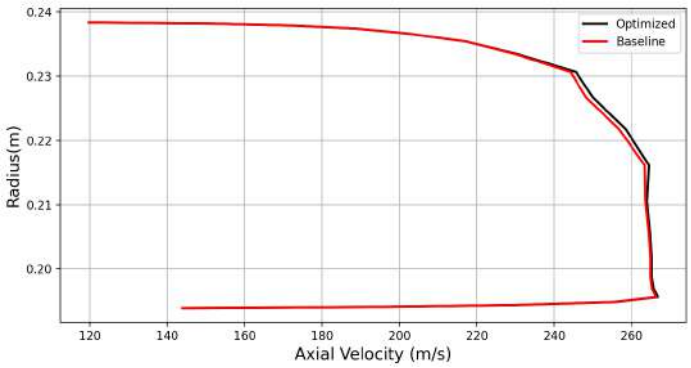

Figure 5.14: Comparison of Radial Distribution of Axial Velocity at Exit Plane Between Baseline and Optimized Geometry Near Peak Efficiency Operating Point.

Radial Distribution of the Spalart-Allmaras Turbulent Variable ($\tilde{\nu}$)

To better understand the behavior of turbulence in the optimized geometry compared to the baseline, we examine the radial distribution of the Spalart-Allmaras turbulent variable ($\tilde{\nu}$) at the exit. This parameter provides insight into the modeled eddy viscosity and its distribution across different spanwise sections of the flow.

By analyzing the distribution of $\tilde{\nu}$ (Figure 5.15), we can identify how the optimization influences the generation and dissipation of turbulence across the span, particularly in regions prone to losses, such as the mid-to-top span where tip leakage effects dominate. This comparison also helps assess how well the optimization balances turbulence levels across the exit plane, ultimately contributing to overall performance improvements.

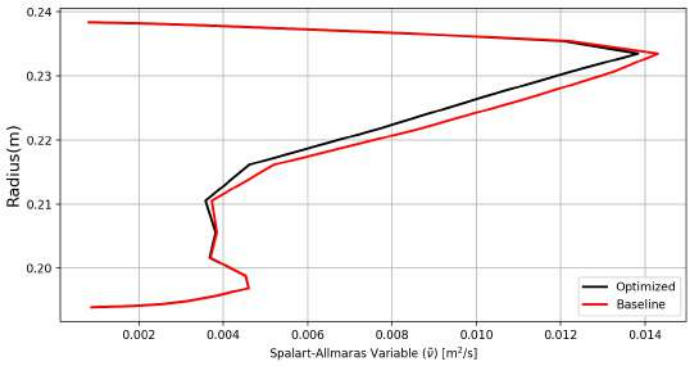

Figure 5.15: Comparison of Radial Distribution of the Spalart-Allmaras Variable ($\tilde{\nu}$) at Exit Plane Between Baseline and Optimized Geometry Near Peak Efficiency Operating Point.

Interestingly, the optimized geometry shows lower turbulence levels from approxi-

mately 90% to 40% span, with the most significant difference observed in the 60-80% span range. This suggests that in the optimized case, there is less turbulence in the lower radial regions compared to the baseline, potentially indicating smoother flow behavior in these sections. Near the blade's trailing edge, the fluid likely experiences fewer losses, as the high-pressure side mixes with the suction side in this critical region. This could result in more efficient flow with less energy dissipation, as seen in the exit distribution of the Spalart-Allmaras Variable ($\tilde{\nu}$).

Summary of Operating Line and Exit Distributions for Optimized Geometry

In this analysis, we compared the performance of the **optimized rotor geometry** with the **baseline geometry** by examining the operating line and key exit distributions (total pressure, total temperature, axial velocity, and turbulent eddy viscosity):

- The optimized geometry shows a shift in the operating line towards higher mass flow rates, achieving better isentropic efficiency and total pressure. However, it reaches the choking point faster than the baseline case. This suggests that the optimized design can handle higher mass flows but operates closer to its limits, particularly in higher flow conditions.
- The optimized geometry exhibits improved total pressure in the mid-to-high span regions, with a significant boost observed around the 80% span. However, the total temperature distribution shows a slight deficit in the **optimized geometry** beyond the 80% span, consistent with the theory that while the middle section is enhanced, the top experiences more losses.
- The optimized geometry shows a more uniform axial velocity distribution, with an increase in axial velocity from 50% to 80% span, particularly benefiting the middle section. This adjustment results in more balanced flow characteristics and reduced losses, especially near the blade's trailing edge, where less mixing occurs between the high-pressure and suction sides of the flow.
- The Spalart-Allmaras Variable ($\tilde{\nu}$) distribution in the optimized geometry shows reduced turbulence from 90% to 40% span, with the most significant difference observed between the 60% to 80% span. This aligns with expectations of smoother flow behavior and fewer losses, particularly near the trailing edge where the high-pressure and suction sides interact.

5.3.3 Comparison of Internal Flow Characteristics: Optimized vs. Baseline Geometry

In this section, we examine the internal flow characteristics of the baseline and optimized rotor geometry to understand the differences in their flow behavior. The analysis will focus on comparing key flow variables such as velocity components, turbulence, and pressure distributions, providing insights into the impact of geometry optimization on the overall flow performance.

The results from PUMA can be utilized in two distinct yet complementary ways, offering different perspectives on the analysis. The first option is to print the radial distribution of the selected flow quantities at a specific axial location (z), providing a snapshot of how the variable varies along the radius at that slice. Alternatively, the results can be printed for a specific radial position (r) along the axial direction (z), allowing the observation of how the variable evolves axially at that fixed radial location. This approach provides insight into the flow's development along the rotor's length at a chosen radial slice. These two methods-examining the radial distribution at specific z-slices and observing the evolution at specific radial positions-offer complementary perspectives on the flow behavior.

Figure 4.1 shows the lines along the z-axis, highlighting the hyperbolic tangent distribution, which results in a denser concentration of radial zones near the endwall of the rotor, allowing for finer resolution in these critical regions. This figure illustrates the meridian profile, providing a clear visualization of how the radial zones are distributed along the rotor and how the flow characteristics will be analyzed across these zones. The specific positions such as -80% chord length, -40% chord length, and -10% chord length are points along the optimized curve, representing its start, the middle section, and a location near its end, respectively.

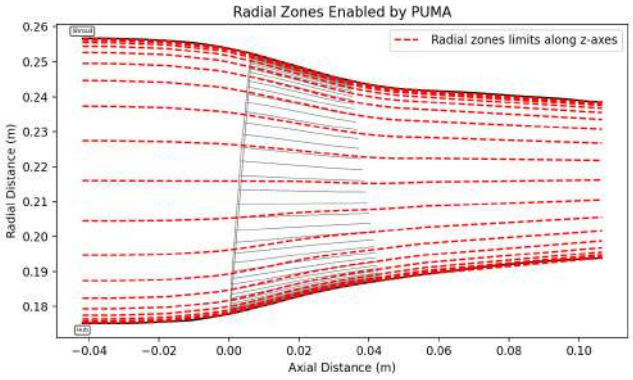

Figure 5.16: Radial zones along the meridional plane of Rotor 37.

Radial Distributions of Velocity Components

The analysis begins, with the components of velocity across various z-locations to evaluate whether the expected changes occur. Specifically, since the optimization is focused on the shroud, modifications in the velocity profile, particularly an increase in the magnitude of radial velocity relative to axial velocity due to the implemented curve in the shroud are anticipated, while generally reducing the overall velocity magnitude.

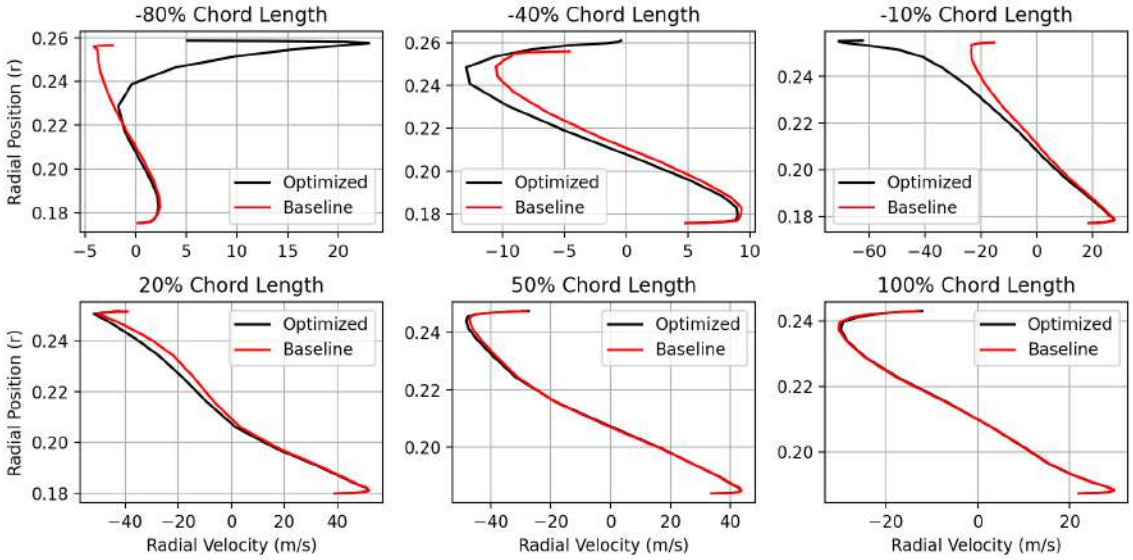

Figure 5.17: Radial distribution of Radial Velocity at different z-locations.

Figure 5.17 presents the radial velocity distribution at different z-locations, revealing key trends. Initially, an outward radial displacement corresponding to the first part of the curve in the shroud is observed. Following this, a negative radial movement appears for the second part of the curve, as expected. Interestingly, this negative radial movement stretches down to approximately 30% of the hub, where the magnitude of positive radial movement is comparatively smaller. This difference in radial velocity stabilizes with the baseline geometry at approximately 60% of the chord length, beginning around the 20% chord length mark

Figure 5.18 examines the axial velocity distribution, highlighting differences between the baseline and optimized geometries. Up to 0% chord length, a deficit in axial velocity is observed in the optimized case, which is expected due to the flow turning more radially as a result of the contoured shape. The region from 0% to 20% chord length appears to act as a transition zone, where the axial velocity begins to recover. Beyond 20% chord length, the optimized geometry shows an advantage over the baseline, particularly in the 60`80% spanwise region, where the radial velocity

difference stabilizes. From this point onward, the optimized geometry achieves a more favorable axial flow in the span of 60`80%. However, in the upper region above 90% span, a very slight deficit in axial velocity is observed from 50% chord length onward, suggesting a localized area of increased losses or weaker flow acceleration.

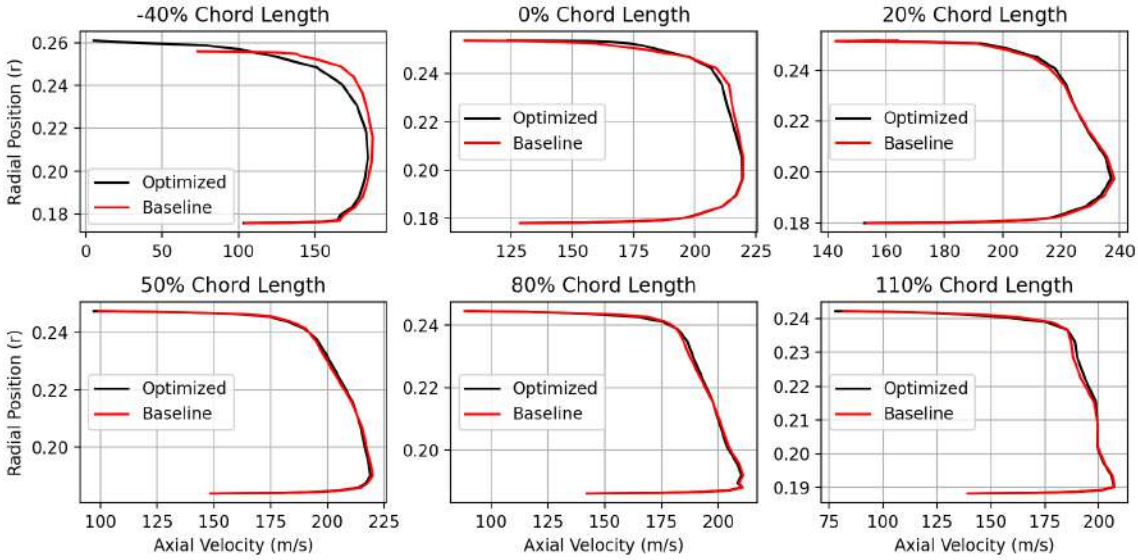

Figure 5.18: Radial distribution of Axial Velocity at different z-locations.

These results demonstrate that the shroud curve impacts the flow by enhancing radial redirection in the first part of the passage and slowing it down in the second, as evidenced by the radial velocity trends. Simultaneously, the optimized geometry shows an initial deficit in axial velocity but gains an advantage in the mid-span region as the flow progresses, indicating a more balanced redistribution of momentum. This combined behavior of radial and axial velocity suggests that the optimization contributes to smoother flow dynamics, especially in the middle region, and potentially improved performance across the rotor.

Radial Distributions of Fluid Properties

By inspecting static pressure distributions(Figure 5.19), starting at the midsection of the contoured shroud curve, a noticeable increase in static pressure is observed across the entire span. This increase is expected due to the deceleration of the fluid as it interacts with the optimized shroud geometry. Moving to the 0% chord location, the static pressure stabilizes at the lower span, with a notable change occurring between the 0-20% span. Here, the static pressure transitions from an advantage to a deficit in the upper span. This shift suggests that, in this region, the radial movement of the flow starts to mix with axial movement, leading to the flow accelerating and behaving more similarly to the baseline geometry. At 20% chord, a static pressure

advantage over the baseline that starts from the hub span is observed. As we move towards the 50% span, the static pressure deficit in the upper span begins to stabilize. From this point onward, the static pressure increases, with the advantage remaining predominantly in the 50-80% spanwise region. This suggests that the optimized geometry continues to provide a performance boost in the middle span, while the flow becomes more uniform across the rotor.

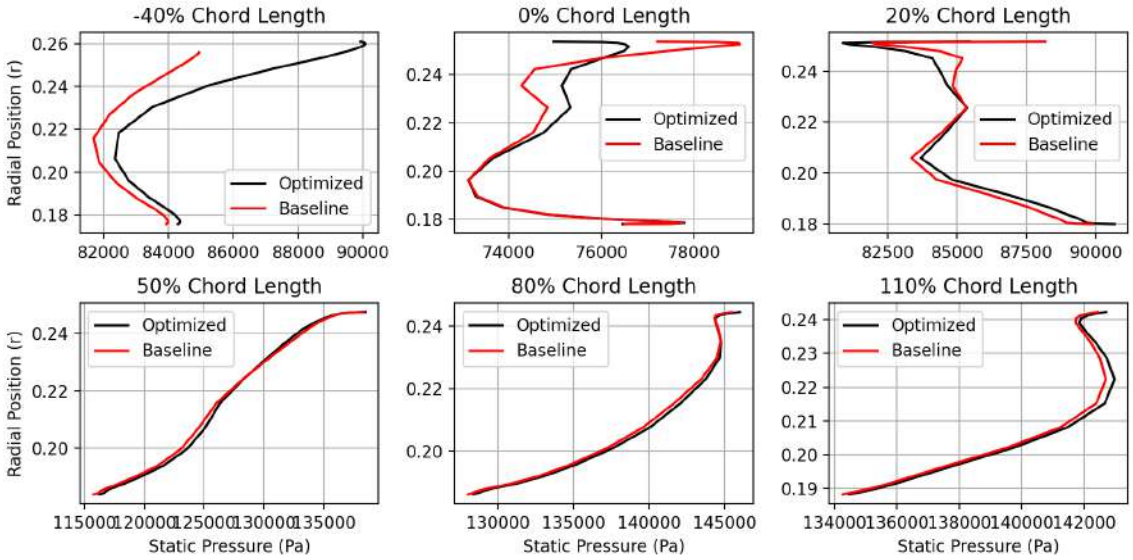

Figure 5.19: Radial distribution of Static Pressure at different z-locations.

Following the static pressure distribution, the total pressure distribution (Figure 5.20)is examined to highlight its behavior across the blade passage. At the 0% axial chord length position, the total pressure shows an advantage over the baseline, while at 20%, it begins to be so close to the baseline. This suggests that, despite the drop in static pressure, the increase in velocity within the optimized geometry contributes to the rise in total pressure. After the 20% chord region, the total pressure starts to gain a slight advantage again. Interestingly, this advantage first emerges around the 30% span, but it becomes more stabilized between the 60-80% spanwise region, where it consistently outperforms the baseline.

Additionally, for the level of turbulence, we examine the Spalart-Allmaras viscosity-like variable($\tilde{\nu}$), which provides insight into the turbulence model's behavior and complements the analysis of flow properties across the rotor (Figure 5.21).

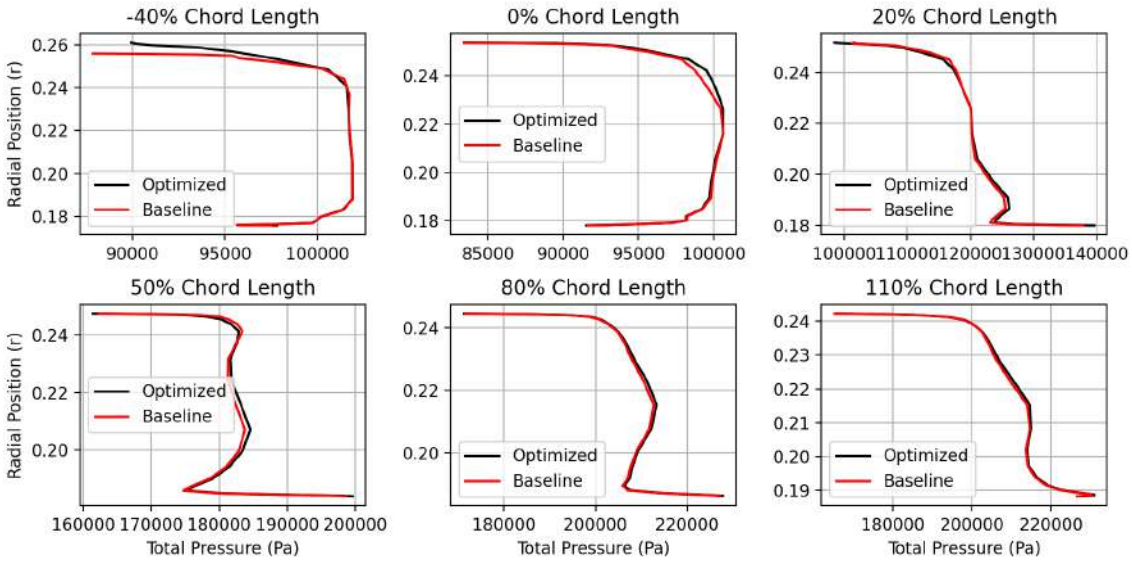

Figure 5.20: Radial distribution of Total Pressure at different z-locations.

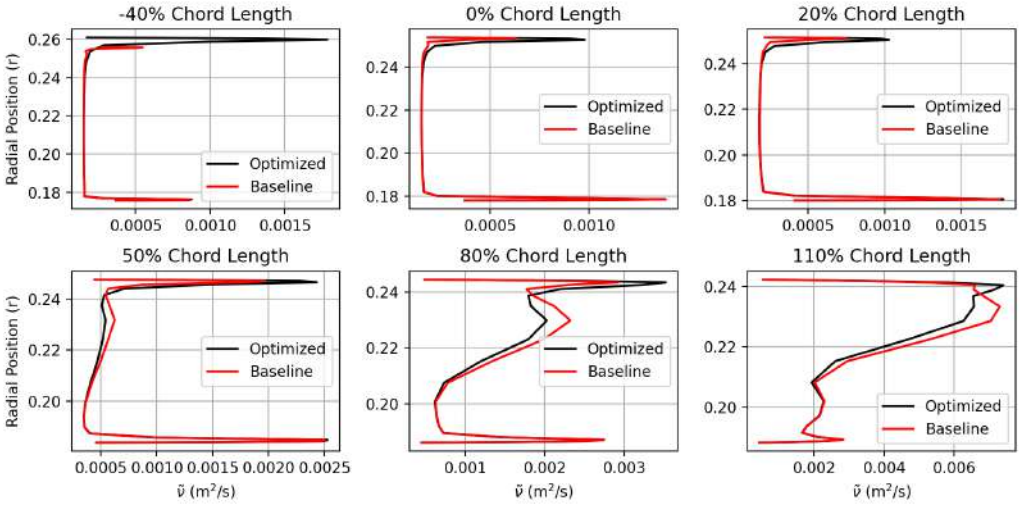

Figure 5.21: Radial distribution of Spalart-Allmaras viscosity-like variable($\tilde{\nu}$) at different z-locations.

Through the inspection of the radial distribution of the Spalart-Allmaras turbulence variable ($\tilde{\nu}$), we observe that the optimized geometry exhibits lower turbulence levels in the 60-90% spanwise region, with this reduction becoming evident from the axial position at 50% chord length and continuing through the downstream area of the blade. Then, its spanwise distributions are examined; these more clearly highlight the 90% span region where the optimized geometry transitions from a deficit to an advantage compared to the baseline.

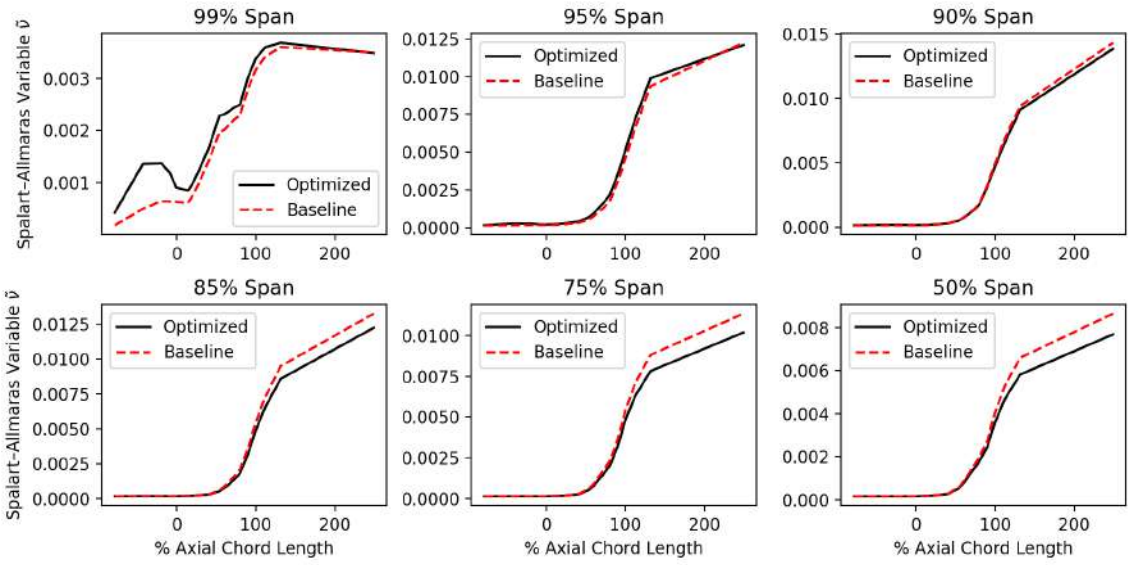

Figure 5.22: Spanwise distribution of Spalart-Allmaras viscosity-like variable($\tilde{\nu}$) at different blade spans.

It should be noted that the optimized geometry exhibits reduced turbulence increase at the trailing edge, where mixing effects occur. This suggests that the 50-80% spanwise region is handled more effectively in the optimized case, contributing to a smoother flow transition and potentially lower losses.

Key Findings

First, by the examination of the velocity components, it becomes evident that the optimized geometry directs more fluid toward the middle section while decelerating it, roughly in the 60-80% spanwise region. This redistribution of flow results in a boost in pressure at the 0% axial chord position, in particular the middle span, where the fluid interaction with the blade leads to favorable conditions. From the (0-20)% axial chord region, static pressure is converted into axial velocity, which marks the phase where the radial velocity approaches to baseline conditions. This mixing area around the 60-80% span exhibits the transition. As a result, starting from the 20% chord length onward, the 60-80% spanwise section begins to show a slight improvement in total pressure. By 80%, static pressure is regained, and beyond this point, the 60-80% span remains slightly better overall.

Turbulence in this section is reduced, as "more fluid" passes through the middle region where losses are inherently lower. However, at the 90% span region, additional losses become evident. At this span, we observe a transition phase where the flow moves from a deficit state toward the shroud, leading to higher turbulence levels. This could arise from the interaction of the less dense fluid near the shroud tip or

from interactions with the boosted layer of flow created below. This transition adds complexity to the flow behavior in this region, highlighting the interplay between local fluid dynamics and the influence of geometry. The optimized geometry demonstrated improved capability in handling the trailing edge region at the upper span (50-90%), exhibiting lower turbulence levels. However, above 90% span, it showed slightly increased losses in the trailing edge region.

Reverse Contour Analysis: Inward Geometry

At this point, the inward contour (reverse) configuration in the same region as the optimized case (shroud-upstream) will also be plotted to explore its behavior and understand why it performs significantly worse compared to the other cases. The decision to examine this particular scenario comes from first, the outcome of the parametric study, where this configuration was distinctly worse, showing up to a 10% reduction in isentropic efficiency, which suggests the possibility of an inverse flow or significant disruption in the fluid behavior. Second, because its a part of the best region outcome which is shroud's upstream region and there should be some relation. Through the analysis of the flow characteristics, The goal is to identify the reasons behind the pronounced degradation in performance for this case while comparing it with the optimized geometry.

The analysis begins with the effects on radial velocity induced by the reversed geometry (Figure 5.23). Initially, we observe that the change in radial velocity follows a similar trend to the optimized configuration, converting axial velocity to radial. However, this conversion is significantly more pronounced in the reversed case, accelerating up to the 80% span. From 80% to 90% span, a distinct layer forms where velocity gradients emerge, where above 90% span, the radial velocity decreases in magnitude, transitioning from high negative values to small positive values very close to the shroud.

Figure 5.24 shows the static pressure distribution at different axial positions. At -40% chord length, we observe a pressure buildup, indicating axial velocity deceleration. During the transition phase from 0% to 20% of the chord length, the pressure does not remain uniform across the z-slice. Instead, it is significantly higher near the shroud and gradually decreases toward lower spans.

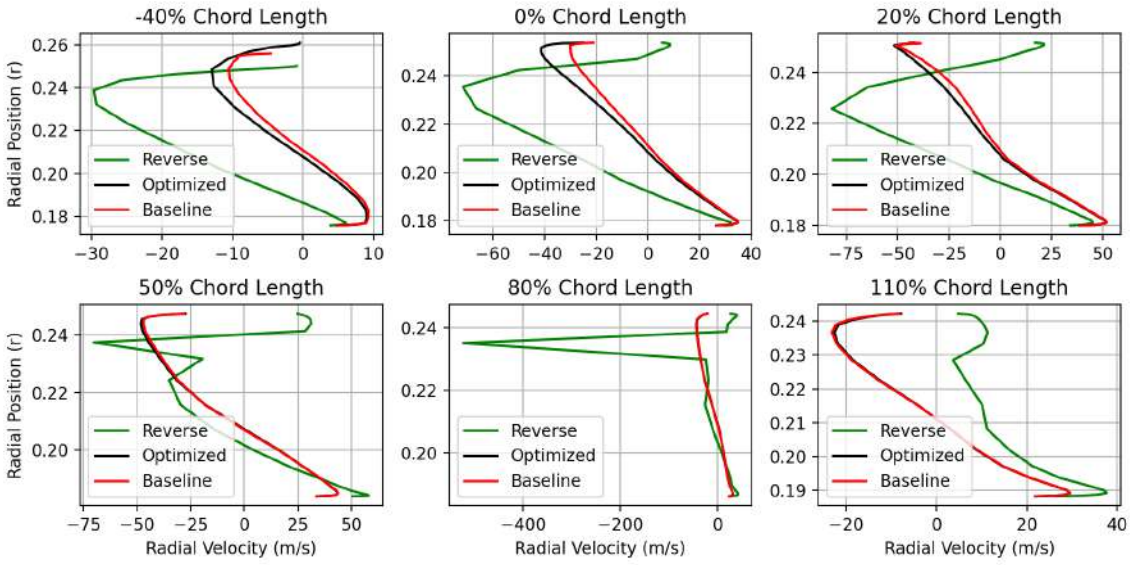

Figure 5.23: Radial distribution of Radial Velocity at different z-locations.

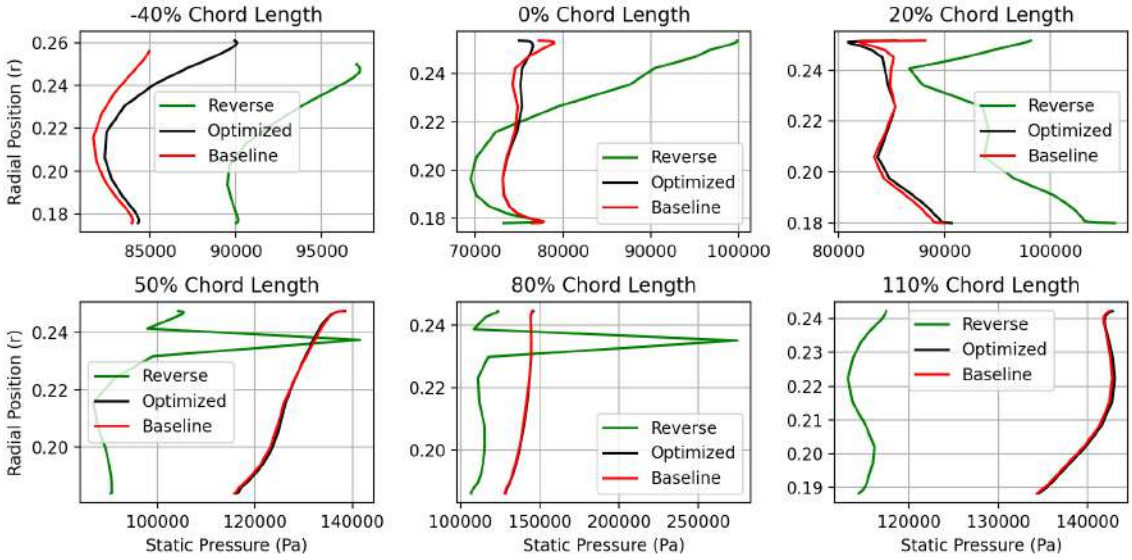

Figure 5.24: Radial distribution of Static Pressure at different z-locations.

Following this, it is observed that the axial velocity (Figure 5.25), which indicates inverse flow near the high shroud regions, where the radial velocity shows a complete reversal. This strongly degenerated flow structure likely arises from adverse pressure gradients and boundary layer effects. Notably, these issues develop very early, as the contrast between the high-pressure region (90% span and above) and the low-pressure region (below 90%) becomes evident even before the blade.

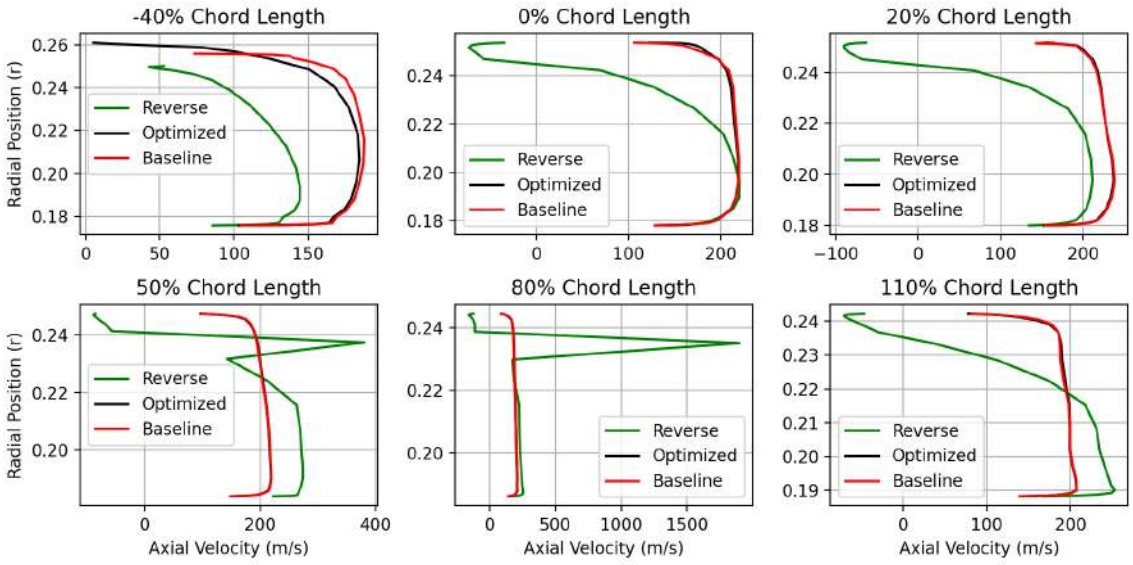

Figure 5.25: Radial distribution of Axial Velocity at different z-locations.

Comparing these results with the optimized configuration, a common pattern where significant changes occur around the 90% span is observed. Additionally, the 60-80% span region emerges as the most affected area in both cases. Also, while the reversed geometry still induced radial velocity relative to axial velocity, its magnitude was greater than in the optimized case. As a result, at the 90% span, the fluid appears to split. Above this point, the flow experiences reverse movement, leading to pressure buildup and ultimately disrupting the overall flow organization.

Chapter 6

Conclusions

This thesis presents the optimization of rotor hub and shroud geometries in an axial compressor, focusing on computational approaches to enhance performance. Specifically, the study examines NASA's Rotor 37, a well-known transonic axial compressor rotor extensively used as a benchmark for CFD and optimization studies. Using PUMA, a GPU-enabled flow solver, a parametric study was conducted to investigate the effects of implementing arc-shaped contours on the hub and shroud regions, outside the blade passage, on the rotor's aerodynamic performance. Following this, optimization was conducted using evolutionary algorithms, starting with the best candidate from the parametric study, to achieve improved isentropic efficiency and overall aerodynamic performance. The study also included comparison with experimental data to assess the accuracy and reliability of the computational results.

6.1 Main Outcomes

From the parametric study, it was observed that most of the evaluated cases exhibited reduced performance compared to the baseline. However, the shroud geometry upstream, featuring an outward orientation of the arc-shaped contour, stood out as the only configuration delivering positive results. In contrast, the inward-oriented arc-shaped contour in the shroud's upstream region produced the worst performance among all cases.

Building on these findings, the optimization process yielded a 0.37% improvement in isentropic efficiency. While this result may appear modest, the positive impact was consistently observed across all cases evaluated through the optimization process. The optimized curve, defined by the selected design variables, adjusted in a manner that increased the radial velocity relative to the axial velocity, while also smoothing the geometry to ensure a more coherent and efficient flow pattern.

The third aspect of this study focused on investigating the flow behavior and understanding the mechanisms behind the observed results. By examining the flow patterns, it became evident that the optimized geometry, which directed the flow inwards from axial to negative radial movement, coupled with deceleration, played a significant role. At 0% chord, a region of increased pressure developed predominantly around the 60-80% span, while at 90% span, interactions between the denser fluid below and the less dense fluid above became prominent. This interaction contributed to the pressurized region, which yielded slightly positive results in terms of flow performance. However, the top section above 90% span experienced degraded performance due to the interaction with the denser fluid below or the less dense fluid experiencing increased losses from tip leakage and its interaction with the shroud's boundary layer.

On the positive side, the region of higher pressure in the middle span (60-80%) allowed for a denser flow to pass through, enhancing the ability to effectively convert rotational speed into pressure. Additionally, this region experienced slightly higher axial velocity, which resulted in a more uniform axial velocity profile at the outlet, contributing to improved overall flow stability. These findings highlight the critical role of mid-span flow dynamics in influencing the compressor's performance and underscore the importance of addressing adverse effects near the shroud.

Finally, we investigated the flow with the inward orientation in the same region. In this case, the flow accelerated downward, creating a pressured region above 90% and a lower-pressure area below. At the 90% span, the flow exhibited inverse behavior, with significant changes in direction. This inverse flow was characterized by strong negative radial velocities, indicating a reversal of the flow near the shroud. One common trend observed was that the 60-80% span region was the most affected afterward.

6.1.1 Broader Implications

The findings of this study provide insights into rotor design optimization, in compressors. The optimized configurations presented in this work resulted in a slight improvement in isentropic efficiency and total pressure recovery, particularly in a region susceptible to high-viscosity effects and boundary layer separation.

Finally, the flow with the inward orientation in the same region was also investigated. In this case, the flow accelerated downward, creating a pressured region above 90% and a lower-pressure area below. At the 90% span, the flow exhibited inverse behavior, with significant changes in direction. This inverse flow was characterized by strong negative radial velocities, indicating a reversal of the flow near the shroud. One common trend observed was that the 60-80% span region was the most affected afterward.

Future Work

Future work could explore various possibilities, such as placing the contour at different axial positions, particularly where the blades begin, or investigating the impact of varying the height. In this study, the results seemed to converge towards a value that was less than the maximum possible, yet a slightly altered and more controlled contour shape could yield significant performance improvements. Furthermore, excluding practical space limitations, increasing the height of the contour could potentially lead to even more pronounced effects. By adjusting these parameters and exploring new geometries, one could unlock additional performance gains and improve the overall efficiency of the rotor.

In conclusion, this study demonstrates the potential of optimizing rotor geometries to enhance turbomachinery performance, with promising avenues for future research and application in practical designs.

Bibliography

[1] A. A. Ameri. *NASA Rotor 37 CFD Code Validation: Glenn-HT Code*. Tech. rep. NASA/CR—2010-216235. AIAA–2009–1060. The Ohio State University, 2010.

[2] J. Bert. "Application of a Design Optimization Strategy to Multi-Stage Compressor Matching". Master of Science Thesis. Cambridge, MA: Massachusetts Institute of Technology, 2006.

[3] A.A. Chemobrovkin and B. Lakshminarayana. *"Numerical Simulation of Complex Turbomachinery Flows"*. The Pennsylvania State University. July 1999.

[4] William Cousins. "The dynamics of stall and surge behavior in axial-centrifugal compressors". In: (Jan. 1997).

[5] S.L. Dixon and C.A. Hall. *Fluid Mechanics and Thermodynamics of Turbomachinery*. 6th. Oxford, UK: Elsevier Inc., 2010. ISBN: 978-1-85617-793-1. DOI: https://doi.org/10.1016/C2009-0-20205-4.

[6] J. Dunham. *CFD Validation for Propulsion System Components*. Tech. rep. Report 355. Advisory Report. May 1998.

[7] F. Gagliardi and K. Giannakoglou. *RBF-Based Morphing of B-Rep Models for Use in Aerodynamic Shape Optimization*. National Technical University of Athens. 2019.

[8] F. Gao. "Advanced Numerical Simulation of Corner Separation in a Linear Compressor Cascade". PhD thesis. Apr. 2014.

[9] K. Giannakoglou. *EASY, The Evolutionary Algorithm SYstem, v2.0*. Available at http://velos0.ltt.mech.ntua.gr/EASY/. 2008.

[10] K. Giannakoglou. *Viscous Flows in Thermal Turbomachinery (in Greek)*. Athens, Greece: Laboratory of Thermal Turbomachines, NTUA, 1997.

[11] M. Hoeger, P. Cardamone, and L. Fottner. "Influence of Endwall Contouring on the Transonic Flow in a Compressor Blade". In: *Proceedings of the ASME Turbo Expo 2002: Power for Land, Sea, and Air*. ASMEDC, 2002. DOI: 10.1115/GT2002-30440. URL: https://asmedigitalcollection.asme.org/GT/proceedings/GT2002/3610X/759/292167.

[12] S. Ito, M. Furukawa, and K. Yamada. "Approximation of hub leakage flow in a high speed axial flow compressor rotor with adjoint method". In: *Journal of Physics: Conference Series* 2217 (2022), p. 012005. DOI: 10.1088/1742-6596/2217/1/012005.

[13] I. A. Johnson and R. O. Bullock. *Aerodynamic Design of Axial-Flow Compressors*. Tech. rep. NASA-SP-36. Acquisition Source: Glenn Research Center. NASA, Jan. 1965.

[14] M. Karakasis and K. Giannakoglou. "On the use of metamodel-assisted, multi-objective evolutionary algorithms". In: *Engineering Optimization* 38.8 (2006), pp. 941–957.

[15] K. Kotsarinis. *NASA Rotor 37 Endwall Profiling Using the GPU-Enabled CFD Solver PUMA*. Diploma Thesis. Athens, 2021.

[16] J. de Laborderie et al. "Wall-Modeled Large-Eddy Simulations of a Multistage High-Pressure Compressor". In: *Flow, Turbulence and Combustion* (2020). DOI: 10.1007/s10494-019-00094-0. URL: https://hal.archives-ouvertes.fr/hal-02571557.

[17] C. B. Meher-Homji. *"The Historical Evolution of Turbomachinery"*. The Pennsylvania State University. 2000.

[18] K. V. Panchal et al. "Effect of Endwall Contouring on a Transonic Turbine Blade Passage: Heat Transfer Performance". In: *Journal of Turbomachinery* 139.1 (2016). ISSN: 0889-504X. DOI: 10.1115/1.4034411.

[19] K. Papailiou, K. Giannakoglou, and K. Mathioudakis. *Introduction to Thermal Turbomachines(in Greek)*. Athens, Greece: Laboratory of Thermal Turbomachines, NTUA, 2000.

[20] A. Peyvan and A. H. Benisi. "Axial-Flow Compressor Performance Prediction in Design and Off-Design Conditions through 1-D and 3-D Modeling and Experimental Study". In: *Journal of Engineering for Gas Turbines and Power* (2021).

[21] X. Qiang, J. Li, and Y. Ma. "Experimental test of a compressor cascade with non-axisymmetric end-wall contouring at off-design conditions". In: *Applied Thermal Engineering* (2024).

[22] L. Reid and R. D. Moore. "Design and overall performance of four highly loaded, high speed inlet stages for an advanced high-pressure-ratio core compressor". In: NASA Technical Paper 1337 (Oct. 1978).

[23] L. Reid and R. D. Moore. "Performance of Single-Stage Axial-Flow Transonic Compressor With Rotor and Stator Aspect Ratios of 1.19 and 1.26, Respectively, and With Design Pressure Ratio of 1.82". In: NASA Technical Paper 1338 (Nov. 1978).

[24] O. Reutter et al. “Advanced Endwall Contouring for Loss Reduction and Outflow Homogenization for an Optimized Compressor Cascade”. In: *International Journal of Turbomachinery Propulsion and Power* (2017).

[25] M. Rose and N. Harvey. “Turbomachinery Wakes: Differential Work and Mixing Losses”. In: *Journal of Turbomachinery-transactions of The Asme - J TURBOMACH-T ASME* 122 (Jan. 2000). DOI: 10.1115/1.555429.

[26] I. Sadrehaghighi. *Turbomachinery of Gas Turbines in CFD*. CFD Open Series. Jan. 2023.

[27] S. Shahpar, P. Seshadri, and G. T. Parks. “Leakage Uncertainties in Compressors: The Case of Rotor 37”. In: *Journal of Propulsion and Power* 31.1 (2014), pp. 141–151. DOI: 10.2514/1.B35039.

[28] P. R. Spalart and S. R. Allmaras. “A one-equation turbulence model for aerodynamic flows”. In: *AIAA Journal* 30.11 (1992), pp. 2745–2751. DOI: 10.2514/6.1992-439.

[29] K. L. Suder. “Experimental Investigation of the Flow Field in a Transonic,Axial Flow Compressor With Respect to the Development of Blockage and Loss”. In: NASA Technical Memorandum 107310 (Oct. 1996).

[30] K. L. Suder and M. L. Celestina. *Experimental and Computational Investigation of the Tip Clearance Flow in a Transonic Axial Compressor Rotor*. Tech. rep. NASA TM 106711. NASA, 1995.

[31] X. Trompoukis. “Numerical solution of aerodynamic-aeroelastic problems on Graphics Processing Units (in Greek).” PhD thesis. National Technical University of Athens, 2012.

[32] K. T. Tsiakas. “Development of Shape Parameterization Techniques,a Flow Solver and its Adjoint, for Optimization on GPUs.Turbomachinery and external aerodynamics applications"”. PhD thesis. National Technical University of Athens (NTUA), Oct. 2019.

[33] Z. Wei et al. “Tip-leakage flow loss reduction in a two-stage turbine using axisymmetric-casing contouring”. In: *Chinese Journal of Aeronautics* 27.5 (2014), pp. 1111–1121. ISSN: 1000-9361. DOI: https://doi.org/10.1016/j.cja.2014.08.009. URL: https://www.sciencedirect.com/science/article/pii/S1000936114001290.

[34] G. Zambonini. “Unsteady dynamics of corner separation in a linear compressor cascade”. PhD thesis. Dec. 2016.

Εθνικό Μετσόβιο Πολυτεχνείο
Σχολή Μηχανολόγων Μηχανικών
Εργαστήριο Θερμικών Στροβιλομηχανών
Μονάδα Παράλληλης Υπολογιστικής Ρευστοδυναμικής
& Βελτιστοποίησης

Διερεύνηση-βελτιστοποίηση της επίδρασης διαμορφώσεων στα κελύφη κινητής πτερύγωσης διηχητικού συμπιεστή

Διπλωματική Εργασία

Μπουζαλάς Κωνσταντίνος

Επιβλέπων: Κυριάκος Χ. Γιαννάκογλου, Καθηγητής ΕΜΠ

Αθήνα, 2025

Εκτενής Περίληψη στα Ελληνικά

Εισαγωγή

Η διπλωματική εργασία επικεντρώνεται στην ανάλυση και βελτιστοποίηση της απόδοσης της κινητής πτερύγωσης NASA Rotor 37.Αυτή, μαζί με την σταθερή πτερύγωση (Stator 37), σχεδιάστηκαν με γεωμετρία χαμηλού λόγου επιμήκους, ως η πρώτη βαθμίδα οκταβάθμιου διηχητικού συμπιεστή με λόγο πίεσης 20:1. Στόχος είναι η αξιολόγηση παραμέτρων όπως ο ισεντροπικός βαθμός απόδοσης και ο λόγος πίεσης, διαμορφώνοντας αξονοσυμμετρικά τη γεωμετρία των επί ποδός και κεφαλής κελυφών.Η κινητή πτερύγωση αυτή είναι ευρέως διαδεδομένη στο χώρο των θερρμικών στροβιλομηχανών, διαθέτοντας πλήθος πειραματικών δεδομένων που την καθιστούν σημαντικό εργαλείο στην αξιολόγηση και σύγκριση υπολογιστικών προσομοιώσεων της ροής (CFD).

Ο επιλύτης του πεδιού ροής που χρησιμοποιήθηκε στη μελέτη αυτή είναι ο PUMA (Parallel Unstructured Multi-row Adjoint) ο οποίος αναπτύχθηκε στο Εργαστήριο Θερμικών Στροβιλομηχανών του ΕΜΠ. Για τη βελτιστοποίηση που πραγματοποιήθηκε με εξελικτικό αλγόριθμο και έχει ως στόχο τη μεγιστοποίηση του ισεντροπικού βαθμού απόδοσης της ροής, χρησιμοποιήθηκε το λογισμικό EASY (Evolutionary Algorithms

SYstem). Για την επιβεβαίωση των αποτελεσμάτων του PUMA, πραγματοποιήθηκε σύγκριση τους με τα διαθέσιμα πειραματικά δεδομένα.

Στη διπλωματική αυτή εργασία, η διαμόρφωση της γεωμετρίας των επιφανειών του κελύφους πραγματοποιείται σε περιοχές ανάντι και κατάντι του πτερυγίων. Ως πρώτο βήμα, διεξάγεται παραμετρική μελέτη για τον εντοπισμό της καλύτερης περιοχής όσον αφορά τον ισεντροπικό βαθμό απόδοσης, προκειμένου να ακολουθήσει βελτιστοποίηση. Το δεύτερο βήμα αφορά τη βελτιστοποίηση της γεωμετρίας, καθώς και τη μελέτη της απόκρισης των μεταβλητών σχεδιασμού που τη διαμορφώνουν. Το τελικό στάδιο της διπλωματικής εργασίας είναι η μελέτη και σύγκριση του πεδίου ροής της βέλτιστης με την αρχική γεωμετρία, με σκοπό την εύρεση των φυσικών αιτίων που προκάλεσαν τις θετικές μεταβολές στην απόδοση της ροής.

Διαμόρφωση Γεωμετρίας Κελύφους

Το υπολογιστικό πλέγμα που χρησιμοποιήθηκε για τη διακριτοποίηση του πεδιού ροής της κινητής πτερύγωσης NASA Rotor 37, είναι μη δομημένο, με εξάεδρα στοιχεία και αποτελείται περίπου από 3.200.000 κόμβους. Το πλέγμα είναι ιδιαίτερα πυκνό στις κρίσιμες περιοχές όπως η ακμή προσφυγής/προσβολής του πτερυγίου ή στα τοιχώματα των κελυφών.

Στην παρούσα μελέτη εφαρμόστηκε καμπυλοειδής διαμόρφωση αξονοσυμμετρικού τύπου, δίνοντας τη δυνατότητα παραμετροποίησης του προφίλ των κελυφών στο μεσημβρινό επίπεδο. Για την παραμετροποίηση της γεωμετρίας των κελυφών στο μεσημβρινό επίπεδο χρησιμοποιήθηκαν οι παραμετρικές καμπύλες Bèzier, οι οποίες επιλέχθηκαν διότι είναι εύχρηστες και παράγουν ομαλές καμπύλες λόγω της πολυωνυμικής φύσης τους. Στο Σχημα 1 φαίνεται πώς με 6 σημεία ελέγχου υπάρχει επίδραση στο κέλυφος επί ποδός, ανάντι της ροής, καθώς και το αποτέλεσμα της στην επιφάνεια του κελύφους

Σχήμα 1: Παραμετροποίηση κελύφους επί ποδός, ανάντι ροής. Αριστερά, οπτική στο μεσημβρινό επίπεδο, δεξιά, 3D οπτική.

Το τελικό στάδιο είναι να παρεμβληθεί η μετατόπιση των οριακών κόμβων που προκλήθηκε από την παραμετροποίηση, στο εσωτερικό του πλέγματος, και αυτό επιτυγχάνεται με

τη χρήση της μεθόδου RBF(Radial Basis Function. Η μέθοδος RBF είναι κατάλληλη λόγω της ικανότητάς της να παράγει ομαλή και συνεχή παρεμβολή και να χειρίζεται αποτελεσματικά μη δομημένα πλέγματα. Με την μέθοδο αυτή, κάθε εσωτερικός κόμβος εξαρτάται από την απόσταση του από τους οριακούς κόμβους, ενώ η γνωστή μετατόπιση των οριακών κόμβων χρησιμοποιείται για τον υπολογισμό των αντίστοιχων βαρών της παρεμβολής.

Σύγκριση του PUMA με πειραματικά δεδομένα.

Σε αυτό το κεφάλαιο πραγματοποιείται σύγκριση των αποτελεσμάτων του PUMA με τα πειραματικά δεδομένα της NASA. Πιο συγκεκριμένα, γίνεται σύγκριση του ισεντροπικού βαθμού απόδοσης και του λόγου ολικής πίεσης καθώς και η ακτινικές τους κατανομές στην έξοδο για σημείο λειτουργίας κοντά στη μέγιστη απόδοση.

Ο PUMA επιλύει τις εξισώσεις RANS. Το μοντέλο της τύρβης που χρησιμοποιήθηκε είναι το μοντέλο Spalart-Allmaras, που εισάγει μια επιπλέον εξίσωση που υπολογίζει την τυρβώδη συνεκτικότητα. Επιπλέον, για την ακριβή προσομοίωση της ροής κοντά στο τοίχωμα, εφαρμόζεται προσέγγιση χαμηλών αριθμών Reynolds, όπου γίνεται ολοκλήρωση μέχρι πολύ κοντά στον τοίχο.

Για τις οριακές συνθήκες εισόδου του πεδίου ροής επιβάλλονται 4 μεταβλητές και μία για το μοντέλο της τύρβης. Εδώ δίνονται η ολική πίεση, ολική θερμοκρασία και δύο γωνίες εισόδου. Ο αριθμός Mach εξάγεται από το πεδίο ροής. Για το μοντέλο της τύρβης δίνεται ο λόγος τυρβώδης προς τη μοριακή συνεκτικότητα.

Λόγω τη υποηχητικής ροής στην έξοδο, το σύστημα των εξισώσεων για να επιλυθεί χρειάζεται μια γνωστή μεταβλητή και μια για το μοντέλο τύρβης. Εδώ, δίνεται η μέση στατική πίεση στο ακτινικό μέσο της εξόδου, η οποία επιλύωντας την εξίσωση ακτινικής ισορροπίας μετατρέπεται σε ακτινική κατανομή πίεσης στην έξοδο. Για το μοντέλο τύρβης επιβάλλεται η μηδενική συνθήκη Neumann. Η ολική θερμοκρασία, ο αριθμός Mach, και 2 γωνίες ροής στην έξοδο, εξάγονται από το πεδίο ροής.

Για τις πλευρικές οριακές συνθήκες, εφαρμόζεται περιφερειακή περιοδικότητα, η οποία απαιτεί τα σημεία που ισαπέχουν κατά το περιφερειακό βήμα της πτερύγωσης και η προβολή τους στο άξονα περιστροφής να έχουν ίσες βαθμωτές ποσότητες, ενώ οι διανυσματικές ποσότητες υφίστανται περιστροφή κατά το βήμα της πτερύγωσης. Τέλος, για τις οριακές συνθήκες τοίχου, επιβάλλεται συνθήκη μη ολίσθησης, που θέλει τη σχετική ταχύτητα πάνω στο τοίχο ίση με μηδέν. Τέλος, ως προς την μετάδοση θερμότητας έχουμε αδιαβατικές συνθήκες στα τοιχώματα.

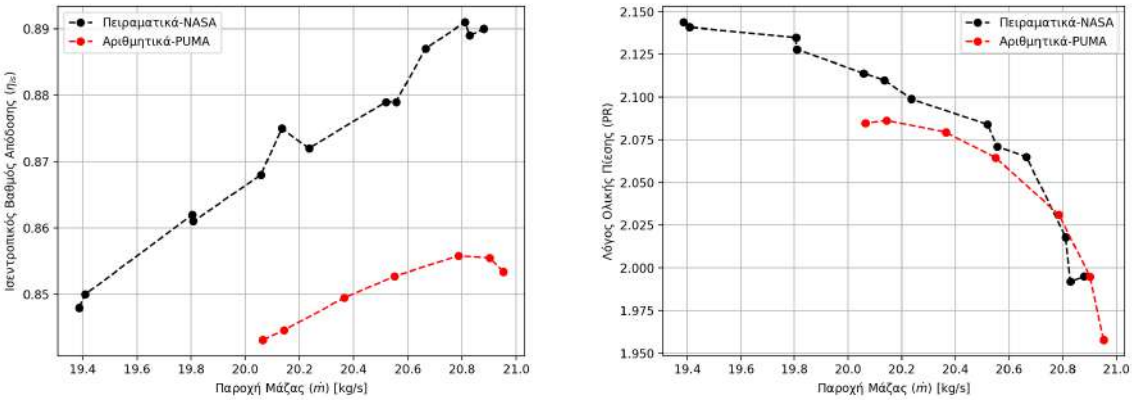

Σχήμα 2: Σύγριση χαρακτηριστικών ισεντροπικού βαθμού απόδσης και λόγου ολικής πίεσης στις ονομαστικές στροφές.

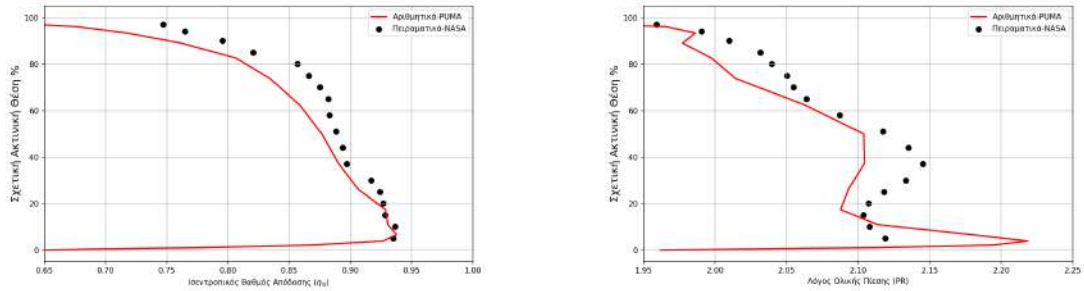

Σχήμα 3: Σύγριση ακτινικών κατανομών στην έξοδο του ισεντροπικού βαθμού απόδοσης και λόγου ολικής πίεσης, κοντά στη μέγιστη απόδοση.

Από το Σχήμα 2 βλέπουμε ότι ο λόγος πίεσης, όσο πλησιάζει προς τα σημεία λειτουργίας μέγιστης παροχής, πλησιάζει περισσότερο τα πειραματικά δεδομένα, ενώ γενικά ο ισεντροπικός βαθμός παρουσιάζει μια διαφορά καθ΄ όλο το εύρος παροχών. Από το Σχήμα 3 βλέπουμε ότι ο ισεντροπικός βαθμός, από τη μέση και κάτω, πλησιάζει τα πειραματικά δεδομένα, ενώ από τη μέση και πάνω υφίσταται μια διαφορά της τάξεως του 3%. Η κατανομή του λόγου πίεσης στο μέρος του κελύφους στο πόδι παρουσιάζει μια αύξηση σε σχέση με τα πειραματικά δεδομένα, κάτι που δικαιολογείται από τη βιβλιογραφία.

Παραμετρική Μελέτη Περιοχών προς Διαμόρφωση.

Σκοπός της παραμετρικής μελέτης είναι να εξετάσει τις υπόψη περιοχές του κελύφους εκτός του περάσματος του δρομέα, εφαρμόζοντας συμμετρικές καμπύλες για τη διαμόρφωση του κελύφους στο μεσημβρινό προφίλ. Όπως φαίνεται στο Σχήμα 4, οι περιοχές

είναι 4, και μαζί με τη φορά της καμπύλης εσωτερικά (inwards) ή εξωτερικά (outwards, έχομε 8 υποπεριπτώσεις, οι οποίες δοκιμάζονται σε 3 διαφορετικά ύψη παραμετρικής καμπύλης. Τα ύψη εκφράζονται σε ποσοστό από το αντίστοιχο ακτινικό ύψος της διατομής εισόδου ή εξόδου ανάλογα αν μιλάμε για περιοχή ανάντι ή κατάντι της ροής αντίστοιχα.

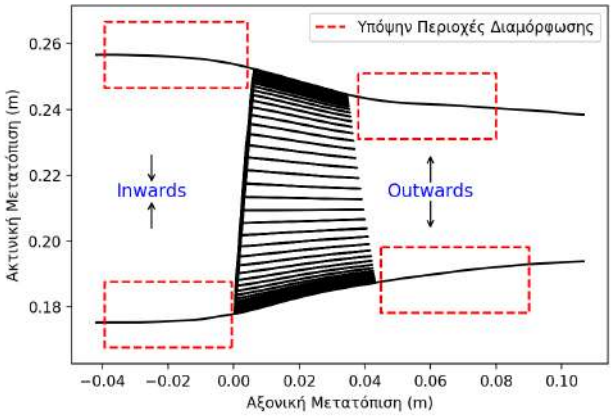

Σχήμα 4: Υπόψην περιοχές προς διαμόρφωση.

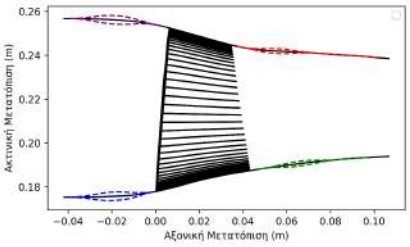

2% Ύψος παραμετροποίησης.

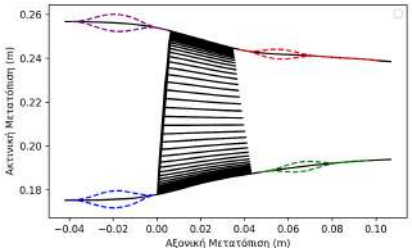

4% Ύψος παραμετροποίησης.

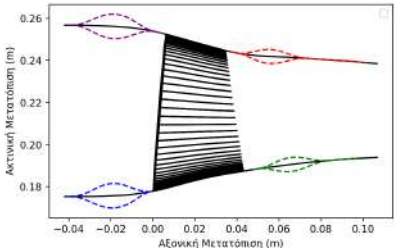

6% Ύψος παραμετροποίησης.

Σχήμα 5: Οπτικοποίηση των υψών παραμετροποίησης αναλογικά με όλο το πεδίο της κινητής πτερύγωσης στο μεσημβρινό επίπεδο.

Στο Σχήμα 5 φαίνονται τα 3 διαφορετικά ύψη που θα εξετασθούν μέσα στο πεδίο ροής για μια οπτικά αναλογική σύγκριση. Τέλος, στο Σχήμα 6 φαίνονται τα αποτελέσματα της παραμετρικής μελέτης, όπου συγκρίνεται η διαφορά του ισεντροπικού βαθμού απόδοσης της καθεμίας περίπτωσης με αυτόν της αρχική γεωμετρίας.

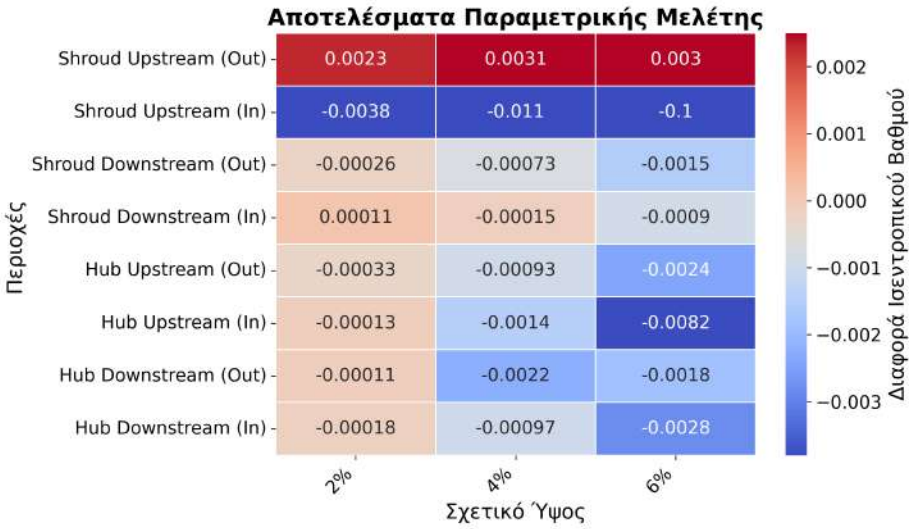

Σχήμα 6: Αποτελέσματα Παραμετρικής μελέτης.

Από το Σχήμα 6, βλέπουμε ότι η περίπτωση του κελύφους της κεφαλής (Shroud), ανάντι της ροής με φορά προς τα έξω, είναι η μόνη με θετικά αποτελέσματα και στα 3 διαφορετικά ύψοι παραμετροποίησης. Ενώ, οι άλλες περιπτώσεις παρουσιάζουν αρνητικά αποτελέσματα αυξανόμενα με το ύψος. Ως αποτέλεσμα της παραμετρικής μελέτης, βελτιστοποιείται η γεωμετρία της περιοχής του **κελύφους κεφαλής ανάντι της ροής** με **εξωτερική φορά** (Outwards).

Βελτιστοποίηση γεωμετρίας κελύφους κεφαλής ανάντι της ροής

Η βελτιστοποίηση υλοποιείται με μια πληθυσμιακή μέθοδο εξελικτικού αλγορίθμου, με τη χρήση του λογισμικού EASY. Πιο συγκεκριμένα, ο εξελικτικός αλγόριθμος είναι τύπου (μ, λ), όπου μ είναι οι γονείς και λ τα παιδιά. Μέσα από διαδοχικές γενιές και εφαρμογή τελεστών, όπως διασταύρωση (crossover) και μετάλλαξη (mutation), επιτυγχάνεται η βέλτιστη λύση για την αντικειμενική συνάρτηση. Ο EASY παρέχει τη δυνατότητα εφαρμογής μεταμοντέλου, το οποίο μετά από ένα προκαθορισμένο αριθμό αξιολογήσεων υπολογίζει προσεγγιστικά την αντικειμενική συνάρτηση και επιταχύνει τη διαδικασία βελτιστοποίησης μειώνοντας το υπολογιστικό κόστος των επιπλέον αξιολογήσεων. Στην εργασία αυτή, χρησιμοποιείται μεταμοντέλο RBF συναρτήσεων.

Η αντικειμενική συνάρτηση έχει ως στόχο τη μεγιστοποίηση του ισεντροπικού βαθμού απόδοσης. Οι συντεταγμένες των σημείων ελέγχου της παραμετροποίησης αποτελούν και τις μεταβλητές σχεδιασμού. Πιο συγκεκριμένα, το πρόβλημα της βελτιστοποίησης χερίζεται 7 μεταβλητές σχεδιασμού, έξι από τις οποίες καθορίζουν τα σημεία ελέγχου Bèzier πάνω στον άξονα z, και μια μεταβλητή σχεδιασμού να καθορίζει το ύψος.

Παράμετρος	**Τιμή**
Μέγιστος αριθμός επιλέκτων ανά γενιά	5
Αριθμός επιλέκτων που εισάγονται ως νέοι απόγονοι	1
Πιθανότητα επιλογής επιλέκτων	0.2
Μέγεθος τουρνουά	5
Πιθανότητα επιτυχίας στο τουρνουά	0.90
Μηχανισμός επιλογής	Διαγωνισμός

Πίνακας 1: Βασικές παράμετροι του μηχανισμού επιλογής για τον εξελικτικό αλγόριθμο.

Παράμετρος	**Τιμή**
Μέγεθος πληθυσμού γονέων (μ)	20
Μέγεθος πληθυσμού παιδιών (λ)	40
Πιθανότητα μετάλλαξης	0.03
Πιθανότητα διασταύρωσης	0.85

Πίνακας 2: Παράμετροι πληθυσμού για τον εξελικτικό αλγόριθμο.

Αποτελέσματα βελτιστοποίησης

Στο Σχήμα 7 παρουσιάζεται η σύγκλιση του ισεντροπικού βαθμού απόδοσης στο σύνολο των αξιολογήσεων που πραγματοποιήθηκαν από τον EASY. Η βελτιστοποίηση οδήγησε σε αύξηση του ισεντροπικού βαθμού απόδοσης κατά 0.37%, φτάνοντας συνολικά στο 85.7%.

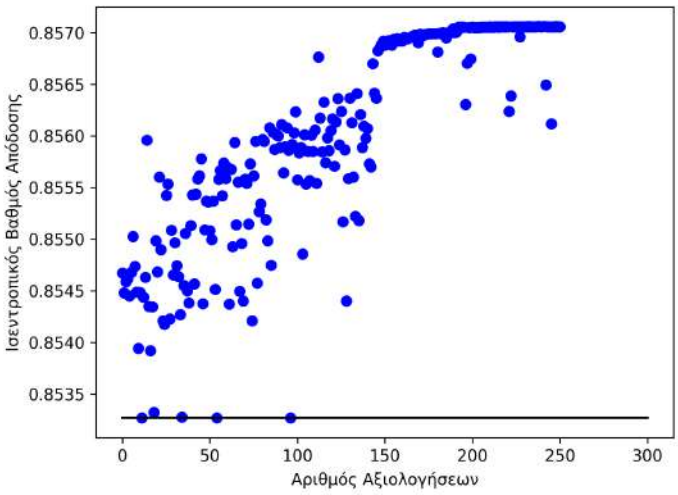

Σχήμα 7: Αποτελέσματα όλων των αξιολογήσεων κατά την βελτιστοποίηση

Παρακάτω στο Σχήμα 7 φαίνεται η γεωμετρία της βέλτιστης παραμετρικής καμπύλης συγκριτικά με τη συμμετρική που χρησιμοποιήθηκε στην παραμετρική μελέτη, με σκοπό την ανάδειξη των διαφορών που οδήγησαν στην αύξηση του ισεντροπικού βαθμού. Βλέπουμε ότι η καμπύλη έχει την τάση να στρίψει προς τα δεξιά, κατευθύνοντας τη ροή σε μια πιο ακτινική διεύθυνση στην έξοδο, σε σύγκριση με την αξονική. Δηλαδή, αναμένουμε ο αέρας να εξέλθει με μεγαλύτερη ακτινική ταχύτητα στην έξοδο.

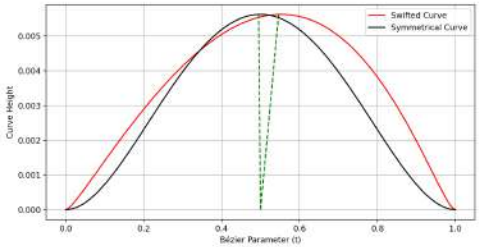

Σχήμα 7: Βέλτιστη καμπύλη Bèzier συγκριτικά με την συμμετρική καμπύλη της παραμετρικής μελέτης.

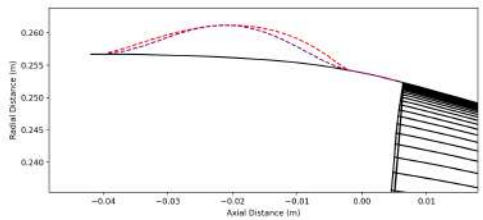

Σχήμα 8: Παραμετροποιημένο προφίλ κελύφους επί κεφαλής, ανάντι της ροής, στο μεσημβρινό επίπεδο.

Σύγκριση Βέλτιστης-Αρχικής Γεωμετρίας

Σε αυτό το κεφάλαιο συγκρίνεται η βέλτιστη γεωμετρία του κελύφους με αυτήν του αρχικού πλέγματος, με σκοπό την διερεύνηση των θετικών επιδράσεων από τις αλλαγές στη γεωμετρία. Η σύγκριση θα γίνει σε 3 διαφορετικά στάδια :

- Σύγκριση χαρακτηριστικών λόγου ολικής πίεσης και ισεντροπικού.

- Σύγκριση ακτινικών κατανομών ολικής πίεσης και ολικής θερμοκρασίας στην έξοδο, κοντά στη μέγιστη απόδοση.
- Σύγκριση κινηματικών και θερμοδυναμικών μεγεθών στο εσωτερικό του πεδίου ροής.

Το πρώτο στάδιο, έχει σκοπό να ερευνήσει τις διαφορές που προκύπτουν σε διαφορετικά σημεία λειτουργίας της κινητής πτερύγωσης μεταβάλωντας την στατική πίεση εξόδου. Στο Σχήμα 9 και Σχήμα 10, παρατηρούμε ότι στη βέλτιση γεωμετρία υπάρχει αύξηση τόσο στον ισεντροπικό βαθμό απόδοσης όσο και στον λόγο ολικής πίεσης, σε όλα τα σημεία λειτουργίας. Παράλληλα, για την ίδια στατική πίεση στην έξοδο, η βέλτιστη γεωμετρία διαχειρίζεται μεγαλύτερη ροή μάζας, γεγονός που οδηγεί στο φαινόμενο του ηχητικού στραγγαλισμού (choking) πιο γρήγορα.

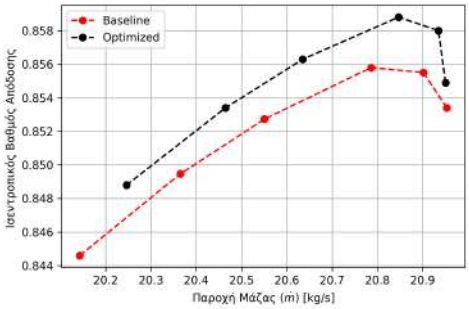

Σχήμα 9: Σύγκριση χαρακτηριστικής Ισεντροπικού βαθμού απόδοσης.

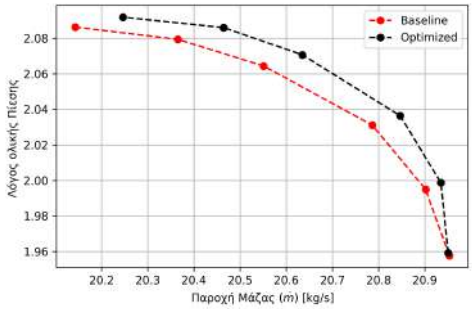

Σχήμα 10: Σύγκριση χαρακτηριστικής Λόγου ολικής πίεσης.

Στο Σχήμα 11 και Σχήμα 12 φαίνονται οι διαφορές των παραμέτρων ολικής πίεσης και ολικής θερμοκρασίας κατά την ακτίνα στην έξοδο. Πιο συγκεκριμένα, διακρίνεται μια μικρή αλλά αισθητή βελτίωση της ολικής πίεσης στο 50-80% του ύψους, καθώς και μια λιγότερο έντονη βελτίωση της ολικής θερμοκρασίας σε μια μικρή περιοχή γύρω στο 80% του ύψους. Ως αποτέλεσμα, η νέα γεωμετρία οδήγησε σε μια μικρή αύξηση του έργου που παρήγαγε ο δρομέας, με μειωμένες απώλειες, σύμφωνα με την κατανομή της ολικής θερμοκρασίας.

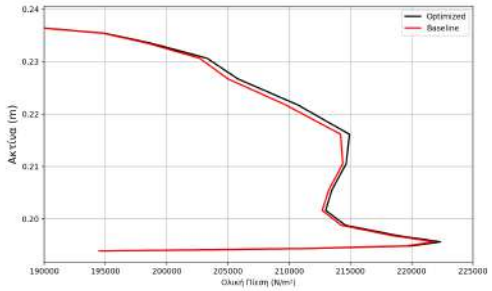

Σχήμα 11: Σύγκριση ακτινικής κατανομής της Ολικής Πίεσης, στην εξόδο.

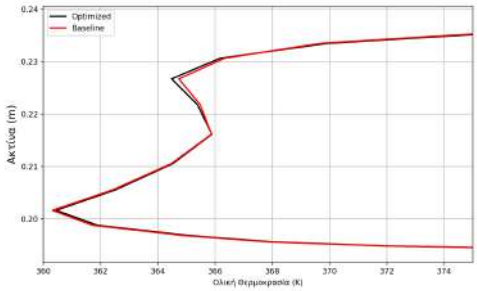

Σχήμα 12: Σύγκριση ακτινικής κατανομής της Ολικής Θερμοκρασίας, στην εξόδο.

Τέλος, ως προς τα χαρακτηριστικά της εσωτερικής ροής, από το σχήμα Σχήμα 13 και Σχήμα 14 παρατηρούμε ότι ο αέρας αποκτά μια ακτινική κατεύθυνση στη περιοχή της παραμετροποιημένης γεωμετρίας. Η αξονική ταχύτητα του αέρα παρουσιάζει επιβράδυνση στην περιοχή αυτή.

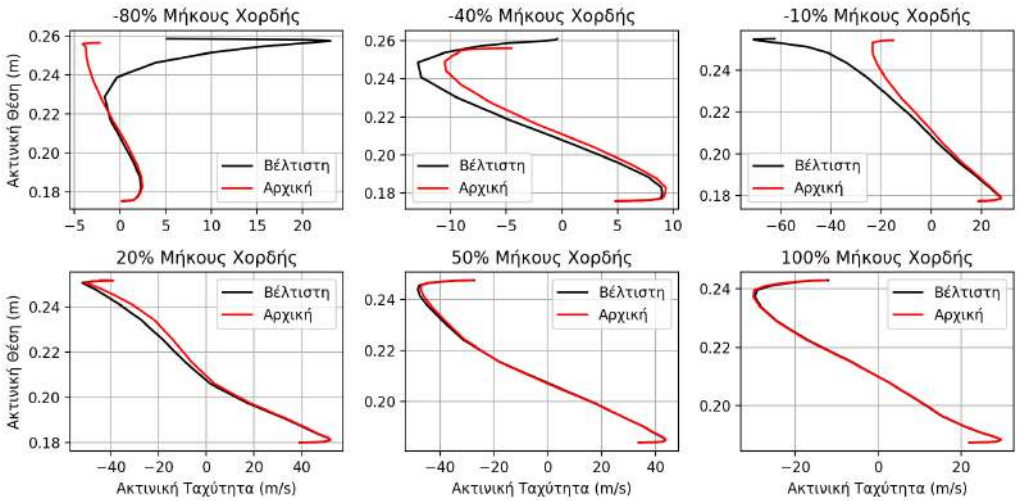

Σχήμα 13: Ακτινική κατανομή της ακτινικής ταχύτητας σε διάφορες αξονικές θέσεις της ροής.

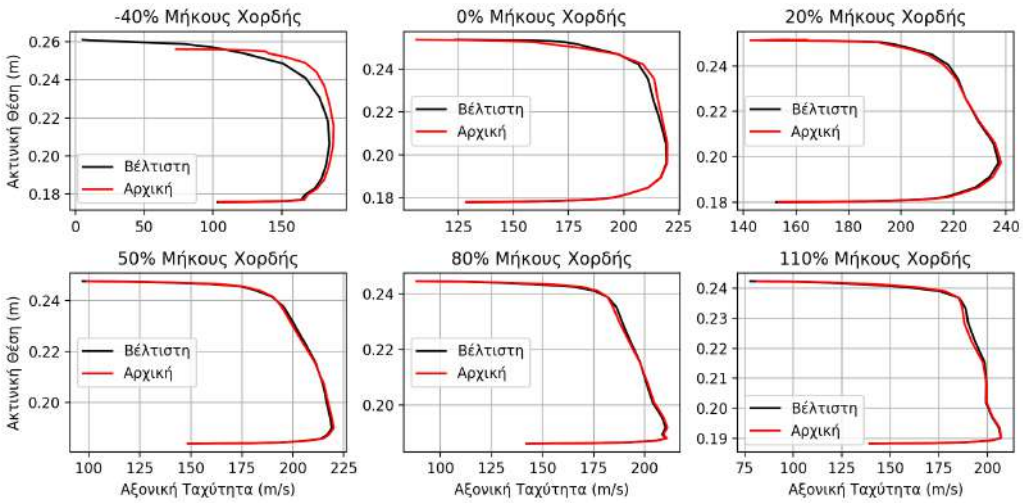

Σχήμα 14: Ακτινική κατανομή της αξονικής ταχύτητας σε διάφορες αξονικές θέσεις της ροής.

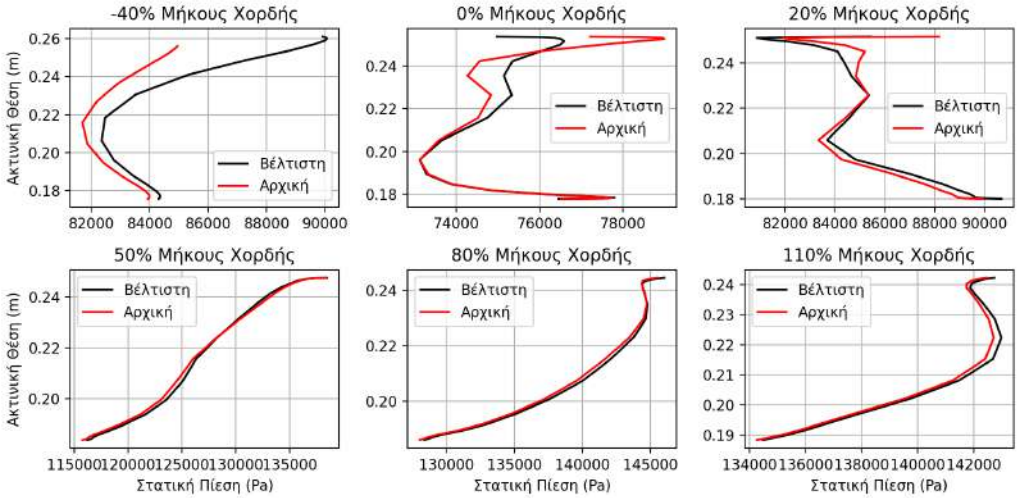

Σχήμα 15: Ακτινική κατανομή της στατικής πίεσης σε διάφορες αξονικές θέσεις της ροής.

Από το Σχήμα 15, ως αποτέλεσμα του νέου πεδίου ταχύτητας ανάντι της ροής, παρατηρούμε στην αξονική θέση, 0% επί της χορδής, να δημιουργείται μια περιοχή από 60-80% καθ΄ ύψος, με αυξημένη στατική πίεση, ενώ πάνω από αυτήν την περιοχή, παρατηρείται μειωμένη στατική πίεση σε σχέση με την αρχική γεωμετρία. Από το 0-20%, παρατηρρείται μια μεταβατική περιοχή, όπου το πεδίο της ακτινικής ταχύτητας της βέλτιστης γεωμετρίας πλησιάζει αυτό της αρχικής, παρατηρείται επίσης, ανάκτηση της αξονικής ταχύτητας στο 60-80% καθ΄ ύψος της διατομής με αντίστοιχη πτώση της στατική πίεσης, όπου πλησιάζουν αυτή της αρχικής γεωμετρίας. Στη συνέχεια, κατά την αξονική κατε-

ύθυνση, οι διαφορές μεταξύ της βέλτιστης και της αρχικής γεωμετρίας να παρουσιάζουν μια πολύ μικρή βελτίωση στην περιοχή 60-80% καθ' ύψος.

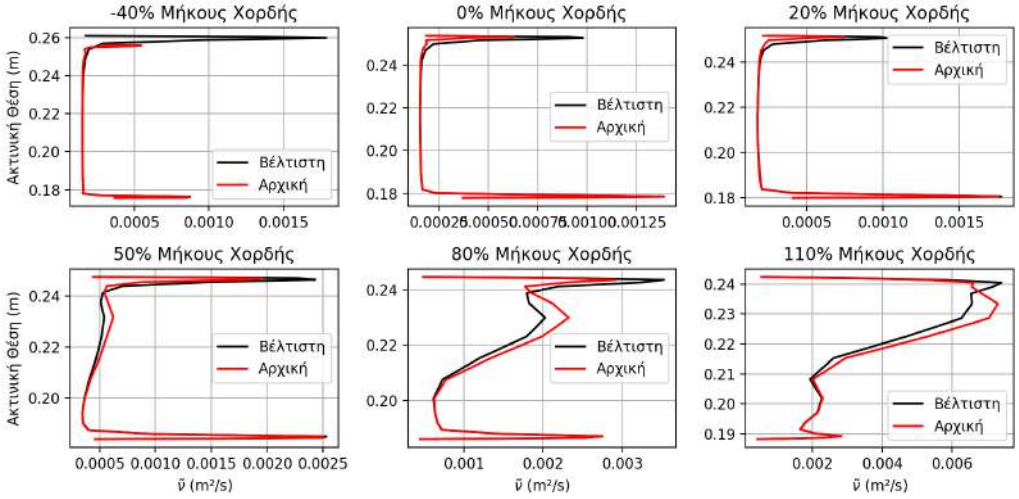

Σχήμα 16: Ακτινική κατανομή της μεταβλητής $\tilde{\nu}$ του μοντέλου Spalart-Allmaras σε διάφορες αξονικές θέσεις της ροής.

Τέλος, παρατηρώντας το πεδίο της μεταβλητής $\tilde{\nu}$ του μοντέλου τύρβης Spalart-Allmaras (Σχήμα 16), παρατηρούμε ότι από το 50% επί του μήκους χορδής και μετά, υπάρχει αισθητή μείωση αυτής, με ιδιαίτερα μειωμένα επίπεδα τύρβης πριν και μετά τη μετάβαση στο σημείο εκφυγής στην περιοχή 60-80% καθ' ύψος.

Γενικά Συμπεράσματα

Σκοπός της διπλωματικής είναι να διαμορφώσει τα κελύφη του NASA Rotor 37, προσδίδωντας τους μια αξονοσυμμετρική καμπυλότητα είτε εσωτερικά είτε εξωτερικά του πεδίου ροής.

Από την παραμετρική μελέτη γίνεται γνωστό ότι μόνο η διαμόρφωση του κέλυφους της κεφαλής ανάντι της ροής παρουσίασε θετικά αποτελέσματα, και πιο συγκεκριμένα η διαμόρφωση με κατεύθυνση προς τα εξωτερικά της ροής. Ως εκ τούτου, πραγματοποιείται βελτιστοποίηση της γεωμετρίας στην περιοχή αυτή.

Η βελτιστοποίηση πέτυχε μια αύξηση του ισεντροπικού βαθμού απόδοσης κατά 0.37% σε σχέση με την αρχική γεωμετρία, φτάνωντας το 85.7%. Επίσης, σε σχέση με τη συμμετρική καμπύλη ως μέτρο σύγκρισης, η βελτιστοποιημένη γεωμετρία παρουσιάζει μια καμπύλη με γωνία εξόδου που προωθεί το ρευστό σε όλο και περισσότερο ακτινική πορεία, ενώ ταυτόχρονα εξομαλύνει ελαφρώς το εσωτερικό της καμπύλης, "φουσκώνοντας" την.

Με τη σύγκριση των χαρακτηριστικών της αρχικής και της βέλτιστης γεωμετρίας, παρατηρείται μια μικρή βελτίωση της απόδοσης σε όλα τα σημεία λειτουργίας της κινητής πτερύγωσης, καθώς για δεδομένη στατική πίεση εξόδου, διαχειρίζεται λίγο μεγαλύτερη παροχή μάζας. Όσον αφορά το εσωτερικό πεδίο ροής της βέλτιστης γεωμετρίας, παρατηρείται περίπου στο 60-80% του καθ΄ ύψος μια μικρή αύξηση των παραμέτρων της ροής, όπως η αξονική ταχύτητα και η στατική πίεση. Επίσης, στο ίδιο τμήμα του καθ΄ ύψος, παρατηρούνται μικρότερα επίπεδα τύρβης.

Εν κατακλείδι, με τη βέλτιστη γεωμετρία παρατηρείται μια μικρή βελτίωση της ροής στο τμήμα 60-80% του καθ΄ ύψος, η οποία προέρχεται από την ανακατανομή των ταχυτήτων που προσέδωσε η νέα γεωμετρία.